CERN Linac4 - The Space Charge Challenge

Design and Commission

D I S S E R T A T I O N

zur Erlangung des akademischen Grades

doctor rerum naturalium
(Dr. rer. nat.)
im Fach Physik

eingereicht an der
Mathematisch-Naturwissenschaftlichen Fakultät I
der Humboldt-Universität zu Berlin

von
Diplom-Physiker Lutz Matthias Hein

Präsident der Humboldt-Universität zu Berlin:
Prof.Dr. Jan-Hendrik Olbertz

Dekan der Mathematisch-Naturwissenschaftlichen Fakultät I:
Prof. Stefan Hecht, Ph.D.

Gutachter/innen:

1. Prof.Dr. Eberhard Jaeschke
2. Prof.Dr. Andreas Jankowiak
3. Prof.Dr. Volker Ziemann

Tag der mündlichen Prüfung: 06.08.2013

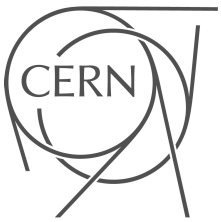

Acknowledgements

The Thesis

"CERN Linac4 - The Space Charge Challenge"

owes much to the close and fruitful collaboration with the teams of Linac4 at CERN. Supervision and guidance by the working group leader

Dr. Alessandra Lombardi

and the whole team is gratefully acknowledged.
The integration in the working group ensured a fast comprehension of the complexity of the Linac4 project and excellent support throughout the work.

The thesis work has been funded by the German doctoral student program at CERN, the "Wolfgang-Gentner-Scholarships", financed by the German Federal Ministry of Education and Research (BMBF).

Bundesministerium
für Bildung
und Forschung

Abstract

Zusammenfassung

Im Rahmen eines grossangelegten Modernisierungsprogramms des CERN Beschleunigerkomplexes zur Steigerung der Intensität der Protonenstrahlen für den "Large Hadron Collider" (LHC) wird in einer ersten Phase der Protonenbeschleuniger Linac2 durch einen H^- Ionen Beschleuniger, Linac4, mit deutlich erhöhter Teilchenenergie ersetzt. Um den Ionenstrahl an die einzelnen Beschleunigerelemente des Linac4 anzupassen sind drei Strahltransportsektionen notwendig, die aufgrund ihrer strahldynamischen Eigenschaften sensitive Stellen für ungewolltes Emittanzwachstum und Teilchenverluste sind.
Die erste Strahltransportsektion, „Low Energy Beam Transport" (LEBT), befindet sich zwischen der Teilchenquelle und dem ersten Beschleunigerelement, den Radiofrequency Quadrupole (RFQ). Mit Hilfe des LEBT wird der Strahl an den RFQ angepasst, wodurch die Teilchenverluste entlang des RFQs minimiert werden. Zwischen dem RFQ und dem Drift Tube Linac (DTL), wird die longitudinale Pulsstruktur des Teilchenstrahls an die Akzeptanz des nachfolgenden Beschleunigers mit Hilfe der zweiten Strahltransportsektion „Medium Energy Beam Transport" (MEBT) angepasst. In der ersten Phase werden die H^- Ionen in den Proton Synchroton Booster (PS-Booster) injiziert, der sich $180\,m$ entfernt von Linac4 befindet. Der Strahltransport von Linac4 zum PS-Booster stellt hohe Ansprüche an die Auslegung der Strahloptik der Transferlinie, welche die dritte Strahltransportsektion des Linac4 ist.
Die vorgelegte Dissertation behandelt die Auslegung der Strahldynamik der drei Strahltransportsektionen des Linac4. Im Rahmen der Arbeit wurde das LEBT in Betrieb genommen, dessen Strahldynamik rekonstruiert und vorbereitende Messungen für die Inbetriebnahme des RFQ durchgeführt. Die Strahldynamik der Transferlinie wurde optimiert und teilweise komplett überarbeitet. Die neue Transferlinie zeichnet sich durch eine verbesserte Emittanzerhaltung, höhere Stabilität der Strahldynamik gegenüber Aufstellungsfehlern und Feldjittern der Magnete und durch eine optimale Anpassung der Strahlparameter an die verschiedenen Injektionsschemata des PS-Boosters aus. Für die abschließenden „Start-To-End" Simulationen wurden die Strahlcharakteristiken, die bei der Inbetriebnahme des LEBTs bestimmt worden sind, als Anfangsbedingungen für die strahldynamische Simulation von Linac4 einschließlich Transferlinie genutzt. Mit Hilfe dieser „Start-To-End" Simulationen wurden kritische Positionen der Strahldynamik identifiziert, die durch Teilchenverluste oder Emittanzwachstum gekennzeichnet sind, um entsprechende Inbetriebnahmeprozeduren zu entwickeln.

Abstract

In the first phase of the upgrade program of the CERN accelerator complex the proton injector Linac2 will be replaced by a new, normal-conducting H^- ion Linac, Linac4, allowing a significant increase of the proton flux intensity along the downstream accelerator complex. In the design of Linac4 three beam transport sections are implemented to match the beam between the different accelerator elements and to model the longitudinal pulse structure. These three beam transport sections, which are the most critical locations in terms of beam quality preservation, are in the focus of this thesis.

During the work of this thesis the low energy beam transport (LEBT), which is required to match the source beam to the radiofrequency quadrupole (RFQ), has been commissioned and its beam dynamics re-constructed. The measurement campaign used to reconstruct the LEBT beam dynamics was performed with the aim to prepare the RFQ commissioning and to maximise the LEBT performance. Downstream of the Linac4 accelerator the beam is transported along a $180\,m$ long transfer line to the Proton Synchrotron Booster (PS-Booster). The transfer line optics was studied, optimised and sections were completely re-designed. The new transfer line optics is characterised by an improved preservation of the beam emittance, higher stability of the optical solution with respect to alignment errors and field jitters of the transfer line magnets and it is matched to each of the PS-Booster injection schemes.

In a concluding "Start-To-End" simulation based on the measured beam characteristics at the LEBT exit the beam dynamics of the downstream Linac, including the transfer line, was calculated. To minimise particle losses within acceptable emittance preservation the beam optics of the Medium Energy Beam Transport (MEBT) was adapted to the measured beam parameters. This "Start-To-End" simulation was performed to identify critical sections of the Linac4 beam dynamics and to adjust the commissioning strategies.

Contents

Introduction

For centuries mankind has been driven to understand the structure of nature and matter. During the 19. and 20. century science has probed subatomic scales and discovered the elements of atoms, namely electrons and the atom nucleus. As the characteristics of the atom nuclei indicate that each atom nucleus consists of even smaller elements, protons and neutrons, the theory of elementary particles was created. Over the last six decades the theoretical model of the elementary particles, the Standard Model [1], has been developed. Even today its experimental verification is still ongoing. The standard model is based on 12 leptons, 36 quarks and 12 interaction bosons. The leptons are divided into charged particles such as electrons and muons and neutral particles like electron neutrinos and muon neutrinos. Hadrons, e.g. protons and pions, are described by an ensemble of quarks. To specify their quantum chromodynamic interactions a colour charge, red, green and blue, has been introduced. In the standard model matter and anti-matter are composed of a combination of leptons, quarks and their anti-particles. The interactions, namely electrodynamic, weak and strong interactions, are described using 12 bosons. In addition to these 60 particles an additional particle, the Higgs boson [2], has been predicted needed to explain the properties of some interaction bosons.
Due to the high rest mass of several of the predicted particles high energy collider experiments are needed to verify the existence of these particles and to investigate their characteristics. Over the last decades the kinetic energy of the colliding particles has been continuously increased and most of the standard model particles were discovered.
With the mission to conduct this research the European Organisation for Nuclear Research, CERN, was founded. Since its foundation mid 1950's many of the discoveries such as the discovery of the $W^{\pm}$ bosons [3] have been accomplished at CERN. Thereby, several upgrades of the CERN accelerator complex led to a continuous increase of particle energies and performances. The latest performed upgrade was the construction of a large hadron collider [4], LHC, and the associated collider experiments, Atlas [5], CMS [6], Alice [7], LHCb [8] and Totem [9]. Due to the superconducting technology of the LHC it is possible to accelerate the colliding particles far beyond the current potential of any other accelerator.
In the scope of the LHC experiments are investigations of the symmetry breaking in the standard model, the discovery of the last missing standard model particle, Higgs boson, as well as researches beyond the standard model. Apart from the LHC experiments with extremely high particle energies further experiments with higher beam intensity requirements like CNGS [10] and ISOLDE [11] are conducted at CERN. In contrast to the LHC experiments, where the colliding particles are stored in the LHC and used for the experiments for hours, these experiments require a continuous supply of 'fresh' particles from the accelerator complex. In order to ensure the high performance of all accelerator

experiments the CERN accelerator chain is optimised for a high duty cycle. However, another important parameter in the accelerator chain is the available particle flux, which can be limited by any element in the chain and is in the focus of the near future upgrade scenarios at CERN.
The near future upgrade plans are focused in particular on the upgrade of the proton accelerator chain. Currently, the proton accelerator chain consists of Linac2, Proton Synchrotron Booster (PS-Booster), Proton Synchroton (PS), Super Proton Synchrotron (SPS) and LHC.
At the CERN accelerator complex the proton beams are generated inside a plasma source at the front end of Linac2. Directly downstream of the source exit the proton beam is focused into a radiofrequency quadrupole (RFQ), where the protons are accelerated to an energy of $750\,keV$. As a second accelerator unit of Linac2 an Alvarez structure [12], also known as Drift Tube Linac (DTL), is used to increase the kinetic energy to the Linac2 extraction energy of $50\,MeV$, which corresponds to a proton velocity of approximately 30 % of the speed of light. Due to the latest upgrade of Linac2 the proton beam current had been increased from $150\,mA$ to $180\,mA$. Using a multi-turn injection scheme bunch trains of Linac2 are accumulated into single PS-Booster buckets and bunch charges in the order of $1.3 \cdot 10^{12}$ protons are achieved. Such high bunch charge intensities are required, as each PS-Booster bunch needs to be slit into 12 to 24 bunches for an optimised filling of the LHC. The combination of high bunch charge and the low kinetic energy of the protons leads to intense space charge effects. These space charge effects are limiting the PS-Booster performance and the maximum proton flux intensity along the CERN accelerator complex. After the PS-Booster acceleration to $1.4\,GeV$ each PS-Booster bunch can be longitudinally split by means of the RF cavities. Further bunch splitting will be performed at the PS before and after the acceleration to $25\,GeV$ [13]. As mentioned these bunch splittings are required to optimise the bunch sequence in the accelerators SPS and LHC. At the SPS the protons are accelerated to a kinetic energy of $450\,GeV$.
The stage One upgrade of the CERN accelerator complex is the replacement of Linac2 with a normal conducting H^- ion Linac, named Linac4. As the performance bottleneck of the PS-Booster is caused by the space charge effects at injection energy, it is required to mitigate these effects accomplished by the increase of the PS-Booster injection energy [14]. The Linac extraction energy will be increased from $50\,MeV$(Linac2) to $160\,MeV$(Linac4). Further improvements of the PS-Booster injection are expected by the charge-exchange H^- ion injection [15] as well as by the optimisation of the longitudinal pulse structure using a special chopper section [14]. With this accelerator upgrade the potential of raising the proton flux intensity by a factor of 1.7 is envisaged, at which a LHC bunch population of $1.7 \cdot 10^{11}$ protons becomes feasible. With this proton flux intensity the LHC nominal Luminosity[1] of $1.0 \cdot 10^{34}\,cm^{-2}\,s^{-1}$ can be increased to LHC ultimate Luminosity of $2.3 \cdot 10^{34}\,cm^{-2}\,s^{-1}$.

[1]The cross section of an interaction, which is defined by nature, is linked to the detected number of events in the detector by the Luminosity. A high Luminosity is in particular required, if rare interactions are in the focus of the experiments.

For a maximised performance of Linac4 three beam transport sections are required. A Low Energy Beam Transport (LEBT) is needed to match the source beam into the RFQ. Downstream of the RFQ a Medium Energy Beam Transport (MEBT) will be used to manipulate the longitudinal beam pulse structure to minimise the radioactive load of the PS-Booster. In order to transport the beam from the accelerator structure of Linac4 to the PS-Booster a High Energy Beam Transport (HEBT), so called transfer line, is required.
In the scope of this thesis are the optimisation and commissioning of these three beam transport sections. This includes the commissioning of the LEBT, the tuning of the MEBT as well as the layout and beam dynamics optimisation of the transfer line from Linac4 to the PS-Booster. As the beam dynamics of Linac4 and of the PS-Booster are strongly influenced by space charge effects, the impact of space charge effects on beam dynamics is summarised in chapter 1. The commissioning of the low-energy front-end of Linac4, i.e. H^- ion source and LEBT, has been performed in the framework of this thesis. The results of the Test Stand commissioning and the re-constructed beam optics are reported in chapter 2. In chapter 3 the optimisation of the transfer line beam dynamics in terms of beam quality preservation is discussed.
At the Test Stand commissioning a first characterisation of the beam is completed. Based on these measured beam characteristics the further downstream sections of Linac4 from the exit of the LEBT to the PS-Booster injection point is simulated. The aim of this updated 'Start-to-End' simulation is the investigation of the performance of the Linac4 accelerator elements and of the transfer line optics. A summary of the 'Start-to-End' simulation results is presented in the final chapter.

Linac4 Project - Overview

The Large Hadron Collider, LHC, is the latest major upgrade of the CERN accelerator complex, Fig. 0.1.

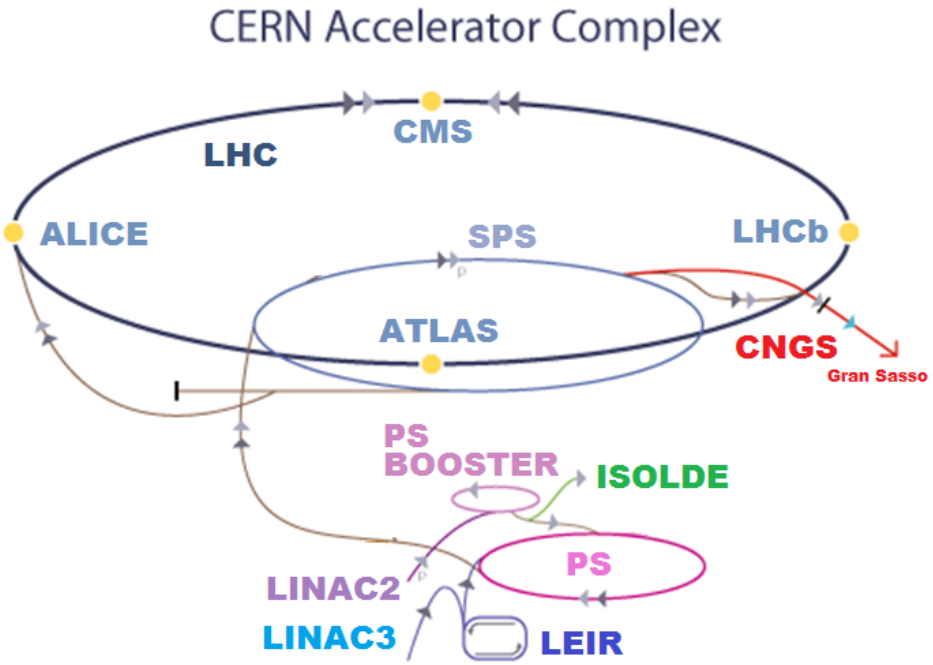

Figure 0.1: CERN Accelerator Complex
This figure shows the current CERN accelerator complex consisting of Linac2, Linac3, Low Energy Ion Ring (LEIR), PS-Booster, PS, SPS and LHC.

The LHC is used to accelerate protons to kinetic energies up to $7\,TeV$ allowing scientists to explore new regions of physics. Its performance in terms of luminosity is restricted by the upstream accelerator chain, Fig. 0.2.

Figure 0.2: Proton Accelerator Chain
The proton bunches are generated at Linac2 and accelerated to a kinetic energy of $50\,MeV$. *At the PS-Booster the proton beams are accelerated to* $1.4\,GeV$. *In further accelerator steps the proton energy is increased to* $25\,GeV$ *(PS) and* $450\,GeV$ *(SPS). In the final accelerator, LHC, the kinetic energy of the protons can be increased up to* $7\,TeV$.

The CERN accelerator chain for proton beams consists of Linac2, Proton Syn-

chrotron Booster (PS-Booster), Proton Synchrotron (PS), Super Proton Synchrotron (SPS) and Large Hadron Collider (LHC). In this accelerator chain the proton flux intensity is limited by the PS-Booster performance.
The present PS-Booster injection energy is $50\,MeV$. Hence, the proton velocity amounts to approximately 30 % of the speed of light. Along the accelerator chain the PS-Booster bunches are longitudinally split to produce 12 to 24 LHC bunches from each PS-Booster bunch. Therefore, high numbers of particles, in the order of $1.4 \cdot 10^{12}$ protons, are accumulated in each PS-Booster bunch. This leads to intense space charge effects, which limit the PS-Booster performance. In order to suppress these space charge effects it is necessary to increase the PS-Booster injection energy.
In the Linac4 project the existing proton Linac, Linac2, will be replaced by a new normal-conducting hydrogen-ion (H^- ion) Linac, Linac4, whose extraction energy is $160\,MeV$, Fig. 0.3.

Figure 0.3: New Proton Accelerator Chain with Linac4
In the new accelerator chain Linac2 is replaced with Linac4. At Linac4 H^- ion bunches are generated and accelerated to a kinetic energy of $160\,MeV$. The H^- ions are "stripped" to protons at the PS-Booster charge-exchange injection.

Due to the higher particle energy the space charge effects will be sufficiently suppressed to achieve a doubling of the proton flux intensity along the accelerator chain.
The main component of the Linac4 project is the new H^- ion Linac, Linac4. This Linac consists of a H^- ion source, Low Energy Beam Transport (LEBT), Radiofrequency Quadrupole (RFQ), Medium Energy Beam Transport (MEBT), Drift Tube Linac (DTL), Cell-Coupled Drift Tube Linac (CCDTL) and Pi-Mode-Structure (PiMS), Fig. 0.4.

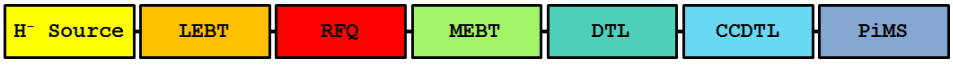

Figure 0.4: Sequence of the Linac4 Components

The H^- ion source is based on the design of the DESY (Hamburg) H^- ion source [14]. In order to enhance the H^- ion current the design extraction voltage has been increased from $35\,kV$ (DESY) to $45\,kV$ (CERN).
Between source exit and the entrance of the first accelerator element, RFQ, a LEBT is needed to match the beam to the RFQ requirements. Moreover, the LEBT will be equipped with diagnostics devices to control the beam quality and to supervise the performance of the source. Due to the high intensity of the source beam a special RFQ design was chosen to reduce the impact of the

intensive space charge effects. At the RFQ output energy of $3\,MeV$ it is foreseen to optimise the bunch train structure to minimise the radioactive load of the PS-Booster elements caused by particle losses at the PS-Booster injection. For the multi-turn PS-Booster injection sequences of 133 bunches in a period of 352 bunches have to be dumped. Therefore, the MEBT is equipped with a special chopper section. By using two pairs of specially designed plates a transverse deflection will be applied on selected bunch train segments. Due to the amplification of the generated beam offset by means of a quadrupole the bunch train section will be directed into a MEBT beam dump.
In addition to the chopper section the MEBT is equipped with two families of four quadrupoles to match the beam from the RFQ into the chopper section and to match the beam from the chopper section to the Drift Tube Linac (DTL). In Fig. 0.5 a schematic of the MEBT components is presented and a picture of the assembled MEBT is shown in Fig. 0.6.

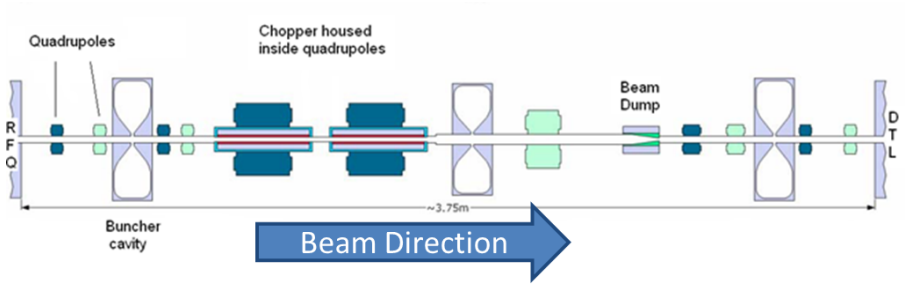

Figure 0.5: Schematic of the MEBT Section
In this scheme the components of the MEBT are shown. Downstream the RFQ four quadrupoles are foreseen to match the beam to the chopper section. This chopper section consists of two special quadrupoles equipped with 'chopper' plates, a third quadrupole and a beam dump. The chopper plates are used to deflect sequences of the bunch train. This deflection will be amplified by the third quadrupole. The resulting offset will be sufficient to stop the selected bunch sequences in the MEBT beam dump. Downstream the MEBT beam dump four quadrupoles will be used to match the beam to the DTL. In order to maintain a short bunch length three cavity cells are installed along the MEBT.

The DTL will be used to accelerate the beam from $3\,MeV$ to $50\,MeV$. In order to enhance the efficiency of the RF-power a transverse focusing structure based on permanent magnet quadrupoles is foreseen. However, this structure does not allow an adjustment of the field gradients to varying beam parameters. Therefore, the DTL focusing structure has been optimised to transmit H^- ion beams with peak beam currents in the range from $20\,mA$ to $70\,mA$.
Downstream of the DTL the H^- ions will be further accelerated to $100\,MeV$ using the Cell-Coupled Drift Tube Linac (CCDTL). The major difference between DTL and CCDTL structure is the configuration of the cavities. The design of the CCDTL cavities permits the use electromagnetic quadrupoles, which allows the adaption of the CCDTL optics to varying beam parameters. The final

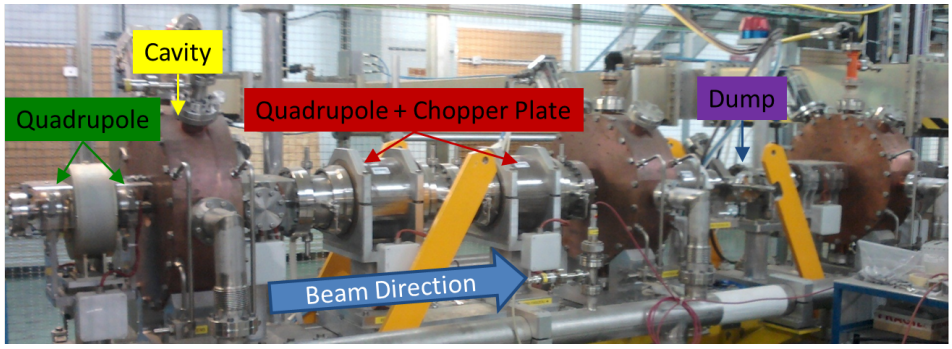

Figure 0.6: Picture of the MEBT Section
In this figure the assembled MEBT is shown. The characteristic features of the MEBT such as the three cavity cells and the two special quadrupoles are shown.

acceleration from $100\,MeV$ to $160\,MeV$ will be accomplished by means of 12 modules of Pi-Mode-Structure cavities (PiMS). Thereby, the last two modules will be used to modulate the average bunch energy by $\Delta E = 1.2\,MeV$ along the bunch train. This energy modulation is required to optimise the phase space painting at the PS-Booster injection.
The length of the accelerator structure of Linac4 amounts to $80\,m$, which is significantly longer than the length of Linac2. With respect to further upgrade scenarios Linac4 will be placed in a newly constructed building near the existing accelerator complex, Fig. 0.7 and Fig. 0.8.

Parts of the existing transfer line between Linac2 and PS-Booster will be further used for the beam transfer from Linac4 to the PS-Booster. However, the construction of a $70\,m$ long transfer line between the exit of Linac4 and the Linac2-PS-Booster transfer line is needed, Fig. 0.8.
Along the Linac the dimensions of the bunches are maintained compact to maximise the RF-power use. But these bunch dimensions lead to a high charge density causing intense space charge effects. Due to the absence of longitudinal focusing along the transfer line an increase of the bunch length is expected. This leads to a reduction of the charge density and so to a reduction of the intensity of the space charge effects. As a consequence the layout and the beam optics of the first transfer line part are in particular crucial in terms of preservation of the transverse emittance.
Moreover, it is expected that the bunch energy spread will be significantly increased by the space charge effects. In order to ensure a minimum energy spread at the PS-Booster injection the use of a debuncher cavity is required. The cavity position in the new transfer line part will be determined according to its beam dynamics efficiency and the estimated RF-power consumption.
The new transfer line part joins the exiting accelerator complex at the bending magnet BHZ20. Downstream of this bending magnet the existing transfer line from Linac2 to PS-Booster will be used to inject the Linac4 beam into the PS-Booster. Due to the higher particle energy several beam optics elements such

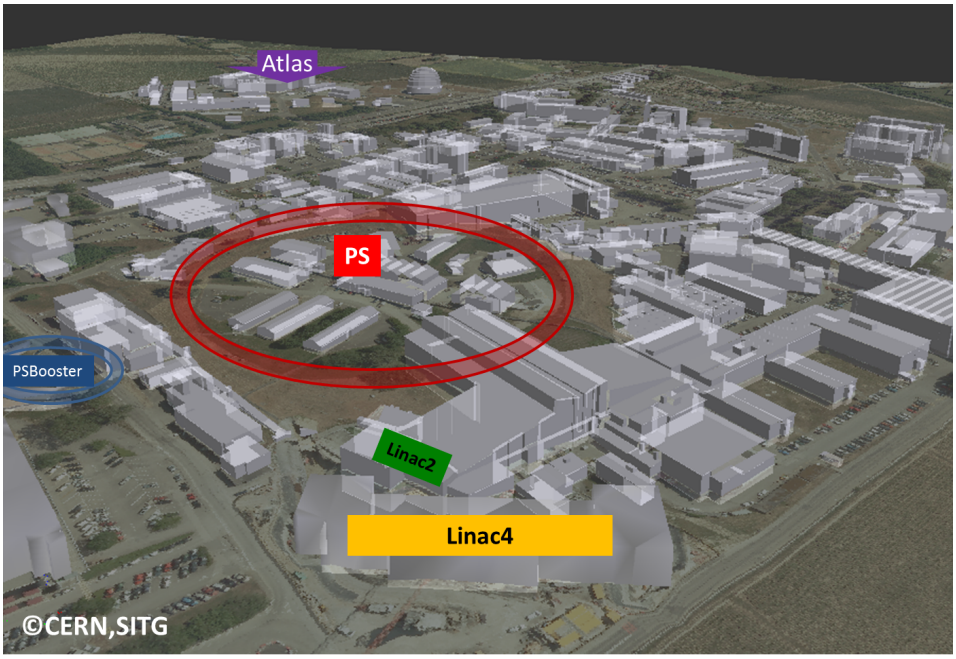

Figure 0.7: Accelerator Complex
In this scheme the locations of the first accelerators of the CERN accelerator chain are shown. The location of the 30 *m long Linac2 is indicated by the green-marked label. For the* 80 *m long Linac4 a new building has been constructed close to the Linac2 location. Also shown in this scheme are the locations of the* 628 *m long PS (red) and of the* 157 *m long PS-Booster (blue).*

as the distributor kicker magnets need to be upgraded. Moreover, the injection section of the PS-Booster will be re-constructed for the intended H^- ion charge exchange injection [15].

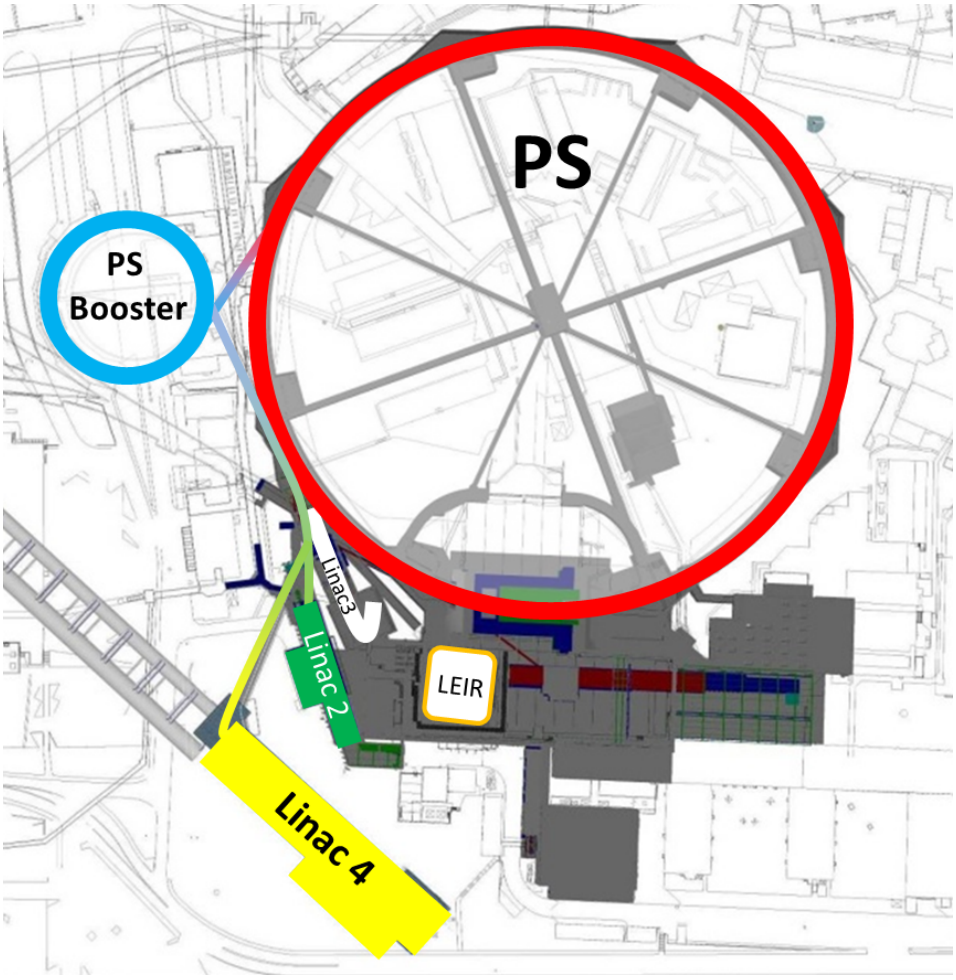

Figure 0.8: Accelerator Complex II

In this schematic overview the locations of Linac2, Linac3, Linac4, LEIR, PS-Booster and PS are shown. The construction of a 70 m long transfer line from the exit of Linac4 to the Linac2-PS-Booster transfer line is required. Parts of the existing transfer line from Linac2 to the PS-Booster will be re-used for the beam transport from Linac4 to the PS-Booster.

1
Space Charge Effects

The major limitation towards higher proton flux intensity in the CERN accelerator chain is the PS-Booster performance, which is limited by intense space charge effects. As the space charge effects are defined by the particle distribution, a short introduction of linear beam dynamics and a description of the beam dynamics of particle ensembles are presented in the first section. In order to quantify the impact of space charge effects on the development of particle ensembles a linear space charge model is introduced. Based on this model the impact of space charge effects on optimised lattices is illustrated. In the case of circular accelerators such as the PS-Booster particle ensembles are passing through a constant sequence of electromagnetic fields. In this configuration constructive interferences of beam dynamic disturbances can be generated leading to particle losses. These resonances, so called tune resonances, are defined by the single particle motion. The particles are not propagating exactly on the design path, but they oscillate transversely around it. The tune specifies the number of these transverse oscillations per turn inside the circular accelerator. As the direct space charge effects are inducing disturbances of the beam dynamics, an impact on the tune is observed. A quantitative description of the tune change induced by space charge effects is presented in the final section of this chapter.

1.1 Linear Beam Dynamics

1.1.1 Coordinate System

In general the magnetic structure of an accelerator defines a design path on which the nominal or reference particle will propagate. This particle is characterised by the reference parameters such as rest mass, charge and kinetic energy. In order to describe and calculate the dynamics of particle ensembles a special coordinate system is commonly used. Basic element of this coordinate system is a 'moving trihedral', which is propagating along the design path of the accelerator. Its motion can be identified with the motion of the reference particle. The coordinates of the particles are specified with respect to the position of the reference particle by:

$$\begin{pmatrix} x \\ x' \\ y \\ y' \\ \delta l \\ \frac{\Delta p}{p} \end{pmatrix} = \begin{pmatrix} \text{horizontal offset} \\ \text{horizontal slope} \\ \text{vertical offset} \\ \text{vertical slope} \\ \text{longitudinal offset} \\ \text{momentum deviation} \end{pmatrix}. \tag{1.1}$$

In Fig. 1.1 an illustration of the co-moving coordinate system is presented.

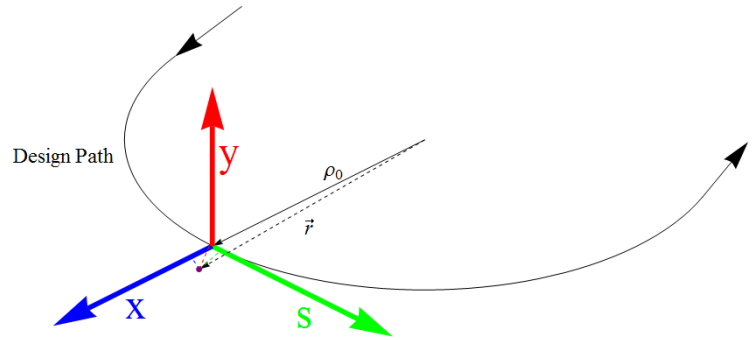

Figure 1.1: Coordinate System
In this figure the co-moving coordinate system, which is commonly used in accelerator physics, is illustrated. The motion of the origin of this coordinate system can be identified with the movement of a reference particle, which is characterised by the design momentum and whose motion is restricted to the design path. The transverse coordinates of the particles are defined by their transverse offset from the design path. Longitudinal coordinates are defined as the momentum deviation from the design momentum and the longitudinal distance from the origin of the coordinate system.

1.1.2 Equation of Motion

Usually electromagnetic fields are used to guide, focus and accelerate the particles along a particle accelerator. Therefore, the beam dynamics of the charged particles are determined by the Lorentz-force [16],

$$\vec{F} \quad = \quad q \cdot \left(\vec{E} + \vec{v} \times \vec{B} \right). \tag{1.2}$$

As an example a magnetic structure has been assumed, which consists of an overlap of a constant vertical dipole field B_0 with a transverse field gradient g. The field distribution is defined as:

$$B_x \quad = \quad -gy \ , \ B_y = B_0 - gx \ , \ B_s = 0. \tag{1.3}$$

It is convenient to scale the field strength with the charge and the momentum of the reference particle, $\frac{q}{p_0}$. Hence, the constant vertical magnetic field B_0 is converted into a curvature radius $\varrho[m]$,

$$\varrho \quad = \quad \frac{p_0}{q} \cdot \frac{1}{B_0}. \tag{1.4}$$

Furthermore, the transverse field gradient g causing a focusing impact can be described as a focusing strength $k[m^{-2}]$,

$$k \quad = \quad g \cdot \frac{q}{p_0}. \tag{1.5}$$

These transformations lead to a compact expression of the equations of motion:

$$x'' + \left(\frac{1}{\varrho^2} - k\right) x = \frac{1}{\varrho}\frac{\Delta p}{p_0}\,, \tag{1.6}$$

$$y'' + k\,y = 0. \tag{1.7}$$

Here the single particle motion in horizontal and vertical phase space are decoupled. The vertical particle motion is characterised by the focusing impact of the field gradient g. Eq. 1.6 shows that the horizontal particle motion is coupled with the longitudinal particle motion. This coupling is called dispersion.

1.1.3 Dispersion

Dispersion D specifies the impact of the particle energy on its transverse dynamics. Due to a difference in the particle momentum or the average momentum of a particle ensemble from the design momentum a different propagation path will be defined leading to a transverse displacement Δx, Fig. 1.2.

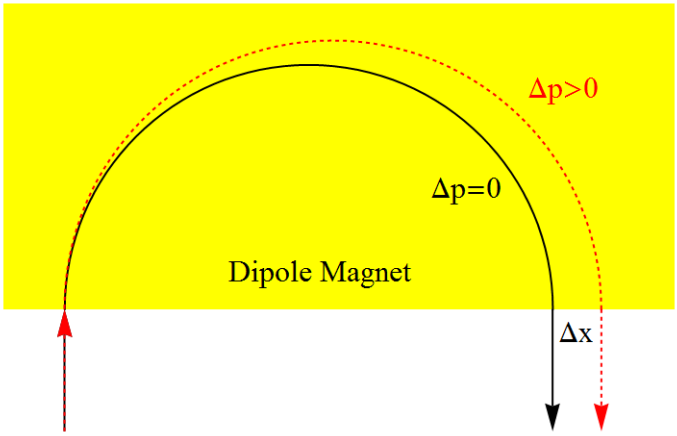

Figure 1.2: Dispersion along a Bending Magnet
The different momentum of the two particles leads to different curvature radii causing a transverse spatial separation Δx of the particles.

Dispersion is characterised by this transverse displacement Δx, which is mathematically defined as [17]:

$$\Delta x = D_x \frac{\Delta p}{p}\,, \tag{1.8}$$

$$\Delta x' = D'_x \frac{\Delta p}{p}\,. \tag{1.9}$$

The dispersion D describes the variation of the transverse position caused by a momentum deviation, whereas the angular dispersion D' characterises the variation of the slope x' or y' in dependence of a momentum deviation. Using this

definition the calculation of path changes due to energy variations is possible. As particle ensembles are characterised by non-monochromatic energy distributions, the transverse distribution of particle ensembles is influenced by their energy distributions at dispersive sections. This topic is discussed in the following section.

1.1.4 Transfer Matrix Formalism

In order to calculate the particle motion it is convenient to use the transfer matrix formalism. In this formalism the impact of an accelerator element such as a dipole magnet on the particle coordinates is expressed by a matrix. By using this matrix the initial particle coordinates of a particle are converted into the final particle coordinates.

$$\vec{x_i} \rightarrow \vec{x_f} \quad = \quad R_{i \rightarrow f} \cdot \vec{x_i} \tag{1.10}$$

For the solution of the equations of motion of Eq. 1.7 the ansatz consists of the linear combination of two linearly independent solutions:

$$y(s) \quad = \quad A\, c_y(s) + B\, s_y(s). \tag{1.11}$$

For a positive coefficient k, $k > 0$, the functions $c_y(s)$ and $s_y(s)$ are identified with the sine and cosine functions, whereas for a negative coefficient k, $k < 0$, these functions are specified as the hyperbolic functions hyperbolic sine and hyperbolic cosine. In the case of a positive coefficient k the ansatz is:

$$y(s) \quad = \quad A\, cos(\sqrt{k}s) + B\, sin(\sqrt{k}s) \tag{1.12}$$
$$y'(s) \quad = \quad -\sqrt{k}A\, sin(\sqrt{k}s) + \sqrt{k}B\, cos(\sqrt{k}s). \tag{1.13}$$

The coefficients A and B are determined by the initial particle coordinates (y_0, y'_0):

$$y(0) \quad = \quad y_0 = A\, cos(\sqrt{k}0) + B\, sin(\sqrt{k}0) \tag{1.14}$$
$$y'(0) \quad = \quad y'_0 = -\sqrt{k}A\, sin(\sqrt{k}0) + \sqrt{k}B\, cos(\sqrt{k}0). \tag{1.15}$$

Hence, the equation of motion is given by:

$$y(s) \quad = \quad y_0\, cos(\sqrt{k}s) + \frac{y'_0}{\sqrt{k}}\, sin(\sqrt{k}s) \tag{1.16}$$
$$y'(s) \quad = \quad y_0\, (-\sqrt{k}\, sin(\sqrt{k}s)) + y'_0 cos(\sqrt{k}s). \tag{1.17}$$

This solution can be expressed by a transfer matrix:

$$\begin{pmatrix} y(s) \\ y'(s) \end{pmatrix} \quad = \quad \begin{pmatrix} cos(\sqrt{k}s) & \frac{1}{\sqrt{k}}\, sin(\sqrt{k}s) \\ -\sqrt{k}\, sin(\sqrt{k}s) & cos(\sqrt{k}s) \end{pmatrix} \cdot \begin{pmatrix} y_0 \\ y'_0 \end{pmatrix}. \tag{1.18}$$

In the case of a dipole magnet without a transverse field gradient Eq. 1.6 sim-

plifies to:

$$x'' + \frac{1}{\varrho^2}\, x \;=\; \frac{1}{\varrho}\,\frac{\Delta p}{p}. \tag{1.19}$$

The transformation of the particle coordinates is described by:

$$\begin{pmatrix} x(s) \\ x'(s) \\ \frac{\Delta p}{p}\,(s) \end{pmatrix} = \begin{pmatrix} cos(\frac{s}{\varrho}) & \varrho\, sin(\frac{s}{\varrho}) & \varrho\,\left(1 - cos(\frac{s}{\varrho})\right) \\ -\frac{1}{\varrho}\, sin(\frac{s}{\varrho}) & cos(\frac{s}{\varrho}) & sin(\frac{s}{\varrho}) \\ 0 & 0 & 1 \end{pmatrix} \begin{pmatrix} x(0) \\ x'(0) \\ \frac{\Delta p}{p}\,(0) \end{pmatrix}. \tag{1.20}$$

In this 3×3 transfer matrix the correlations between the horizontal coordinates x and x' and the longitudinal coordinate $\frac{\Delta p}{p}$ are expressed by the matrix elements R_{13}, Dispersion D_x, and R_{23}, angular Dispersion D'_x. The transfer matrix formalism can be extended to 6 dimensions by using 6×6 transfer matrices, which allows the calculation of the particle motion in the 6 dimensional phase space [18].

1.1.5 Periodical Structures and Stability Criterion

In periodical structures such as circular accelerators, where the particles have to perform numerous turns, certain conditions for the focusing structures are mandatory to ensure a stable beam transport. As already discussed the transformation of the particle coordinates can be described by transfer matrices. In case of a periodical structure with N periods the transformation of the particle coordinates can be expressed as:

$$\vec{x}_f \;=\; R_{i\to f} \cdot \vec{x}_i = (R_L)^N \cdot \vec{x}_i, \tag{1.21}$$

where the transformation matrix R_L represents the coordinate transformation for one period. In the so called Twiss matrix presentation [17] R_L is given by:

$$R_L \;=\; cos(\mu) \begin{pmatrix} 1 & 0 \\ 0 & 1 \end{pmatrix} + sin(\mu) \begin{pmatrix} \alpha & \beta \\ -\gamma & -\alpha \end{pmatrix} \quad \text{with} \tag{1.22}$$

$$cos(\mu) \;=\; \frac{1}{2}\, trace(R) \quad \text{and} \tag{1.23}$$

$$\beta \;=\; \frac{R_{12}}{sin(\mu)}; \quad \alpha = \frac{R_{11} - R_{22}}{2\, sin(\mu)}; \quad \gamma = -\frac{R_{21}}{sin(\mu)} \tag{1.24}$$

The coordinate transformation for N periods is given by:

$$(R_L)^N \;=\; cos(N\,\mu) \begin{pmatrix} 1 & 0 \\ 0 & 1 \end{pmatrix} + sin(N\,\mu) \begin{pmatrix} \alpha & \beta \\ -\gamma & -\alpha \end{pmatrix}. \tag{1.25}$$

In order to ensure a stable beam transfer the variable μ must be real to avoid an exponential growth of particle offsets. Hence, a stability criterion is,

$$|trace(R)| \;<\; 2. \tag{1.26}$$

Single Particle Motion

In case of negligible coupling the motion of single particles along a periodical structure is defined by the Hills equation [18][17],

$$y'' + k(s)\, y \;=\; 0. \tag{1.27}$$

Based on the Floquet theorem two linearly independent solutions exist. They are expressed as a product of a periodical function $A_r(s)$ and an exponential function:

$$y_r(s) \;=\; A_r(s) \cdot e^{\pm i \frac{s}{L}} \quad \text{with} \tag{1.28}$$

$$A_r(s+L) \;=\; A_r(s) \quad , \; \text{r} = 1{,}2. \tag{1.29}$$

The linear combination of both solutions defines the most general solution of the Hills equation. For the particle motion the development of its position is expressed as:

$$y(s) \;=\; a\sqrt{\beta(s)} \cdot cos(\psi(s) + \psi_0). \tag{1.30}$$

The argument $\psi(s)$, so called phase advance, is defined as:

$$\psi(s) \;=\; \int_0^s \frac{\mathrm{d}\tilde{s}}{\beta(\tilde{s})} \;. \tag{1.31}$$

As mentioned the particles are not moving exactly on the design orbit of the accelerator, but the particles are performing oscillations around it, so called betatron oscillations. In case of a circular accelerator the numbers of betatron oscillations per turn is defined as tune Q, Fig. 1.3,

$$Q \;=\; \frac{1}{2\pi} \oint \frac{\mathrm{d}s}{\beta(s)}. \tag{1.32}$$

The development of the function $\beta(s)$ is determined by the magnetic structure [17]. In addition to the β function the functions $\alpha(s)$ and $\gamma(s)$ can be introduced,

$$\alpha \;=\; -\frac{1}{2}\,\beta' \quad , \tag{1.33}$$

$$\gamma \;=\; \frac{1+\alpha^2}{\beta}. \tag{1.34}$$

These parameters $\beta(s)$, $\alpha(s)$ and $\gamma(s)$ are identified with the Twiss parameters presented in Eq. 1.24. In a linear approximation at each position of the focusing structure the phase space movement of a particle is restricted to an ellipse, whose shape and orientation can be described by the Twiss parameters.
By means of the Courant-Snyder-Invariant a correlation between Twiss parameters and properties of the phase space distribution of particle ensembles is possible [17]. As a consequence the development of the β function can be used

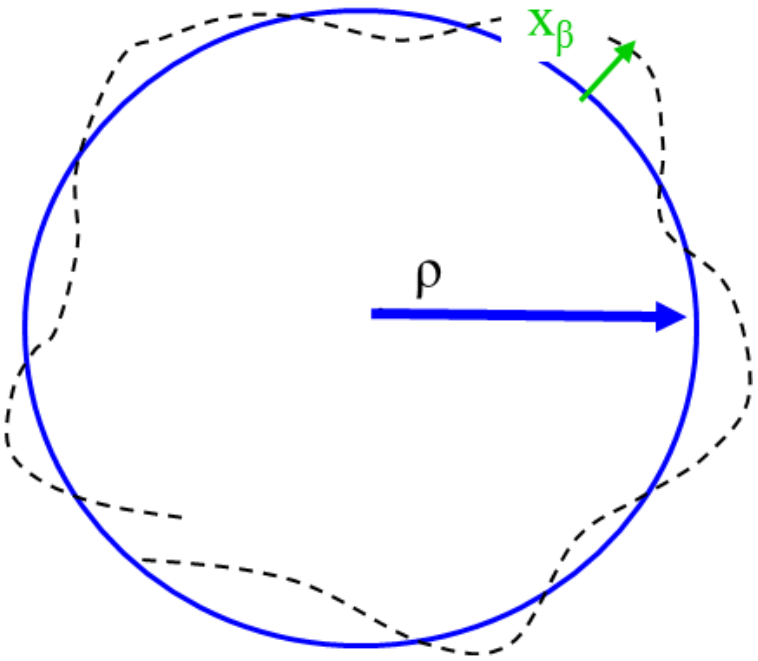

Figure 1.3: Tune

In this figure [19] an illustration of the tune is presented. The particles are not moving exactly on the design orbit (blue), but due to the focusing structure an oscillation of the particles around the design orbit can be accomplished, called betatron oscillation. The number of oscillations per turn defines the tune. In the example a tune of approximately 5.2 is plotted.

to determine the development of the beam size $\sigma(s)$ or beam envelope,

$$\sigma(s) \quad = \quad \sqrt{\varepsilon\,\beta(s)}. \tag{1.35}$$

In order to illustrate the dependency between single particle motion, phase advance and beam envelope a simple focusing structure consisting of an alternating sequence of focusing and defocusing quadrupole, FODO lattice, has been simulated. In Fig. 1.4(1) the development of the beam envelope along the structure and the motion of a single particle are plotted. In order to demonstrate the physical meaning of the phase advance the particle position in the transverse phase space [in arbitrary units] at the centre of each horizontally focusing quadrupole is shown in Fig. 1.4(2).

Tune and Tune Resonances

In an accelerator facility the particle motion in the machine is usually disturbed by field errors. Due to manufactory reasons the field distributions of each magnets contains higher order magnetic multipole components. Also due to field jitters and alignment errors disturbances of the beam transport are unavoid-

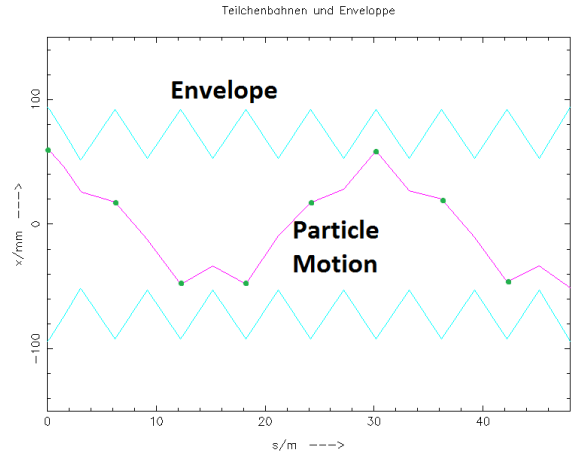

(1) Envelope and Particle Motion along the FODO Lattice

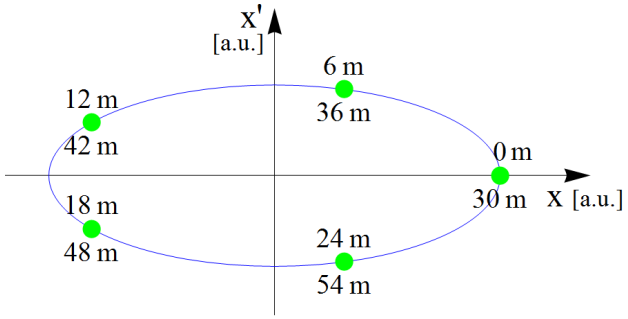

(2) Phase Space Motion of the Particle

Figure 1.4: Beam Envelope, Single Particle Motion and Phase Advance
In Fig. (1) [19] the development of the beam envelope and a single particle motion are plotted. The beam envelope is defined by the β-function and shows the periodicity of the FODO lattice. In Fig. (2) the phase space coordinates of the particle at the focusing quadrupole magnets of the FODO lattice are illustrated. In contrast to the development of the beam envelope the single particle motion is characterised by a significant higher period length of 5 FODO cells determining a phase advance of $\psi(FODO) = 72\,deg$ per FODO cell. The neighbouring particle coordinates on the plotted ellipse in Fig. (2) are separated by a phase advance of $72\,deg$.

able. In the case of circular accelerators the particle ensembles will have to pass through a defined sequence of field errors several times. In order to avoid a constructive interference of the disturbances, so called tune resonances, additional constraints for a stable beam transport are required.
In order to introduce these constraints the impact of two field disturbances on the particle motion and on the development of the particle ensemble is summarised. A detailed description is presented in [17].
A dipole field error, which can be generated by a misaligned quadrupole, causes

a deflection of the particles. In the concept of the phase space presentation this deflection leads to a shift of the particle ensemble along the ordinate (x' or y'). This shift is constant with each loop. In the case of an integer tune the beam deflections of each turn are superposing, which leads to the loss of the particles. The change of a quadrupole field ΔK affects the development of the β-function leading to a variation of the tune,

$$\Delta Q = \frac{1}{4\,\pi} \oint \beta(s) \cdot \Delta K(s)\,\mathrm{d}s. \tag{1.36}$$

The change of the β function at position s of the accelerator is given by:

$$\Delta\beta(s) = \frac{\beta(s)}{2\,sin(2\pi Q)} \oint \beta(t) \cdot \Delta K(t)\,cos(2\,|\Phi(t) - \Phi(s)| - 2\pi Q)\,\mathrm{d}t. \tag{1.37}$$

The impact of the field error on the β function depends on the phase advance difference between measurement point and position of the field error, $|\Phi(t) - \Phi(s)|$. It depends linearly on the product of the field disturbance and the β function at its position. Most important, the change of the β function is inversely proportional to the sine of the tune, $\Delta\beta(s) \sim \frac{1}{sin(2\pi Q)}$. Therefore, the operation at half integer tune values has to be avoided.
For higher order field components further constraints exist. These constraints can be summarised in a diagram, so called tune resonance diagram, Fig. 1.5.
In this diagram the horizontal (Q_x) and the vertical tune (Q_y) are plotted. Each of the lines in this plot is representing a resonance. For the calculation of the resonances the following formulas are used,

$$m\,Q_x + n\,Q_y = l, \tag{1.38}$$

$$|m| + |n| = \mathcal{O} \quad with \;\; m,\, n,\, l\,\epsilon\,\mathbb{Z}\;\; . \tag{1.39}$$

The resonances are defined by Eq. 1.38 and their orders $\mathcal{O}$ are determined by the integer coefficients m and n with Eq. 1.39.

1.1.6 Characterisation of Particle Ensembles

In addition to the description of the motion of single particles it is possible to use the transfer matrix formalism to determine the development of particle ensembles.
Particle ensembles can be described by their phase space distributions
$\varrho = \varrho(x, x', y, y', \delta l, \frac{\Delta p}{p})$. In a linear approximation a particle distribution can be characterised by its first and second order moments. These moments are used to define the position, dimensions and orientation of a six dimensional ellipsoid. The dimensions and orientation of this ellipsoid are represented using the Σ matrix. Its diagonal elements represent the square of beam size in the six

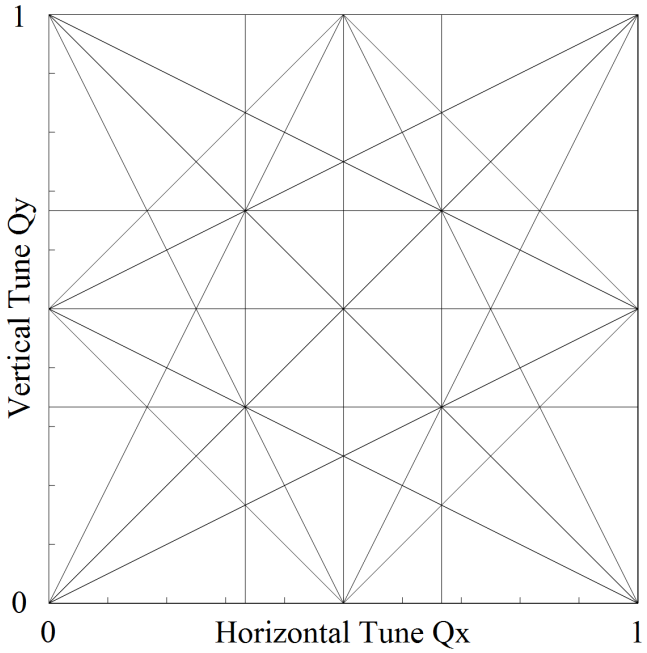

Figure 1.5: Tune Resonance Diagram
In this diagram the tune resonances to the third order have been plotted. As the resonances are defined by the non-integer fraction of the tune, the plot range has been restricted from 0 *to* 1 *for horizontal and vertical tune.*

dimensions, e.g. $\sigma_{11} = \sigma_x^2$.

$$\begin{pmatrix} \sigma_{11} & \cdots & \sigma_{16} \\ \vdots & \ddots & \vdots \\ \sigma_{61} & \cdots & \sigma_{66} \end{pmatrix} = \begin{pmatrix} \sigma_x^2 & \sigma_{xx'} & \sigma_{xy} & \sigma_{xy'} & \sigma_{x\Delta l} & \sigma_{x\frac{\Delta p}{p}} \\ \sigma_{xx'} & \sigma_{x'}^2 & \sigma_{x'y} & \sigma_{x'y'} & \sigma_{x'\Delta l} & \sigma_{x'\frac{\Delta p}{p}} \\ \sigma_{xy} & \sigma_{x'y} & \sigma_y^2 & \sigma_{yy'} & \sigma_{y\Delta l} & \sigma_{y\frac{\Delta p}{p}} \\ \sigma_{xy'} & \sigma_{x'y'} & \sigma_{yy'} & \sigma_{y'}^2 & \sigma_{y'\Delta l} & \sigma_{y'\frac{\Delta p}{p}} \\ \sigma_{x\Delta l} & \sigma_{x'\Delta l} & \sigma_{y\Delta l} & \sigma_{y'\Delta l} & \sigma_{\Delta l}^2 & \sigma_{\Delta l\frac{\Delta p}{p}} \\ \sigma_{x\frac{\Delta p}{p}} & \sigma_{x'\frac{\Delta p}{p}} & \sigma_{y\frac{\Delta p}{p}} & \sigma_{y'\frac{\Delta p}{p}} & \sigma_{\Delta l\frac{\Delta p}{p}} & \sigma_{\frac{\Delta p}{p}}^2 \end{pmatrix}$$

The correlation between different moments is described by the off-diagonal elements σ_{ij}, with $i \neq j$ and $\sigma_{ij} = \sigma_{ji}$. The volume of the ellipsoid, i.e. the emittance, is determined by the determinant of the Σ matrix.

$$\varepsilon_{6D} = \sqrt{|\Sigma_{6D}|}. \tag{1.40}$$

In order to illustrate the characteristics the Σ matrix the 2 dimensional phase space (x, x') is used. This subspace is represented by the submatrix:

$$\Sigma_{(x,x')} = \begin{pmatrix} \sigma_{11} & \sigma_{12} \\ \sigma_{12} & \sigma_{22} \end{pmatrix}. \tag{1.41}$$

A graphical illustration is given in Fig. 1.6.

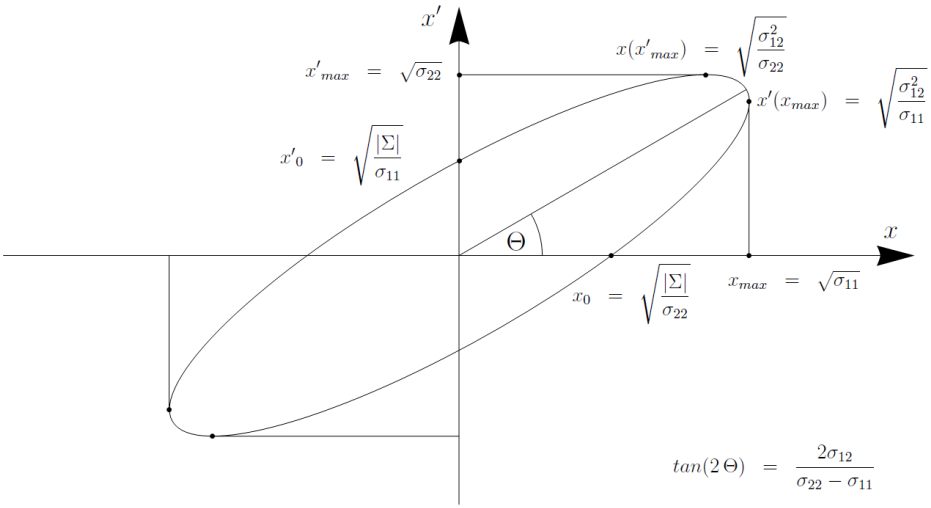

Figure 1.6: Two Dimensional Phase Space

Some characteristics of the Σ matrix elements are summarised in this plot. The beam size and beam divergence are defined by the matrix elements σ_{11} and σ_{22}. The orientation of the ellipse is determined by the correlation element σ_{12}. The area of the transverse phase space distribution, transverse emittance, is determined by the determinant of the $\Sigma_{(x,x')}$ matrix.

Horizontal beam size and beam divergence are determined by the matrix elements $\sigma_{11} = \sigma_x^2$ and $\sigma_{22} = \sigma_{x'}^2$. The orientation of the phase space ellipse is defined by the matrix element σ_{12}. The phase space area, emittance ε, is given by the determinant of the $\Sigma_{(x,x')}$ matrix,

$$\varepsilon_{x,x'} = \sqrt{\begin{vmatrix} \sigma_{11} & \sigma_{12} \\ \sigma_{12} & \sigma_{22} \end{vmatrix}}. \tag{1.42}$$

Similar to the transformation of single particle coordinates a transformation of the particle ensemble parameters is accomplished using the transfer matrix $R = R\,(S_0 \rightarrow S_1)$,

$$\Sigma\,(S_1) = R\,\Sigma\,(S_0)\;R^T. \tag{1.43}$$

1.2 Space Charge Effects

The "direct space charge effects"[1] are the direct interactions of charge particles with each other. Thereby, the particle distribution itself defines its internal field distribution. Differences between internal fields of different particle distributions have been observed at theoretical studies. In general it can be assumed that the space charge fields are characterised by non-linear field components. Therefore, a linear approximation of these fields is restricted to a limited fraction of the particle distribution, Fig. 1.7. However, as a similar development

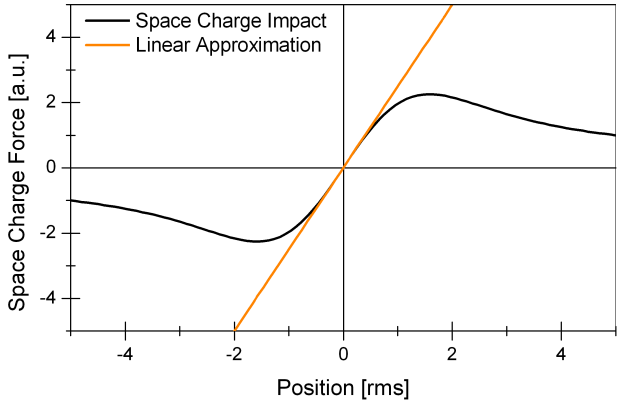

Figure 1.7: Space Charge Field of a Gaussian Distribution
In this figure the development of the space charge force depending on the transverse distance from the bunch centre in the units of rms beam size is plotted. A linear approximation of the space charge force is restricted to the minor fraction of the distribution below $r \leq 1\sigma_{rms}$.

of the rms beam size for different particle distributions was observed [20], several analytical beam models have been developed to estimate the influence of space charge on the development of charged particle beams. For the estimation of space charge effects in linear beam dynamics the "uniform beam" model is fundamental. In this model a six dimensional ellipsoid is used to represent a particle distribution, section 1.1.6. For the calculation of the space charge impact an uniform charge distribution inside the ellipsoid is assumed. Due to the uniform charge distribution an analytical determination of the space charge fields is possible [21]. Based on these fields the space charge force is determined by means of Eq. 1.2.
The space charge force depends strongly on the particle energy and scales with $F_{sc} \sim \gamma^{-2}$. It depends linearly on the charge density. Due to the uniform charge distribution the space charge force is linearly correlated to the particle position.

[1] "Indirect space charge" is the indirect interaction of charged particles with each other. Classical examples are wake-fields, at which a particle ensemble generates a charge variation in its environment, e.g. image charge at the beam pipe, which acts back on the particle ensemble and on following particle ensembles.

As a consequence the space charge force in the "uniform beam" model can be seen as a co-moving, defocusing field gradient, whose focusing strength $k^{sc}(s)$ is determined by the bunch dimensions.
Hence, the equation of motion for single particles[2] changes to:

$$x''(s) + (k_s(s) - k_x^{sc}(s))x(s) = 0, \tag{1.44}$$

where $k_s(s)$ corresponds to the focusing strength of beam optics elements such as quadrupole magnets and k^{sc} to the space charge defocusing. In order to illustrate the space charge impact on the beam optics a FODO lattice is chosen. The particle ensemble is a proton beam with transverse normalised rms emittance of $\varepsilon_x = \varepsilon_y = 0.3\,\pi\,mm\,mrad$ and a kinetic energy of $3\,MeV$.
The quadrupole field gradient is $g = 100\,T/m$, which corresponds to a quadrupole focusing strength of $k_{qf} = -k_{qd} = 400\,\frac{1}{m^2}$ or rather a focal length of $f = \frac{1}{k \cdot length} = 50\,mm$. In Fig. 1.8 the layout of one cell is illustrated.

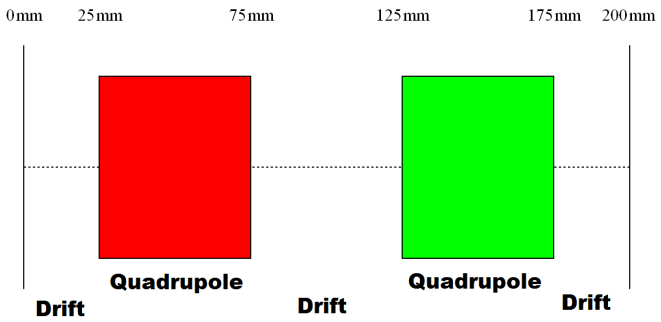

Figure 1.8: Layout of one FODO Cell
In order to illustrate the impact of space charge on the development of the transverse beam size an example lattice consisting of four FODO cells is chosen. The layout of one FODO cell is shown in this scheme. The red and green rectangles are representing the focusing and defocusing quadrupole magnets of a FODO cell.

Neglecting space charge effects the periodical solution is determined by the lattice itself, [17]. The initial transverse Twiss parameters are listed in Tab. 1.1.

$\beta_x = 0.15095\,m$	$\beta_y = 0.15095\,m$
$\alpha_x = -2.0665$	$\alpha_y = 2.0665$

Table 1.1: Twiss Parameters for the Periodical Solution
The Twiss parameters were defined based on the calculated transfer matrix of one FODO cell. Each FODO cell is characterised by a phase advance of $109\,deg$.

In Fig. 1.9 the development of the rms beam size neglecting space charge effects is plotted.

The results of analytical calculations with Trace3D [20], T3D, and the results

[2]In this example the coupling of the particle motion such as dispersion has been neglected.

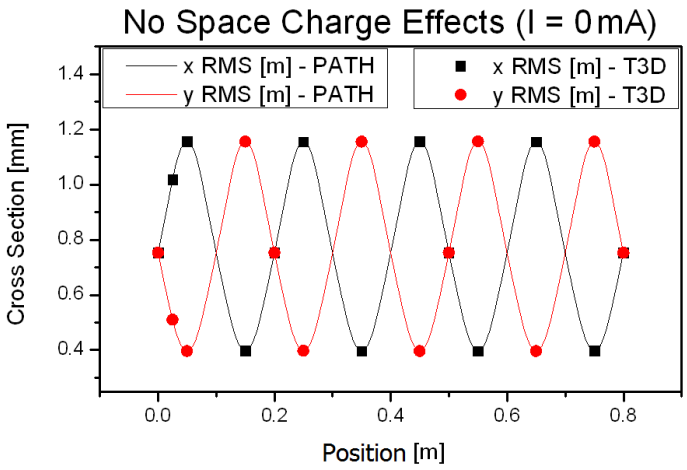

Figure 1.9: Development of the rms Beam Size (without space charge effects)
In this plot the development of the rms beam size along the FODO lattice is shown. Based on analytical calculations the initial Twiss parameters were defined, which lead to a periodical solution of the beam parameters.

of particle tracking simulations[3] with Path [22] are consistent, Fig. 1.9.
Due to the defocusing effect of the space charge force the periodical solution is disturbed. Depending on the beam current the grade of disturbance increases, as shown in Fig. 1.10.

The defocusing space charge fields are causing a mismatch between beam and lattice parameters leading to a strong beta beat. This beta beat is characterised by a modulation of the beam size over a certain number of FODO cells. In Fig. 1.10(3) the periodicity of the beta beat is two FODO cells. Although a strong variation of the beam optics is caused at higher beam currents, a good agreement between analytical calculations and the results of the particle tracking has been obtained, Fig. 1.10.
In the design of the Linac4 beam optics it is essential to adapt the beam optics to the expected space charge defocusing to avoid the generation of beta beats. Due to the beta beat the maximum transverse beam size increases, which leads to a higher potential of particle losses. Furthermore, this modulation of the transverse beam size leads in presence of intense space charge effects to an increase of the transverse emittance. During the optimisation of the transfer line optics this effect was observed, chapter 3.

[3] At the particle tracking the phase space distribution of a beam is represented by an ensemble of test particles characterised by identical beam parameters emittance and Twiss parameters. The motion of each test particle will be calculated. Based on the motion of the test particles the development of the beam parameters is determined.

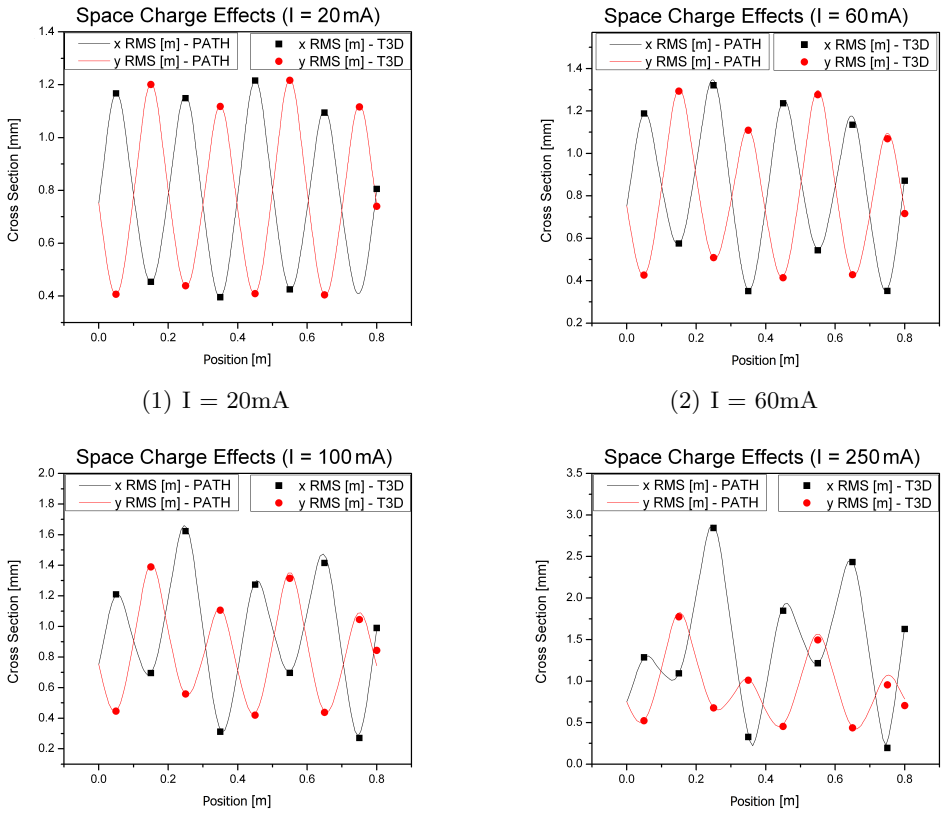

(1) I = 20mA (2) I = 60mA

(3) I = 100mA (4) I = 250mA

Figure 1.10: Development of the rms Beam Size (with space charge effects)
In this figure the development of the rms beam size along the FODO lattice influenced by space charge effects is shown. For the calculations the analytical code Trace3D, T3D, and the particle tracking code PATH were used. With increasing space charge impact a stronger disturbance of the design optics is caused. Also at significantly disturbed beam optics a good agreement between the results of the two simulation codes has been obtained.

1.2.1 Dispersion and Space Charge

" [..]The function $D\frac{\Delta p}{p}$ *determines the offset of the reference trajectory from the ideal path for particles with a relative energy deviation* $\frac{\Delta p}{p}$ *from the ideal momentum p.[..]"* [23]. Particles with momentum deviation propagate on paths whose transverse distance is determined by the amount of momentum deviation and the dispersion D, Eq. 1.8 and Eq. 1.9.
Internal fields such as space charge influence the motion of the single particles. Due to these internal fields the dependence between particle offsets from the ideal path and their momentum deviations changes. For the description of the development of phase space distributions internal fields have to be considered. This can be completed in a consistent approach by the definition of two different dispersion functions. As for the description of the development of phase space

distributions internal fields have to be taken into account, the impact of these fields has been implemented in the definition of an "internal dispersion" or "space charge dispersion",

$$\Delta x = D_x^{Space\,Charge} \frac{\Delta p}{p} \quad , \tag{1.45}$$

$$\Delta x' = D'^{Space\,Charge}_x \frac{\Delta p}{p}. \tag{1.46}$$

However, these internal fields are not changing the first order moments of the particle distributions such as average horizontal position $< x >$, average horizontal slope $< x' >$ or the average particle momentum p. For the calculation of the path of particle ensembles internal fields have to be neglected, which leads to the definition of the "external dispersion" as described in section 1.1.3, Eq. 1.8 and Eq. 1.9.
In summary for the definition of dispersion it is required to distinguish between single particle movement and the dynamics of particle ensembles. For the determination of the dynamics of particle ensembles it is necessary to define an "internal dispersion" $D_x^{SpaceCharge}$, as the effects of the bunch internal field distributions have to be considered. In addition to the internal dispersion the definition of an "external dispersion" is required to describe the path of a particle ensemble, which is characterised by a momentum deviation from the reference momentum. The external dispersion is determined by the magnetic structure of the accelerator and is independent of the particle distribution. A detailed discussion of this subject can be found in [24].

1.3 Space Charge Effects in Circular Accelerators

The main limitation towards higher proton flux intensity in the CERN accelerator chain is the impact of the space charge in the PS-Booster. As shown in chapter 1.2 the direct space charge effects are creating disturbances of the beam optics. The transverse space charge forces acting on a particle depend on its position. As a consequence each particle in the bunch is focused differently by means of the space charge effects. The main issue of the direct space charge effects is that due to their non-linear field distributions incoherent beam optics disturbances are caused, which leads to the generation of a tune spread. Instead of a defined tune a certain tune area is covered by the particle ensemble. The performance limitation is given by the size and position of this area. Fig. 1.11 shows the simulated tune spread of the PS-Booster at injection [25]. For the PS-Booster simulation beam parameters, which have been defined for the Linac4 injection, were used. The simultaneous increase of beam intensity and particle energy to Linac4 injection parameters leads to an equivalent space charge impact on the PS-Booster dynamics.

In order to illustrate and quantify the tune spread mechanism the linear space charge model introduced in section 1.2 is used. Due to the linear dependency between the space charge forces and the particle position in this model a shift

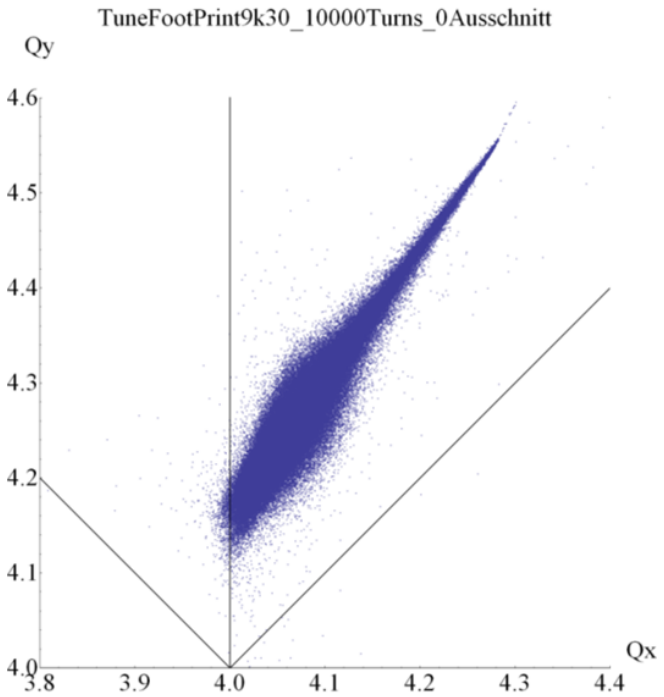

Figure 1.11: Simulated Tune Spread of the PS-Booster
In this plot a simulated PS-Booster tune spread is shown, [25]. For the simulation of this PS-Booster tune spread the Linac4 beam parameters have been used. Due to the simultaneous increase of particle energy and beam intensity the tune spread dimensions of the PS-Booster are preserved. Due to the non-linear space charge effects the PS-Booster tune is converted into a tune spread, which is limiting the PS-Booster performance.

of the tune instead of a tune spread will be generated. But, as the dependency between space charge forces, particle energy and beam current are maintained, the space charge tune shift formula can be used to estimate the development of the tune spread area for different beam currents and particle energies. In the following approach chromaticity and dispersion are neglected.
In the linear space charge model the defocusing strength is defined as [26]:

$$k_{sc} = -\frac{2r_0 I}{ec\beta^3\gamma^3 a^2} \quad \text{with} \tag{1.47}$$

$$r_0 = \frac{e^2}{4\pi\varepsilon_0 m_0 c^2}. \tag{1.48}$$

In this approach a round beam is assumed, i.e. $\sigma_x = \sigma_y$ and $a = \sqrt{3}\sigma_x$. As discussed the space charge force scales with the particle energy γ. In this formula the charge density is expressed by the beam current I in combination with the relativistic velocity β. In order to simplify the formula constants such particle charge e and particle mass m_0 were summarised to the particle radius r_0. To calculate the impact of space charge on the tune the tune shift formula [27] for

quadrupole gradient errors is used:

$$\Delta Q = \frac{1}{4\,\pi} \int_0^{2\pi R} \Delta K(s) \cdot \beta(s) \mathrm{d}s.$$

The gradient error ΔK is replaced by the space charge defocusing of Eq. 1.47,

$$\Delta Q = -\frac{1}{4\pi} \frac{2 r_0 I}{e \beta^3 \gamma^3 c} \int_0^{2\pi R} \frac{\beta(s)}{a^2} \mathrm{d}s. \tag{1.49}$$

Assuming that the transverse emittance is maintained constant during one turn the expression in the integral can be replaced by the transverse absolute emittance, $\varepsilon_{abs} = \varepsilon_n/(\beta\,\gamma)$. The beam current I is replaced by the number of particles N,

$$I = \frac{N \cdot q \cdot \beta c}{2\pi R}. \tag{1.50}$$

This leads to a compact expression of the space charge tune shift of:

$$\Delta Q = -\frac{r_0}{2\pi\varepsilon_n} \frac{N}{\beta\gamma^2}\ . \tag{1.51}$$

In this linear approximation the space charge effects lead to a coherent reduction of the tune, which depends on the number of particles, particle energy and the transverse normalised emittance ε_n.
Since in the approximation an uniform charge distribution of the particles is assumed, space charge forces are linearly dependent on the particle positions. A more realistic model is a Gaussian distribution. As shown in Fig. 1.7 this distribution leads to a non-linear dependence between space charge force and particle position. Hence, instead of a coherent tune shift an incoherent tune spread is expected. In Fig. 1.11 the simulated tune of the PS-Booster at injection is plotted. For its simulation a multi-particle tracking-code was used, which interpolates non-linear space charge fields.
The space charge tune shift using the linear space charge model and the space charge tune spread identically depend on the particle energy and particle density. Based on the Maxwell equations [16] a linear relation between field intensity and bunch charge is defined. The dependence between particle energy and space charge impact can be discussed in two different reference frames.
In the laboratory frame the motion of the charged particles leads to the generation of a magnetic field, which counteracts the repelling Coulomb force. The strength of the magnetic field is defined by the velocity of the charged particles, Biot-Savart law [16]. Hence, the space charge force scales with $F_{sc} = F_{coulomb}/\gamma^2$.
In the rest frame of the particle bunch the space charge force is defined by the

Coulomb force. Due to the velocity of the rest frame with respect to the laboratory system the Einstein time dilatation has to be considered leading to the identical dependency between space charge force and particle energy. So, the dependence between particle density, particle energy and space force is constant and independent from the particle distribution.
Consequently, the relation between tune shift, particle energy and particle density can be used to estimate the maximum bunch intensity of the PS-Booster using Linac4. The present PS-Booster injection energy is $50\,MeV$. The replacement of Linac2 with Linac4 as the injector for the PS-Booster leads to an increase of the injection energy to $160\,MeV$. As a result a doubling of the intensity of the PS-Booster bunches is expected.

At several sections of this thesis the presented theory is used to calculate the beam dynamics.
The linear beam optics without space charge effects is used to develop a first draft layout of the diagnostic line LBS foreseen for the measurement of the longitudinal beam parameters directly upstream of the PS-Booster injection. In the layout of the transfer line a debuncher cavity for the reduction of the beam energy spread is required. Due to the energy modulation of the Linac4 bunches the adjustment of the synchronous phase of the debuncher cavity, called phase swing, is needed. This phase swing has been calculated using the transfer matrix method.
For first calculations and optimisations of beam transfer sections such as the optimisation of the beam optics of the vertical chicane of the transfer line the linear space charge model was used. Further optimisations and beam dynamics studies were conducted using multi-particle tracking codes.
For the minimisation of the transverse emittance along the transfer line the interplay of dispersion and space charge had to be considered, see section 1.2.1.

2

Investigations at the 3 MeV Test Stand

The beam dynamics of the low-energy front-end components of Linac4 is in particular crucial for the quality of the final beam. These components will be commissioned at a special test stand, the $3\,MeV$ Test Stand[1]. In the scope of the $3\,MeV$ Test Stand commissioning is the test and performance optimisation of the low-energy front-end elements of Linac4, which are the H^- ion source, Low Energy Beam Transport (LEBT), Radio Frequency Quadrupole (RFQ) and Medium Energy Beam Transport (MEBT). The commissioning is sequentially performed starting with the commissioning of the H^- ion source.
The H^- ion source is based on the design of the H^- ion source of DESY (Hamburg) [14]. In a first phase of the source commissioning the Linac4 source parameters were adapted to the source parameters of DESY (Hamburg) to benchmark its performance. This source commissioning phase is successfully completed [28][29].
In order to increase the H^- ion beam current the extraction voltage is increased from $35\,kV$ (DESY source) to $45\,kV$ (CERN Linac4 source). Due to technical reasons it was decided to change the source operation mode at $45\,kV$ extraction voltage. The further Test Stand commissioning was conducted using proton beams, which are characterised by a significantly higher beam current at similar transverse emittances[2]. In the framework of this thesis detailed characterisations of the source beams for different source settings were conducted. The investigation of the beam characteristics at different source settings is essential for the reconstruction of the beam dynamics and these measurements are fundamental of the commissioning of the downstream accelerator elements.
Downstream of the source exit a LEBT is used to match the beam from the source to the RFQ conducted by means of two solenoid magnets. The two solenoids of the final Linac4 LEBT are identical and characterised by an aperture of $r = 100\,mm$. For the $3\,MeV$ Test Stand commissioning a temporary LEBT is used, whose layout is similar to the final one. The aperture limitations of the solenoids of the temporary LEBT are smaller with respect to the final Linac4 solenoids leading to a reduced acceptance.
The LEBT commissioning was performed in 2 stages. In the first stage the first solenoid and diagnostic vessel were assembled. The goals of this measurement

[1] The name is based on the fact that all Linac4 components with particle energies below $3\,MeV$ will be commissioned at this test stand.

[2] The major difference between the two operation modes is the polarity of the extraction voltage. Due to the change of the voltage polarity negative charged particles such as electrons and H^-ions are confined in the plasma vessel and the extraction of positive charged particles is enhanced. In addition to neutral particle, whose extraction is not influenced by the extraction voltage, protons, H_2^+ ions and H_3^+ ions are extracted from the source.

campaign are the investigation of the space charge compensation, the determination of the solenoid scaling factors and in combination with a spectrometer diagnostic line the examination of the energy spread. As amongst protons H_2^+ ions and H_3^+ ions are simultaneously extracted from the source, the spectrometer measurements are used to determine the relative population of these particle species.
In the second phase the Test Stand LEBT was completely assembled. The investigation, optimisation and reconstruction of the beam dynamics are in the focus of this phase conducted in the framework of this thesis. A theoretical model of the LEBT beam dynamics was developed based on the measurements at the source exit and downstream of the first solenoid. At the second phase further emittance measurements and beam current measurements were conducted, which are used to reconstruct the LEBT beam dynamics and to complete its beam dynamics model. Further characteristics of the LEBT beam dynamics are obtained by the simultaneous variation of the source and LEBT settings. In addition to the reconstruction of the beam dynamics these measurements are used to determine the LEBT acceptance.
In the context of this thesis the preparation measurements for the RFQ commissioning are conducted. The first part of this preparation consists of the identification of LEBT settings, at which the beam is matched to the RFQ. Several settings with different LEBT transmission were determined.
In order to identify and compensate possible alignment errors additional preparation measurements were performed. In the case of longitudinal alignment errors the matching plane of the RFQ changes. It is foreseen to compensate this change by an adjustment of the focusing of the second solenoid. Transverse alignment errors will be compensated by means of two pairs of steerer magnets installed in between the two solenoid magnets. The applied beam deflection is re-directed by the focusing impact of the second solenoid. In oder to identify transverse alignment errors the transverse phase space motion of the beam centre at the RFQ entrance in dependence of the steerer magnet settings is recorded and summarised in a so called 'Steerer Map'.
A special feature of the Linac4 LEBT is the low energy iris used to collimate the transverse phase space. This allows the generation of special probe beams, so called pencil beams, which are characterised by lower beam currents and smaller transverse emittances. It is foreseen to use these beams to detect alignment errors and examine the Linac4 acceptance, [30]. Due to the reduced emittance of these probe beams a higher RFQ transmission is expected. The Twiss parameter matching remains crucial in terms of transverse emittance preservation, which allows the simultaneous tuning of the probe beam current and emittance downstream of the RFQ.
The commissioning of the RFQ and chopper section is ongoing and is beyond the scope of this thesis.

2.1 Source Commissioning

For the design of the LEBT and of the RFQ several assumptions in terms of expected source beam current and phase space distribution are required. Based on these assumptions the accelerator parts were developed and optimised. With the measurement of the phase space distribution, beam current, extraction energy and energy spread most of the hypothesized beam characteristics are determined.
The beam current extracted from the Linac4 source is a major parameter. The source is designed to generate negative-charged hydrogen-ion beams with a flat-top beam current from $80\,mA$ to $90\,mA$ [14]. Its design is based on the Caesium-free volume source of DESY (Hamburg). The extraction voltage of the DESY source is $35\,kV$. By raising the extraction voltage from $35\,kV$ to the Linac4 nominal voltage of $45\,kV$ an enhancement of the H^- ion beam current is expected.
Due to technical reasons the operation mode of the Linac4 source was changed to generate proton beams at the extraction voltage of $45\,kV$. These proton beams are characterised by a similar transverse phase space distribution[3]. The performance of the Linac4 source is defined by the interplay of hydrogen gas flux[4] and RF-power in the plasma volume of the source.
In the end of 2010 a first characterisation of the proton beams at the source exit was completed. At this investigation a stable source operation was obtained by the manual adjustment of the source settings. In the framework of this thesis an implemented stabilisation system for the hydrogen gas injection was conditioned. Due to this stabilisation system a sensitive tuning of the source performance is possible and a high reproducibility of the source performance conditions is obtained. At the end of 2011, i.e. after one year of operation, it was decided to re-check the beam parameters at the source exit. Variations from the measured parameters were expected caused by source damages induced by operational effects such as antenna sparking[5] and the interaction of the extracted particles with the material of the extraction cathode. It was expected that the source damages might caused a variation of the source beam parameters. In the framework of this thesis a new characterisation of the source beam parameters was accomplished, which due to the improved stabilisation system is marked by a high reproducibility.

[3] During the source commissioning with an extraction voltage of $35\,kV$ the transverse phase space of H^- ion beams and proton beams were measured and similar emittances and Twiss parameters for H^- ion beams and proton beams were observed.
[4] This parameter is influenced by external parameters. E.g. a change of the temperature inside the source cage changes the characteristics of the piezo valve, which is used to regulate the hydrogen gas injection.
[5] Inside the source an antenna is used to transmit the $2\,MHz$ RF-power to the plasma. At certain configurations of the source sparkings of the antenna can be affected.

2.1.1 Beam Current Measurements

For the beam current measurement a Faraday cup was mounted at the source exit, Fig. 2.1(2). A drawing of the Faraday cup is presented in Fig. 2.1(1).

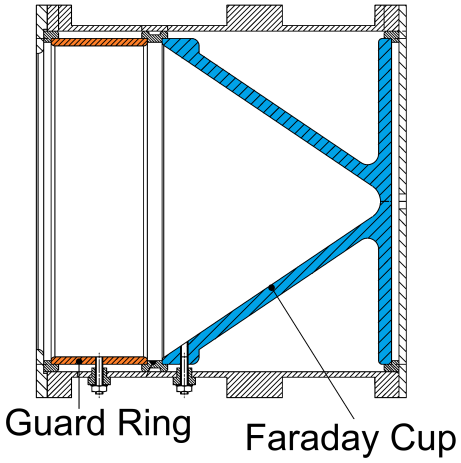

(1) Faraday Cup Drawing

(2) Faraday Cup mounted at Source Exit

Figure 2.1: Faraday Cup

In figure (1) the schematic of a Linac4 Test Stand Faraday cup is shown. The Guard ring (red) is used to suppress the secondary electron emission, which is caused by the impact of the proton beam in the Faraday cup (blue). Figure (2) shows a photo of this Faraday cup mounted at the source exit. Photo provided by [31].

Due to the impact of the extracted particles onto the Faraday cup material electrons are emitted [32]. The secondary electron emission from the Faraday cup is suppressed using an opposing field. This field is generated by a potential step between Faraday cup and Guard ring, which is mounted upstream of the Faraday cup.

Old Beam Current Measurements

In the focus of the measurement campaign was the examination of the source performance at different source settings. The beam current was measured in dependence of the source parameters source RF-power and the hydrogen gas flux [33], Fig. 2.2.

At the measurements the impact of the hydrogen gas flux was studied in two different regimes, namely low gas flux regime and high gas flux regime. In the low gas flux regime the hydrogen flux is minimised within stable source operation. At the high gas flux regime the gas injection was manually regulated above the minimal required hydrogen gas flux. Based on the reduction of the beam current and a simultaneously detected increase of the reflected RF-power it was concluded that an increase of the hydrogen flux disturbs the interplay

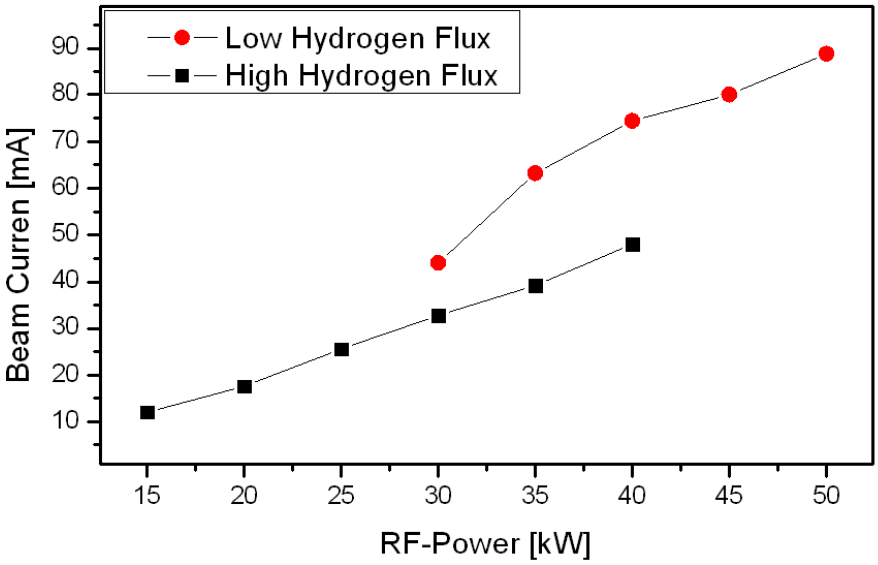

Figure 2.2: Faraday Cup Signals for different Source Settings (2010)
This plot shows the Faraday cup signals measured at the source exit. The data was recorded at the end of 2010. Two different regimes of hydrogen flux regulations are plotted, namely high hydrogen flux regime and low hydrogen flux regime. In the low flux regime the coupling between RF-power and plasma is optimised. An increased hydrogen flux leads to a degradation of the coupling, indicated by an increase of the reflected RF power and the decrease of the detected beam current. At the two regimes a linear dependence between RF-power and beam current is observed.

between RF-power and plasma.
In the high hydrogen flux regime and in the low hydrogen flux regime a linear dependence between RF-power and Faraday cup signal is observed. The maximum Faraday cup signal is in the order to $90\,mA$. In addition to protons H_2^+ ions and H_3^+ ions are extracted from the source. In a later phase of the $3\,MeV$ Test Stand commissioning the ratio of the different particle species was measured: $H_1^+ : H_2^+ : H_3^+ = 70 : 15 : 15$, [34]. Hence, a maximum proton beam current of approximately $60\,mA$ to $65\,mA$ is determined.

New Beam Current Measurements

After one year of source operation the source beam parameters transverse emittance and beam current were re-measured. For the new measurement an identical measurement setup was used. Due to the improved stability system a sensitive calibration of the hydrogen flux is possible. Basic element of the upgraded stability system is a feedback loop (fbl) used to control the gas injection valve and to regulate the gas injection according to gas pressure readings at the source recipient. A higher fbl value corresponds to a higher hydrogen flux.

The beam current was measured in the source RF-power range from $10\,kW$ to $60\,kW$ for three different hydrogen flux settings. A minimised hydrogen gas flux within stable source operation was obtained at a fbl value of $6.95V$[6]. At the two hydrogen flux settings of fbl $7.00\,V$ and $7.05\,V$ the hydrogen flux was slightly increased. A degradation of the plasma RF-power coupling and reduction of the beam current was observed, Fig. 2.3.

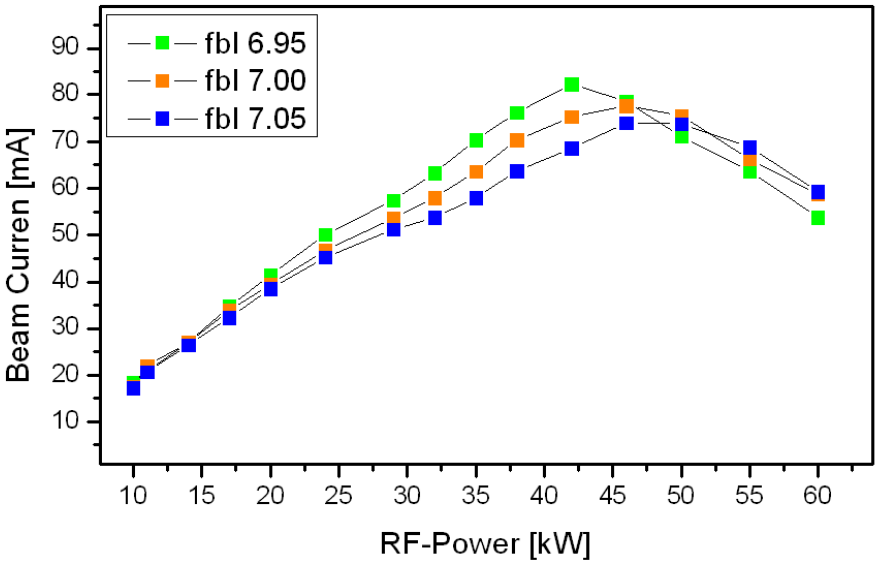

Figure 2.3: Faraday Cup Signals for different Source Settings (2011)
In this plot the results of the new Faraday cup measurements are summarised. By means of a feedback loop system (fbl) the hydrogen flux was controlled. With increasing hydrogen flux a reduction of the beam current was obtained. The reduction of the Faraday cup signal with increasing RF-power is most likely caused by an unwanted interaction of the protons with the Faraday cup Guard ring. Measurements of the source capacitor current indicate a further increase of the extracted beam current with increasing RF-power. Due to the fbl stabilisation system a high reproducibility of the measurements results is obtained.

In the RF-power range from $10\,kW$ to $40\,kW$ the Faraday cup signal increases linearly with the source RF-power, which was also observed at the old beam current measurements. Above a RF-power of $40\,kW$ a decreasing Faraday cup signal at increasing RF-power is detected. Measurements of the reflected source RF-power and of the current of the source capacitor, which is used to hold the extraction voltage during beam extraction, indicate a further increasing beam current. Based on detailed analyses of the measurement setup and of the recorded data the following explanation model was developed.
As shown in chap. 2.1.2 the beam size and divergence at the source exit increase

[6] A quantification of the fbl value is not possible, as its value is defined by the volume of the vacuum vessel, the pumping speed of the vacuum pumps and by the hydrogen injection flux.

with increasing RF-power. An enhanced hydrogen flux causes a degradation of the plasma RF-power coupling and leads to a lower beam current within a reduction of the beam size and the beam divergence.
In order to suppress the emission of secondary electrons the Faraday cup is equipped with a Guard ring, which is set on a high potential to capture emitted electrons inside the Faraday cup. Readings of the Guard ring potential indicate that at the decreasing Faraday cup signals with increasing RF-power fractions of the source beam are interacting with the Guard ring material, which causes the reduction of the Faraday cup signal. With further increasing RF-power the fraction of interacting particles increases causing an amplification of this process.
In Fig. 2.4 the results of the two beam current measurement campaigns are plotted.

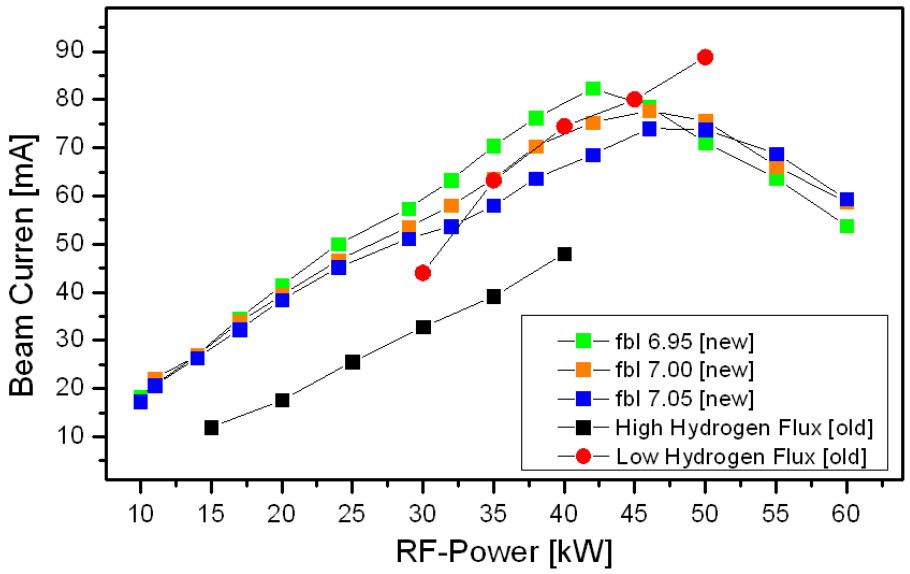

Figure 2.4: Faraday Cup Signals - 2010 & 2011
In this plot Faraday Cup measurements from 2010 and 2011 are summarised. A good agreement between the new measurements with the low hydrogen measurements of 2010 is observed. As the stabilisation system of the measurement campaigns differs, small variations are expected. It is concluded that no significant variations of the source output beam current is caused by the source operation of one year.

In the RF-power range from $10\,kW$ to $40\,kW$ the beam current measurements of the low hydrogen flux regime are in the measurement spectrum of the later investigations, which verifies that the source performance in terms of beam current is mainly preserved.

2.1.2 Beam Emittance Measurements

The beam emittance is defined as the phase space volume projected on a 2-dimensional coordinate system, e.g. position x and angle x'. As the reduction of the phase space volume is limited by conservation laws the emittance is an indicator of the beam quality.
A first examination of the proton beam emittance of the Linac4 source was conducted in the end of 2010. The measurement results present the baseline for the further Test Stand commissioning and their corresponding simulations. In the framework of this thesis a new, more detailed characterisation of the transverse phase space distribution was performed in 2011 with the aim to examine the dependence between beam emittance and source settings and to investigate the impact of one year operation time on the source performance.

Measurement Layout

The transverse emittance measurements are performed using a slit SEM-Grid combination, Fig. 2.5.

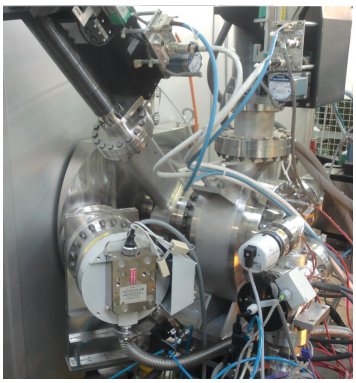

(1) Emittance Meter mounted at the Source Exit

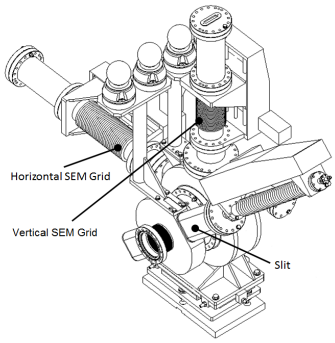

(2) Scheme of the Emittance Meter

Figure 2.5: Emittance Measurement Device at the Source Exit
Figure (1) shows the Linac4 emittance meter mounted at the source exit. At figure (2) a schematic of the emittance meter is presented. It consists of a double slit, one vertical slit and one horizontal slit , and two SEM-Grids, one vertical SEM-Grid and one horizontal SEM-Grid.

At the emittance measurements a projected phase space distribution is recorded. Due to the collimating impact of the slit a spatial fraction of the phase space is isolated, Fig. 2.6(1). The angular distribution related to the selected spatial beam fraction is projected onto and measured using the SEM-Grid, Fig. 2.6(2).

The motions of the slit and SEM-Grid of the emittance meter are limited to $S_{slit} = \pm 35\,mm$ and $S_{SEM} = \pm 70\,mm$ defining a spatial scan range of $\pm 35\,mm$. The angular scan range is determined by the correlated motions of slit and SEM-Grid. The measurement interface allows two kinds of scan modes. In the first

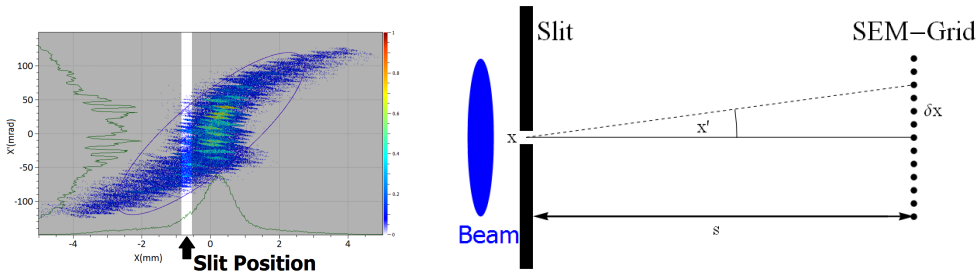

(1) Angle Mapping at separated spatial distribution

(2) Angle Determination

Figure 2.6: Working Principle of the Slit-SEM-Grid Emittance Meter
The collimating impact of the slit is used to isolate a spatial fraction of the beam. Due to the drift between slit and SEM-Grid the beam angular distribution is projected onto the SEM-Grid.

mode the SEM-Grid motion is linked to the motion of the slit, so called 'fast scan', e.g. Fig. 2.7(1). At each measurement position of the slit one SEM-Grid position is defined. This scan mode was used for the emittance measurements at the LEBT exit and for performing pre-scans to determine the required scan range. In the second scan mode the slit motion and the SEM-Grid motion are independently determined by a user-defined input file. This emittance scan mode allows to conduct emittance measurements with significantly increased measurement resolutions, so called 'detailed scan', e.g. Fig. 2.7(2).

Old Emittance Measurements

The aim of the first emittance measurement campaign conducted at the end of 2010 was the characterisation of the transverse phase space distribution, i.e. the measurement of the transverse emittance and the transverse Twiss parameters α and β. This data is required to simulate the LEBT beam dynamics and to benchmark the source simulation codes.
As mentioned the source beam consists of protons, H_2^+ ions, H_3^+ ions and neutral particles. Apart from the neutral particles the kinetic energy of the extracted particles is determined by the extraction voltage. Due to the different rest masses the particle species are separated in the momentum space. In between the source exit and the emittance meter no momentum sensitive beam optics element is installed, at which the measured phase space distributions of the four different particle species overlap, Fig. 2.7.
It is assumed that each of the particle distributions, i.e. protons, H_2^+ ions and H_3^+ ions, is characterised by the measured transverse emittances and Twiss parameters. The emittance values and Twiss parameters are reported in Tab. 2.1.

The normalised emittances are in the range from $\varepsilon = 0.4\pi\,mm\,mrad$ to $\varepsilon = 0.65\pi\,mm\,mrad$. This variation was expected, as at these measurements the source settings such as the source RF-power and the source hydrogen flux were

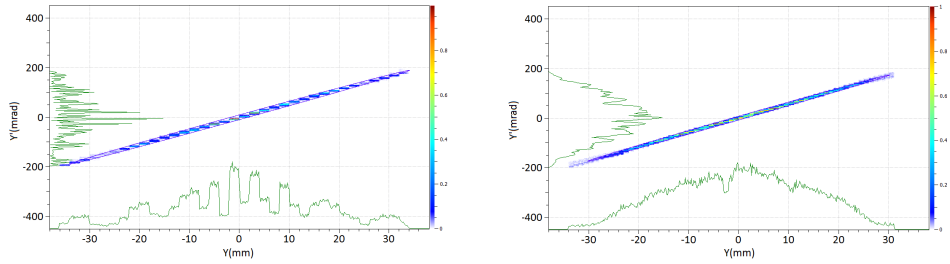

(1) Phase Space Plot vertical Plane 08.Oct.2010

(2) Phase Space Plot vertical Plane 18.Oct.2010

Figure 2.7: Phase Space Plot - Measurements 2010
This figure shows two measured phase space distributions. At the measurement (1) [08.Oct.2010] the 'fast scan' mode was used with a spatial resolution of $\Delta y = 1\,mm$. The measurement (2) [18.Oct.2010] was conducted using the 'detailed scan' method, at which a spatial resolution of up to $\Delta y = 0.1\,mm$ and higher measurement resolutions of the angle distribution are possible.

Scan Date	$\varepsilon_x(norm)$ $[mm\,mrad]$	α_x	β_x $[m]$	$\varepsilon_y(norm)$ $[mm\,mrad]$	α_y	β_y $[m]$
08.Oct.2010	0.53	-16.2	3.0	0.64	-19.7	3.55
14.Oct.2010	0.56	-23.2	4.3	0.57	-23.2	4.2
18.Oct.2010	0.44	-22.1	3.9	0.46	-22.5	3.9
20.Oct.2010	0.43	-20.2	3.6	0.49	-21.2	3.7

Table 2.1: Emittance and Twiss Parameters measured at the Source Exit - 2010
In this table typical beam parameters determined at the emittance measurement campaign of 2010 are summarised. For the computation of the Twiss parameters and transverse emittances a back ground threshold of 0.1 ‰ was used. The variations of the beam parameters are dominantly caused by two effects. These effects are different settings of the source and the different measurement settings. A detailed investigation of the impact of the source settings on the phase space distribution was performed in the framework of this thesis at the end of 2011. In Fig. 2.7 two phase space plots are shown to illustrate the impact of different measurement configurations.

altered. In spite of the significant variation of the transverse emittance only minor variations of the Twiss parameters are observed, apart from the measurements of 08.Oct.2010. In Fig. 2.7 the measurements 08.Oct.2010_y(1) and 18.Oct.2010_y(2) are plotted. The discrepancies of the Twiss parameters are enhanced by the measurement settings, which were still in the optimisation process at the measurement 08.Oct.2010.

New Emittance Measurements

In the end of 2011 the beam parameters at the source exit, i.e. transverse emittance and beam current, were re-investigated. One aim was the detailed investigation of the transverse emittance depending on the source parameter space, which is essential for the detailed understanding of the LEBT beam dynamics.

These measurements were also used to examine the impact of source damages, which are caused by the operation of one year, on the source performance in particular on the phase space distribution.
The new emittance measurement campaign was divided into two measurement campaigns. In the first measurement campaign the dependence between source RF-power and transverse emittance was examined. For this purpose measurement series with constant hydrogen flux were performed. The measurement results show that beams generated at higher RF-power levels are characterised by an increased transverse emittances. In Tab. 2.2 relevant results of one measurement series are reported.

RF Power / Scan Date	$\varepsilon_x(norm)$ $[mm\,mrad]$	α_x	β_x $[m]$	$\varepsilon_y(norm)$ $[mm\,mrad]$	α_y	β_y $[m]$
$30kW$						
25.Oct.2011	0.42	-26.5	4.7	-	-	-
02.Nov.2011	0.44	-23.1	4.1	0.42	-23.6	4.1
$40kW$						
25.Oct.2011	0.51	-27.3	5.0	-	-	-
03.Nov.2011	0.5	-27.3	5.0	0.46*	-25.5*	4.6*
$50kW$						
24.Oct.2011	0.66	-25.7	4.9	0.64	-25.8	4.8
24.Oct.2011(2)	0.66	-25.3	4.8	-	-	-
01.Nov.2011	0.64	-22.2	4.2	-	-	-

Table 2.2: Emittance and Twiss Parameters measured at the Source Exit - 2011
This table summarises characteristical emittance measurement results of 2011. With increasing RF-power an increase of the transverse emittance is observed. The increase of the hydrogen flux (measurement 03.Nov.2011-vertical plane) leads to a reduction of the beam emittance. The horizontal and vertical phase space distributions are similar. Due to the improved source stability system a high reproducibility of the measurement results is obtained.*

The increase of RF-power leads to an increase of the transverse emittance. The measured emittance values are in the range from $\varepsilon = 0.4\,\pi\,mm\,mrad$ to $\varepsilon = 0.66\,\pi\,mm\,mrad$, which agree to the emittance measurement results of 2010.
In the second measurement campaign the impact of the hydrogen flux on the transverse emittance was studied, for which additional measurements with increased hydrogen flux levels were conducted. Based on the measurement results it is verified that an increased hydrogen flux causes a reduction of the transverse emittance in combination with a reduction of the beam current. In Tab. 2.3 typical measurement results of one measurement series are summarised.
The transverse phase space measurement results indicate that an increase of the beam current is related to an increase of the transverse emittance and in particular with an enhanced population of the distribution tails, which was predicted based on beam current measurements at the LEBT commissioning phase II. An example is shown in Fig. 2.8.

In summary the beam parameters beam current and transverse emittance are strongly correlated and determined by the source settings RF-power and hydrogen flux. A maximum proton beam current of approximately $60\,mA$ was mea-

fbl Value (Hydrogen Flux)	**Emittance** $[\pi\, mm\, mrad]$	α	β $[m]$
7.1	0.78	-19.3	3.72
7.2	0.68	-20.3	3.92
7.3	0.62	-19.7	3.77
7.4	0.58	-18.0	3.45

Table 2.3: Impact of the Hydrogen Flux on the Beam Phase Space
In this table the measurement results of a measurement series with a constant source RF-power of $40\,kW$ *and varying hydrogen flux are listed. The increase of the hydrogen flux leads to a reduction of the beam emittance. The transverse Twiss parameters are preserved.*

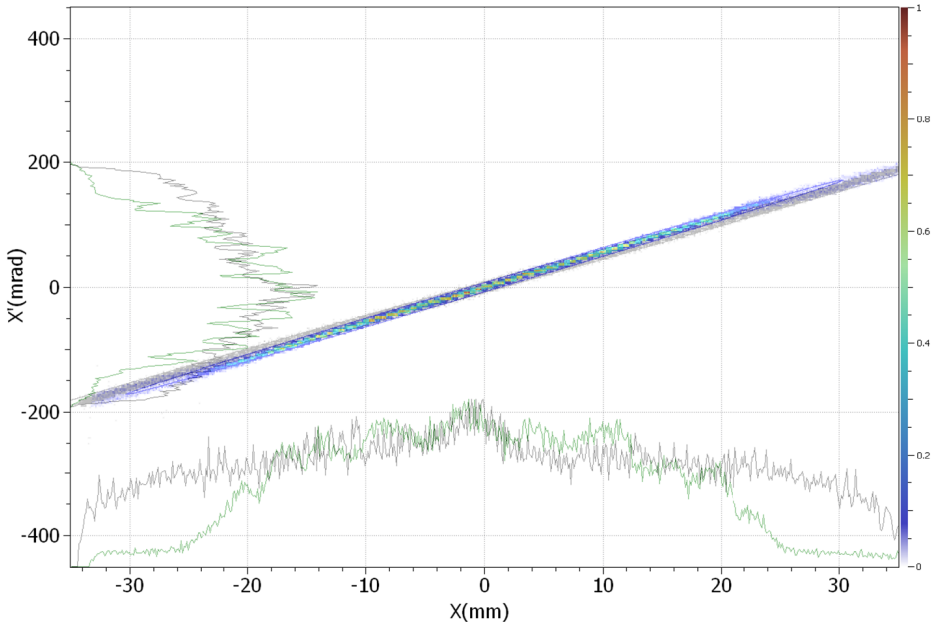

Figure 2.8: Transverse Phase Space Distributions of different Source Settings
In this diagram two measured phase space distributions are plotted. For these measurements the source RF-power has been varied from $30\,kW$ *(colour) to* $50\,kW$ *(monochrome). The hydrogen flux was maintained. Due to the increase of RF-power an enhanced population of the distribution tails of the transverse phase space is caused, which leads to higher emittance values.*

sured. The transverse phase space distribution in horizontal and vertical plane is similar with transverse emittance values in the range from $\varepsilon = 0.4\,\pi\, mm\, mrad$ to $\varepsilon = 0.66\,\pi\, mm\, mrad$. Although small variations of the transverse Twiss parameters between old and new measurements were detected, no significant changes of the source performance are observed. In Fig. 2.9 a comparison of an old phase space distribution with a new one is shown.

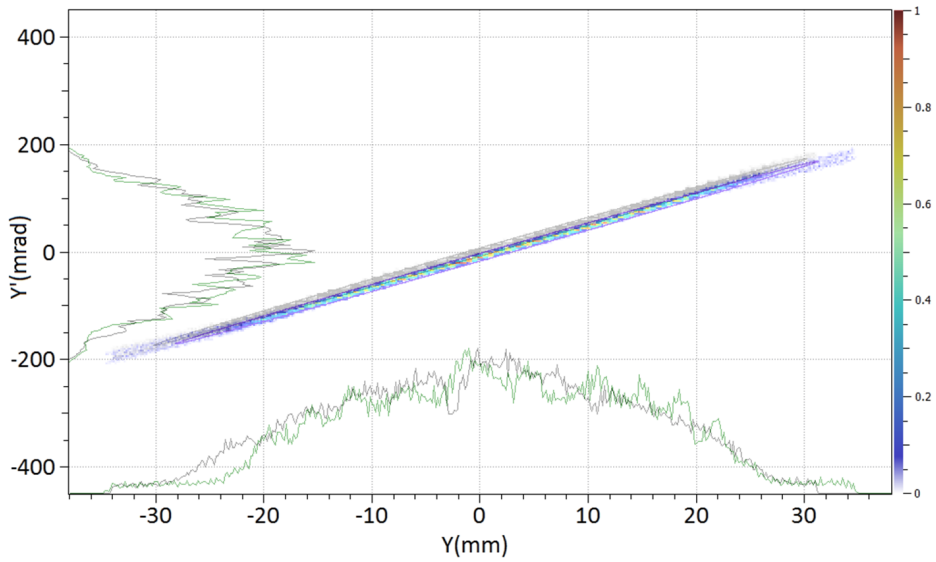

Figure 2.9: Phase Space Distribution - Old Vs. New Measurement
In this figure the phase space distribution of two measurements are plotted. The monochrome displayed distribution shows an old measurement [18.Oct.2010]. The coloured displayed distribution represents a later measured phase space distribution [02.Nov.2011 - vertical plane 30kW RF-power]. Apart from signal jitter the two distributions agree in phase space area, beam size, beam divergence and orientation of the phase space area.

Reference Beam Characteristics

In order to design the layout of the LEBT assumptions of the beam characteristics are required. These assumptions are combined into a test beam, so called reference beam. Based on the beam characteristics of the H^- ion source of DESY (Hamburg) the characteristics of the reference beam were defined.
At the source exit a H^- ion beam current of $80\,mA$ is defined. The measured beam current is in the range from $60\,mA$ to $100\,mA$ corresponding to a proton beam current in the range of $42\,mA$ to $70\,mA$.
The transverse phase space of the reference beam is symmetrical in the two planes, i.e. horizontal and vertical emittance and the Twiss parameters are identical. As the measurement plane is located $100\,mm$ downstream of the initial position of the LEBT simulation, the reference beam parameters are tracked to the measurement plane. At the measurement plane the reference beam is characterised by $\beta_x = \beta_y = 0.9\,m$ and $\alpha_x = \alpha_y = -10.77$. An increase of the transverse emittance was not been observed at the simulations. The transverse emittance of the reference beam is conserved at $\varepsilon_x = \varepsilon_y = 0.25\,\pi\,mm\,mrad$.
The emittance measurements at the source exit showed that the beam emittance varies from $\varepsilon = 0.4\,\pi\,mm\,mrad$ to $\varepsilon = 0.7\,\pi\,mm\,mrad$ depending on the source settings. In addition to the higher transverse emittance the orientation of the measured phase space distributions significantly differs. In order

to illustrate these discrepancies the transverse phase space distributions of the reference beam (colour) and of a measured beam (monochrome) are plotted in Fig. 2.10.

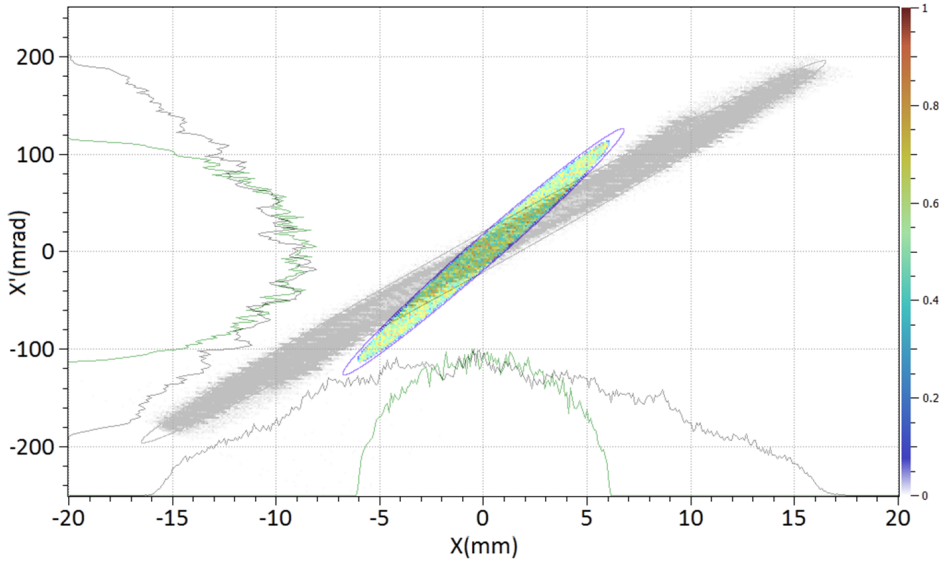

Figure 2.10: Reference Beam and Measured Beam

This plot shows the reference-beam phase-space-distribution (colour) and the phase space distribution of the measured source-beam (monochrome). The measured beam is characterised by a significantly larger beam size and beam divergence leading to a higher potential of particle losses along the LEBT.

In order to quantify the beam quality the beam parameter Brilliance B is used. At this parameter the beam properties beam current I, transverse emittance ε_x, ε_y and momentum spread δ_{rms} are combined [18],

$$B = \frac{I}{\pi\varepsilon_x \, \pi\varepsilon_y \, \delta_{rms}}. \tag{2.1}$$

In the first phase of the LEBT commissioning momentum spread measurements were conducted indicating that the beam momentum spread corresponds to the specifications. Hence, for the comparison of the beam quality the momentum spread δ_{rms} in Eq. 2.1 is set to 1. In Tab. 2.4 the brilliance with $\delta_{rms} = 1$ of the source beams are reported.
The measured beam brilliances amounts to less than 20% of the reference beam brilliance. At higher beam current outputs a reduction of the beam brilliance due to the increase of transverse emittance is observed.

Beam	**Emittance** ε $[\pi\ mm\ mrad]$	**Beam Current** **I** $[mA]$	**Brilliance** $[\frac{mA}{(\pi\ mm\ mrad)^2}]$
Reference	0.25	80	130
30kW RF-power	0.42	42	24.1
40kW RF-power	0.5	55	22.3
50kW RF-power	0.65	70	16.8

Table 2.4: Source Beam Parameters - Summary
This table summarises the beam brilliance of the source beams with momentum spread set to $\delta_{rms} = 1$. The increase of the RF-power leads to an increase of the two beam parameters beam current and transverse emittance. The simultaneous increase of these parameters leads to a decrease of the beam brilliance. The measured beam brilliances amount to less than 20% of the beam brilliance of the reference beam.

2.2 LEBT

The commissioning of the Linac4 Test Stand LEBT consists of two parts, LEBT commissioning part I and part II. In the first commissioning step the beam characteristics were measured downstream of the first solenoid. Due to the solenoid field the different particle species are separated in phase space. This permits a more precise determination of the proton beam emittance. For the simulation of the LEBT beam dynamics the field distributions of the solenoid magnets were analytically modelled using Poisson/Superfish [35]. At the second commissioning part the LEBT was completely assembled. The aim of this commissioning phase is the preparation of the RFQ commissioning and the reconstruction of the beam dynamics. Based on the reconstructed beam dynamics theoretical studies of the LEBT performance were conducted. In the focus of these studies is the optimisation of the beam transmission within acceptable RFQ matching. In addition to the theoretical beam matching an empirical beam matching was completed. Thereby, several LEBT settings were identified characterised by different LEBT transmissions, which can be used to adjust the RFQ input beam current.

2.2.1 Why is a LEBT needed?

The Low Energy Beam Transport, LEBT, located between source and RFQ, is used to match the beam to the RFQ. The RFQ matching parameters are pre-defined by the high phase advance lattice of the RFQ. Due to the high beam intensity in combination with the high phase advance lattice of the RFQ intense space charge effects along the RFQ are expected. The intensity of the space charge effects determined by the combination to the transverse emittance and the beam current is considered by an adjustment of the matching parameters. In Tab. A.1 the optimised RFQ matching parameters are listed [34]. In order to illustrate the different beam characteristics at the source exit and at the RFQ entrance the phase space distributions of the measured source beam (monochrome) and of a beam perfectly matched to the RFQ (colour) are plotted in Fig. 2.11. This beam transformation has to be accomplished by the LEBT optics.

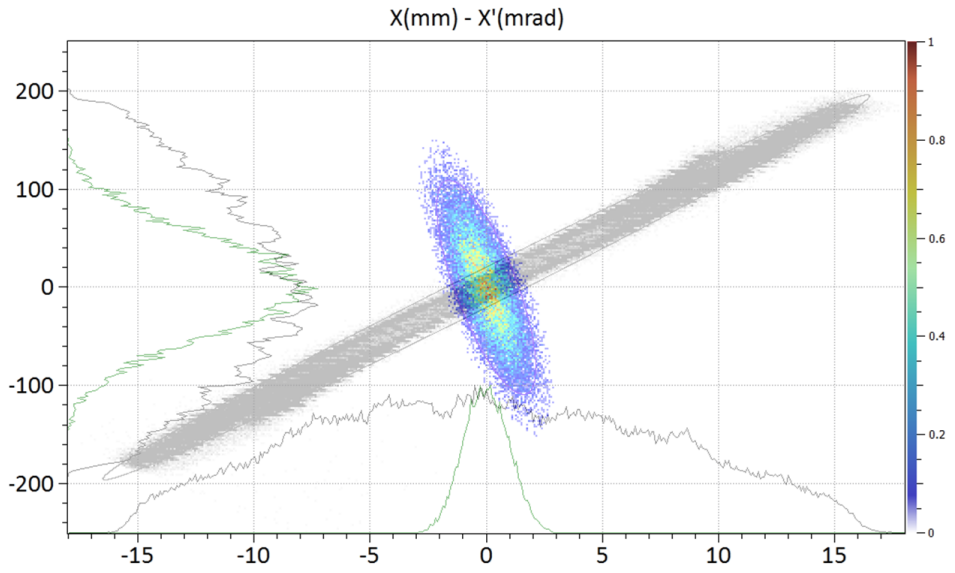

Figure 2.11: Source Beam Vs. RFQ-matched Beam

This plot shows the transverse beam phase space distribution at the source exit (monochrome) and a perfectly RFQ-matched phase-space-distribution (colour). At the source exit the beam is divergent. At the RFQ entrance a focused convergent beam is required for the high phase advance lattice of the RFQ. The transformation of the beam parameters has to be accomplished by means of the two solenoid magnets of the Linac4 LEBT.

2.2.2 LEBT Layout and Beam Optics

Layout

The function of the LEBT is to match the beam to the RFQ. Under the assumption of identical phase space distributions in the two transverse planes the beam matching can be accomplished by means of two solenoids. This allows a very compact design minimising the impact of space charge effects. The length of the Linac4 Test Stand LEBT amounts to 1.8 m. Apart from the two solenoids the LEBT consists of two pairs of steerer magnets, one Beam Current Transformer (BCT) and a diagnostics box with Iris, Pre-chopper, Profile SEM-Grid and a Faraday cup. The steerer magnets are required to compensate alignment errors of source, solenoids and RFQ. The permanently installed diagnostics in between the solenoids are foreseen to control the operation of source and LEBT. In the commissioning phase a combination of emittance meter and Faraday cup was mounted at the LEBT exit, Fig. 2.12 - black box. Fig. 2.12 illustrates the LEBT layout.
The Faraday cup at the LEBT exit permits the measurement of the beam current transmitted to the RFQ location and the investigation of the beam transmission. The transmission through the RFQ is determined by the matching of

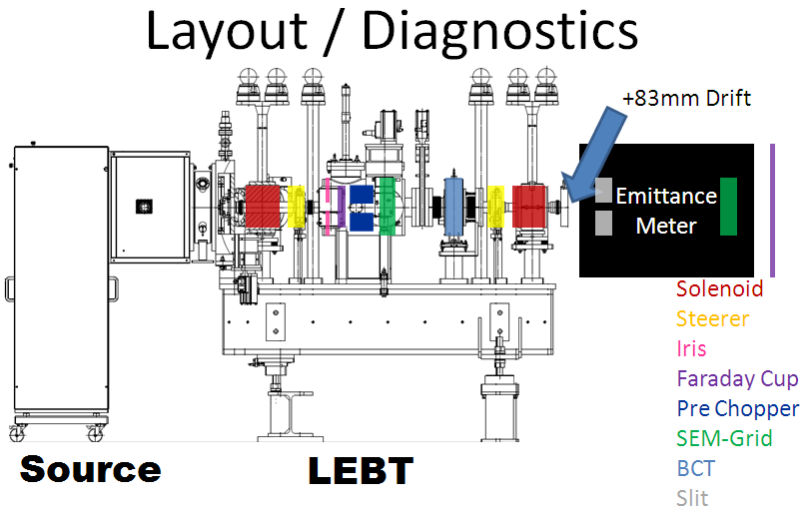

Figure 2.12: Schematic of the Linac4 Test Stand LEBT and Source
The positions of beam optics elements such as steerer magnets and the positions of diagnostics elements such as Faraday cups and SEM-Grids are highlighted. At the exit of the LEBT the sequence of the diagnostics devices of the emittance meter are illustrated. Between RFQ matching plane and measurement plane of the emittance meter a drift of $83\,mm$ *is present.*

the beam phase space. In order to enhance the RFQ matching detailed investigations of the phase space distribution at the LEBT exit for varying LEBT and source settings were conducted.

Beam Optics

In order to optimise the layout of the accelerator elements a model of the Linac4 source beam, so called reference beam, was developed. The LEBT beam optics of this reference beam is characterised by a low-loss beam transmission within a perfect matching to the RFQ. A space charge compensation of 90 % is assumed. Also no significant emittance increase is predicted based on the results of the simulation studies. The development of the transverse beam size and of the beam transmission along the Test Stand LEBT is shown in Fig. 2.13.
In order to simulate the LEBT beam dynamics of the measured proton beam several measured phase space distributions were combined to create an universally valid distribution as simulation input. Similar to the beam dynamics of the reference beam also for the simulated proton beam dynamics a space charge compensation was assumed. Based on source and LEBT measurements an effective space charge current of $I_{eff.} = 10\,mA$ was determined corresponding to a space charge compensation of 85 % to 90 %.
The measured proton beam distributions are characterised by significantly larger, transverse emittances, transverse beam sizes and beam divergences leading to a higher potential of particle losses along the LEBT. Due to the LEBT

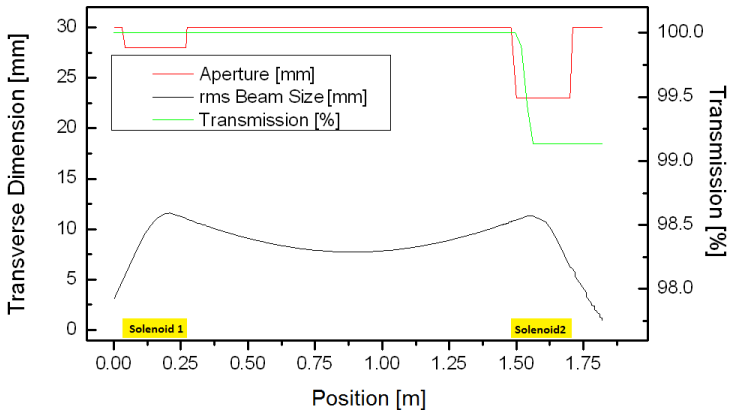

Figure 2.13: LEBT Beam Envelope - Reference Beam

This plot shows the development of the transverse beam size and the aperture constraints along the LEBT. Aperture bottlenecks are located at the solenoids, where large transverse beam sizes are present. Although at these locations minor particle losses are simulated, a good beam transmission within an excellent RFQ matching is expected.

layout the beam transmission is defined by the settings of the first solenoid. In Fig. 2.14 the simulated transmission in dependence of the solenoid1 current is plotted.

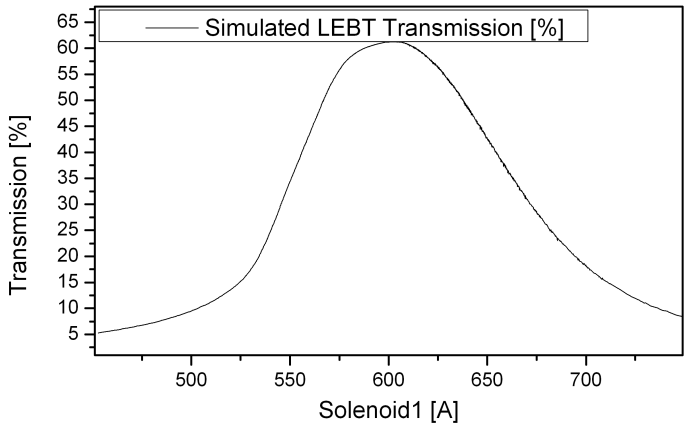

Figure 2.14: LEBT Transmission

In this figure the simulated LEBT transmission of the measured proton beam is plotted in dependence of the solenoid1 current. A maximum beam transmission of approximately 60 % *is expected at a solenoid1 current of* $I_{sol1} = 600\,A$.

A maximum transmission of approximately 60 % is predicted at a solenoid1 current of $600A$. Hence, assuming a proton beam current of $I^{in}_{proton} = 55\,mA$ at the source exit a maximum beam current of $I^{out}_{proton} = 33\,mA$ is expected. In Fig. 2.15 the locations of lost protons, H_2^+ ions and H_3^+ ions along the LEBT

are shown.

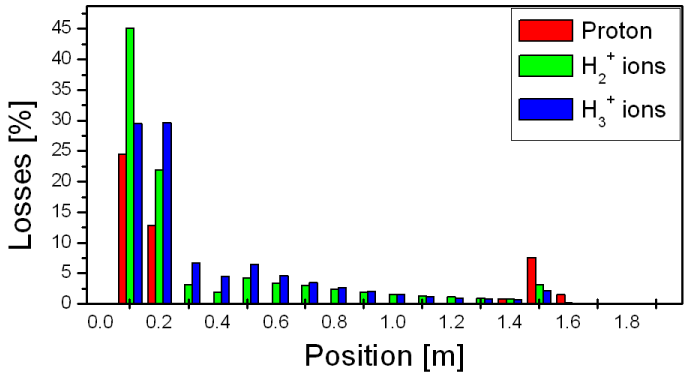

Figure 2.15: Particle Losses along the LEBT

In this diagram the percental particle loss of the initial particle distribution is plotted along the LEBT. Due to the large transverse beam size significant particle losses are expected already at the entrance of the first solenoid.

For this simulated "loss map" a LEBT setting with maximised proton beam transmission was chosen.
Due to the high particle losses a variation of the transverse emittance is expected, Fig. 2.16.

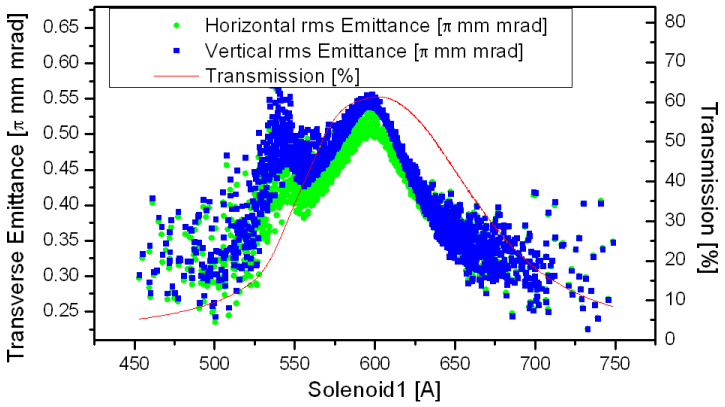

Figure 2.16: Transverse Emittance Variation

In this plot the simulated beam transmission and the final emittance at the LEBT exit are plotted. A reduction of the transverse emittance in dependence of the beam transmission is expected. As the simulation beam is characterised by a small variation of the transverse phase space distribution in horizontal and vertical plane, minor discrepancies between the final horizontal and vertical emittances are observed.

At the exit of the LEBT a reduction of the transverse emittance depending on the beam transmission is predicted.
The third important characteristic of the LEBT is its tunability or rather its

potential to match the beam to the RFQ. In order to quantify the RFQ matching the penalty function, also called mismatch function [36], is used. A perfect matched beam is indicated by a vanishing mismatch value. The grade of mismatch is indicated by the value of the mismatch function. For the invesitgation several thousand different combinations of solenoid1 and solenoid2 settings were simulated. The RFQ matching depends simultaneously on the settings of the two solenoids. Fig. 2.17 shows the simulated mismatch projected on the settings of the first solenoid, which defines the LEBT beam transmission.

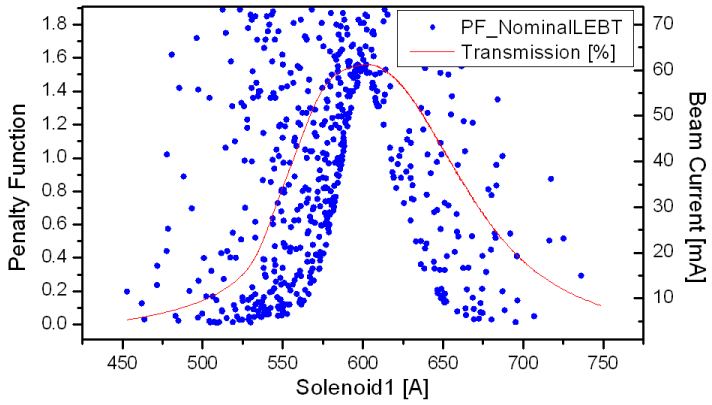

Figure 2.17: RFQ Matching

In order to quantify the RFQ matching the penalty function / mismatch function [36] is used. A mismatch value of zero indicates a perfect matching. This plot shows the feasible penalty function values for the LEBT parameter space projected on the solenoid1 setting. In addition to the penalty function the simulated beam transmission is plotted. Based on these data a suboptimal RFQ matching is predicted for LEBT settings with maximised beam transmission.

Based on these simulation results a suboptimal RFQ matching is predicted at LEBT configurations with maximised LEBT transmission.
In contrast to the reference beam optics high particle losses for the measured phase space distributions are simulated. In Fig. 2.18 the reference beam optics and the beam optics of the measured phase space distributions are shown. At the optics simulation of the measured beam a LEBT setting with maximised LEBT transmission was chosen. Significant particle losses upstream and along the first solenoid and minor particle losses downstream of the first solenoid are observed.

2.3 LEBT Commissioning - Phase I

In the first phase of the LEBT commissioning emittance measurements downstream of the first solenoid and spectrometer line measurements are conducted. The aim of this commissioning phase is the determination of the solenoid scaling factor, the estimation of the effective space charge and the identification of the particle species and their population ratio.

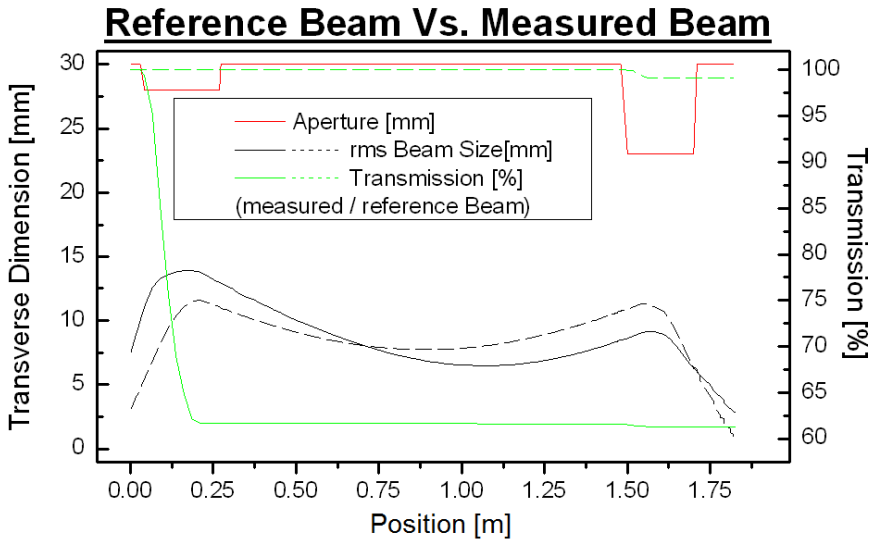

Figure 2.18: LEBT Beam Optics - Measured Beam

In this plot the LEBT beam optics of the reference beam and the measured beam are shown. In contrast to the reference beam dynamics high particle losses at the first solenoid are expected for the measured beam leading to a maximum LEBT transmission of approximately 60 %.

For the simulation of the LEBT beam dynamics the solenoid fields were analytical modelled and as field maps implemented in the beam optics simulations. These field maps calculated based on analytical formulas need to be benchmarked with measurement results.
Along the LEBT the interaction of the source beam with residual-gas molecules leads to the effect called space charge compensation. At this effect the first part of the beam pulse ionises parts of the residual-gas molecules. Due to the electrodynamics potential of the beam pulse the negative charged and positive charged components of the residual-gas will be separated. E.g. in the case of proton beams negative charged ions and electrons are captured inside the potential of the beam pulse, whereas the positive charged ions are expelled. The accumulation of opposite charged particles inside the beam pulse leads to a neutralisation effect of the space charge effects [37]. Based on emittance measurements at the source exit and downstream of the first solenoid an effective space charge current of $I_{eff.} = 10\,mA$ was determined [34], which corresponds to a space charge compensations of 85 % to 90 %.
Downstream of the first solenoid a temporary measurement lines for the determination of the particle energy and of the beam energy spread was installed. Based on these measurements it has been concluded that the extracted proton beam is characterised by an energy spread corresponding to the specified energy spread [34].
This measurement line was also used to identify the particle species and their population ratio at the source exit.

2.3.1 Emittance Measurements

The emittance measurements downstream of the first solenoid are used to benchmark the solenoid field maps, to investigate the space charge compensation and to cross-check the particle tracking code Path. For this purpose several emittance measurements with different solenoid1 settings were conducted. Downstream of the first solenoid the different particle species are separated in the transverse phase space. This allows the simultaneous test of the solenoid field maps and the examination of the space charge compensation.
For the simulation a test beam based on the measurement results of the source commissioning was generated. This test beam is composed of three beams of different particle species, namely protons, H_2^+ ions and H_3^+ ions[7]. The three beams are characterised by identical transverse phase space distributions.
In Fig. 2.19 simulated phase space distributions (monochrome) downstream of the first solenoid are plotted and superimposed with the corresponding emittance measurements (colour).
For sake of clarification the beam offsets of the measured phase space distributions were not corrected. For the simulation an effective space charge current of $I_{eff.} = 8\,mA$ was assumed. Investigations of the source performance led to a comparable effect space charge current of $I_{eff.} = 10\,mA$ [33]. For the generation of the solenoid field maps a solenoid current of $1000\,A$ was assumed. The comparison of the measured and simulated phase space distributions indicates a constant offset of $10\,A$ leading to a solenoid scaling factor of $\alpha_{sol1} = \frac{I[A]+10}{1000}$.
A good agreement between simulation results and measurement results for each of the particle species is obtained.

2.3.2 Spectrometer Measurements

At the emittance measurements downstream of the first solenoid a separation of the source beam into four beams according to their momentum was observed, Fig. 2.19. By using a spectrometer line composed of a bending magnet and a SEM-Grid an identification of the particle species and a measurement of their population ratio are conducted.

Identification of the Particle Species

At the emittance measurements with different solenoid1 settings a specific movement of three of the four distributions in the phase space was observed, Fig. 2.19. It can be concluded that the particles of the distribution, which are insensitive to the changes of the solenoid field, are uncharged. The other three distributions are influenced by the solenoid setting. It is assumed that these three particle species are charged with $q = +1e$. To identify the species a spectrometer line was used, Fig. 2.20.
The dispersive effect of the spectrometer dipole leads to a separation of the particles according to their momentum.

[7] Although a neutral particle beam is component of the measured beam, the generation of the neutral particle beam as part of the simulation beam was not conducted.

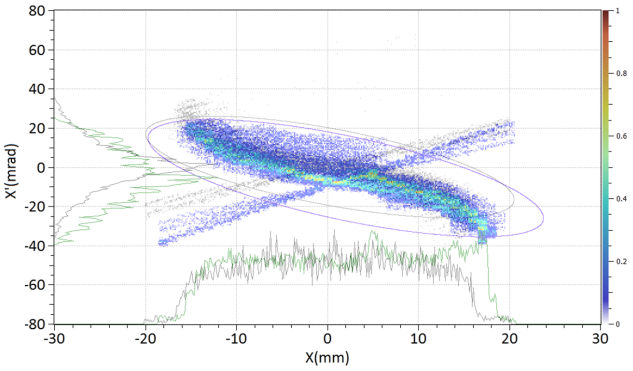

(1) 600A Solenoid Current

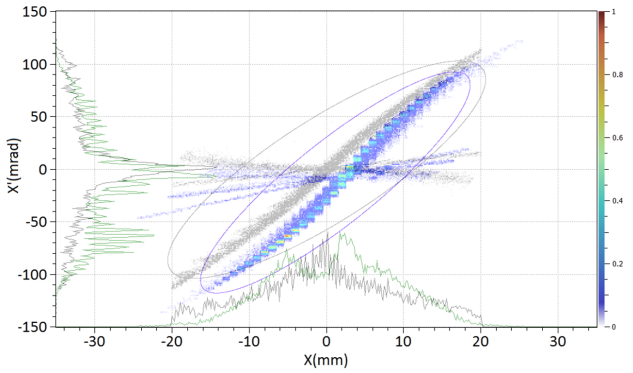

(2) 800A Solenoid Current

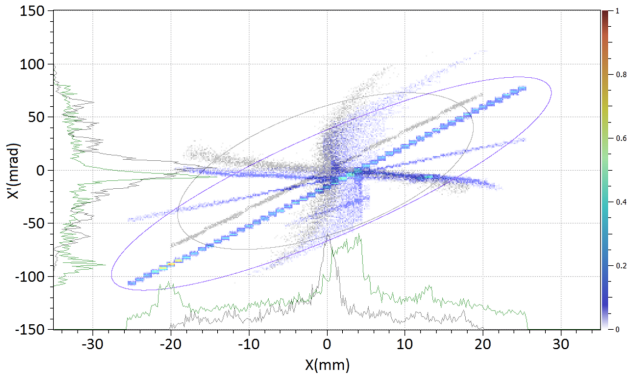

(3) 1000A Solenoid Current

Figure 2.19: Emittance Measurements downstream of Solenoid1

Downstream of the first solenoid the different particle species of the source beam are separated in the transverse phase space. Phase space measurements(colour) at different solenoid1 settings were conducted and compared with the corresponding simulated phase space distributions (monochrome). For sake of clarification the offsets of the measured beam were not corrected. A good agreement between simulation and measurement results is obtained.

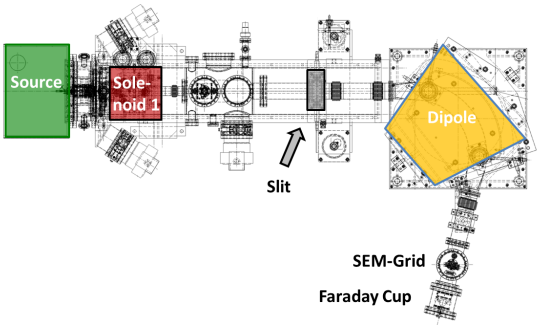

(1) Scheme of Spectrometer Measurement Line

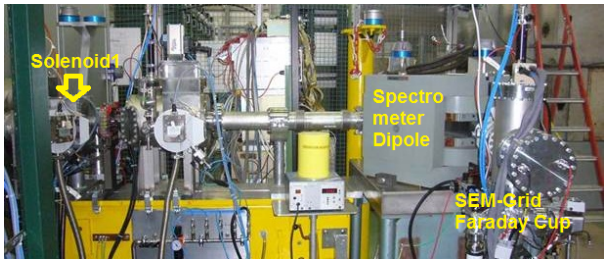

(2) Photo of Spectrometer Measurement Line

Figure 2.20: Layout of the Spectrometer Line

In figure (1) the layout of the spectrometer measurement is shown. Between the source (green) and the spectrometer magnet (yellow) the first solenoid (red) was mounted to optimise the beam optics for the measurements. Downstream of the spectrometer magnet a SEM-Grid and a Faraday Cup were mounted. For the examination of the energy spread the slit between solenoid1 and spectrometer dipole was used to collimate the transverse phase space. Figure (2) shows a photo of the measurement layout. Photo provided by [31].

The construction of the spectrometer dipole allows the variation of the magnetic field strength to deflect the different particle species to the downstream measurement devices SEM-Grid and Faraday cup.
The ratio between the current settings of the spectrometer magnet is $1 : \sqrt{2} : \sqrt{3}$. Assuming a linear scale between dipole field and magnet current the ratio of the magnetic field is characterised by the identical ratio. The kinetic energy T_i of the particles is defined by the extraction voltage $V_{ext.}$. At the source exit the kinetic energy is in the order of a few tens of keV and so the particles are not relativistic. Therefore, the particle momentum can be calculated using:

$$T_i = q_i \cdot V_{ext.} = \frac{p_i^2}{2m_i}. \tag{2.2}$$

The effect of a magnetic field on a moving charged particle is defined by the

Lorentz force, Eq. 1.2,

$$\vec{F_i} \quad = \quad q_i \cdot \left(\vec{E} + \vec{v_i} \times \vec{B} \right).$$

Assuming that the spectrometer dipole can be described by an ideal dipole field perpendicular to the particle momentum without electrical field components, the particles are forced on a circular path with a radius ϱ. This path is defined by:

$$\frac{p}{q} = B\varrho\,. \tag{2.3}$$

As the measurement position is maintained, the bending radius ϱ of each of the particle species has to be identical. Using Eq. 2.3 the relative change of the magnetic flux density identifies the momentum deviation[8]:

$$p_1 : p_2 : p_3 \quad = \quad 1 : \sqrt{2} : \sqrt{3}.$$

The species masses are obtained from the ratio of the momentums using Eq. 2.2:

$$m_1 : m_2 : m_3 \quad = \quad 1 : 2 : 3.$$

This ratio is perfectly confirmed by protons, H_2^+ ions and H_3^+ ions. The measurement data of this spectrometer line investigation is listed in Tab. 2.5.

$I_{solenoid1}[A]$	$I_{magnet}[A]$	Signal $[mA]$
606	14.35	-20.9
832	20.2	-2.0
1064	25.1	-2.0

Table 2.5: Data of the Spectrometer Measurement
During variation of the spectrometer magnet current I_{magnet} three signal peaks at the Faraday cup were detected. The solenoid1 focusing was adapted to maximise the signal strength. In this table a summary of the measurement settings and the measurement results is presented.

Determination of the Population Ratio

Due to the properties of the source beam significant particle losses upstream and along the first solenoid are predicted. To identify the population ratio of the species the LEBT beam optics needs to be considered. As also the focusing effect of the solenoid scales with the particle momentum, an adjustment of the solenoid field is required to obtain comparable particle losses for each particle type. After the setup of the spectrometer magnet to a certain particle type, the solenoid current was adjusted to obtain the maximum signal in the spectrometer

[8] Assuming that all particles are single charged, i.e. $q = +1e$.

line. The applied solenoid1 current also demonstrating the ratio of:

$$I^1_{sol1} : I^2_{sol1} : I^3_{sol1} \quad = \quad 1 : \sqrt{2} : \sqrt{3}.$$

The measurement results are reported in Tab. 2.5. Based on the signal strength a population ratio of $21\,(protons) : 2\,(H_2^+\,ions) : 2\,(H_3^+\,ions)$ was detected. Based on these measurement results it can be concluded that approximately 84% of the extracted charged particles at the source exit are protons.

2.4 LEBT Commissioning - Phase II

At the second phase of the LEBT commissioning the Test Stand LEBT was completely assembled. The aims of the commissioning phase are the preparation of the RFQ commissioning and the reconstruction of the LEBT beam dynamics, both conducted in the framework of this thesis.
The reconstruction of the beam dynamics was mainly based on the measurement results of the source commissioning of 2011 and the measurements of the LEBT commissioning phase II. Based on the reconstructed beam dynamics the "theoretical LEBT acceptance" has been determined. In addition to the "theoretical LEBT acceptance" a "semi-experimental[9]" and an "empirical LEBT acceptance[10]" were identified.
For the preservation of transverse beam emittance and the minimisation of particle losses along the RFQ the matching of the Twiss parameters at RFQ injection is crucial. Hence, for the preparation of the RFQ commissioning the identification of LEBT settings with optimised RFQ matching is essential. In addition to the theoretical study of the RFQ matching at different LEBT settings an empirical RFQ matching was conducted. The identified settings are characterised by different transmissions allowing a variation of the RFQ input beam current.
For the preparation of the RFQ commissioning additional measurements for the compensation of feasible alignment errors were included. It is foreseen to compensate longitudinal alignment errors by the adjustment of the focusing of the second solenoid. In preparation of feasible transverse alignment errors steerer maps were generated. At these steerer maps the average position of the phase space distribution, the transverse emittances and Twiss parameters are recorded in dependence of the steerer settings. Based on these maps the determination of transverse alignment errors is possible, which allows the physical adjustment of the accelerator elements.
During this commissioning phase an iris was installed at the diagnostics chamber of the LEBT. The collimating impact of the iris is used to generate probe beams characterised by lower transverse emittances and lower beam currents.

[9] For the determination of the semi-experimental acceptance a combination of phase space measurements and particle tracking simulations is used.

[10] For the determination of the empirical LEBT acceptance the detailed beam characterisation of the source commissioning of 2011 and the beam current measurements at the LEBT exit have been used. Based on these measurement results an acceptance region in the transverse phase space has been determined.

It is foreseen to use these probe beams for the empirical determination of the Linac4 acceptance. The tunability of the probe beam current and emittance were studied for the LEBT parameter space. The transverse emittance preservation of these probe beams along the RFQ can be controlled by the Twiss parameter matching. This allows the generation of probe beams with lower beam currents and nominal transverse emittance downstream of the RFQ.

2.4.1 Beam Current Measurements

Along the LEBT, beam current measurements were performed at three different locations, which are Faraday cup1 (purple) and Beam Current Transformer (BCT) (blue) in between the two solenoids and Faraday cup2 at the LEBT exit, Fig. 2.21.

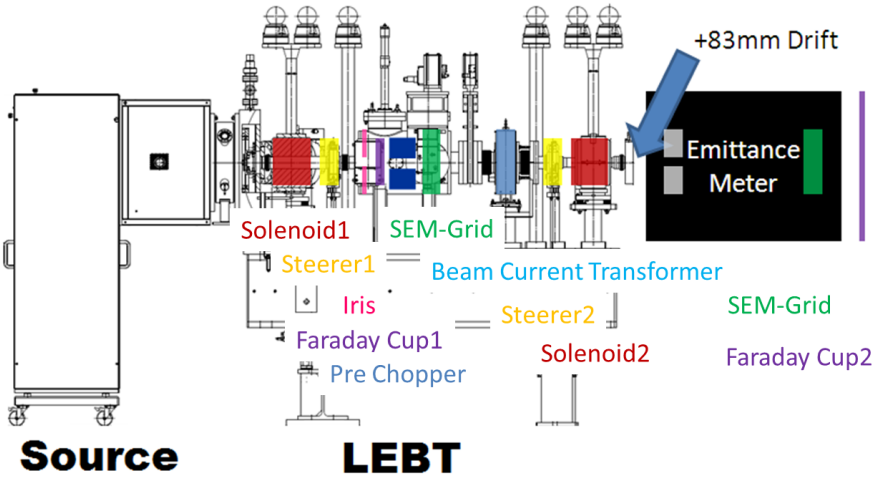

Figure 2.21: LEBT Layout

This figure shows a schematic of the LEBT. The position of the beam optics elements and diagnostics devices such as solenoid magnets (red) and SEM-Grids (green) are highlighted. In the case of several elements of similar type a consecutive number is added, e.g. Solenoid1 (at the source exit) and Solenoid2 (at the LEBT exit).

As the two Faraday cups are equipped with similar electronics, the same trigger system for read out and sampling of the beam signal can be used. Hence, a constant time slot of the beam pulse can be isolated at the two Faraday cups, which was used to measure the LEBT beam transmission.
The two solenoids are located at both ends of the LEBT. Hence, the beam transmission is mainly determined by the settings of the first solenoid. In Fig. 2.22 the signals of the two Faraday cups in dependence of the solenoid1 current are plotted.

The Faraday cup1 signal curve is characterised by a increasing slope at lower currents of the first solenoid, a wide plateau from $I_{sol1} = 700\,A$ to $I_{sol1} = 800\,A$

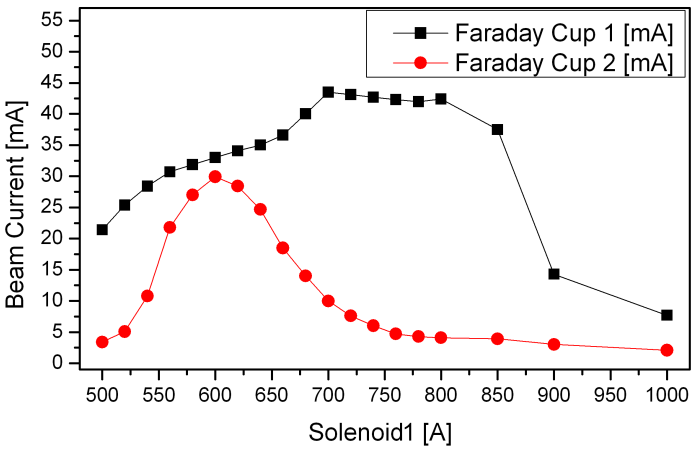

Figure 2.22: Faraday Cup Measurements

In this plot the signals of Faraday cup1 (LEBT centre) and Faraday cup2 (LEBT exit) are plotted in dependence of the settings of the first solenoid. A maximum Faraday cup2 signal corresponding to a maximum LEBT transmission is obtained at a solenoid1 current of $I_{sol1} = 580\,A$.

and a decreasing slope at higher solenoid currents. The maximum Faraday cup signal is $43.5\,mA$.
For the beam current measurement at Faraday cup2 the second solenoid was set to a solenoid current of $I_{sol2} = 300\,A$ to ensure that the beam is focused into the Faraday cup. Based on the measurement results of Faraday cup2 a maximum LEBT beam transmission is obtained at a solenoid1 current of $I_{sol1} = 580\,A$ leading to a beam current of approximately $30\,mA$.
The power input of the source was $50\,kW$ at a minimised hydrogen flux. At these settings a source beam current of $85\,mA$ to $95\,mA$ is expected.
For the comparison of the measurement results with simulated Faraday cup signals a simulation beam based on the measurements at the source exit with an RF-power of $50\,kW$ was generated. This generated beam also consists of the three charged particle species, protons, H_2^+ ions and H_3^+ ions.
In Fig. 2.23 a comparison of the measured Faraday cup signals with simulated Faraday cup signals is shown.
A good agreement between simulation results and measurement results for Faraday cup2 is obtained. The maximum beam transmission of about 35 % of the source beam agrees perfectly with the measured beam current of approximately $30\,mA$ assuming a source beam current of $85\,mA$, which was measured at the source exit.
In the case of a pure proton beam a maximum LEBT transmission of 60 % was predicted, section 2.2.2. The measured source beam current of $85\,mA$ indicates a proton beam current of approximately $60\,mA$ at the source exit leading to a proton beam current of $36\,mA$ at the LEBT exit.
For Farady cup1 the results of the measurements and of the simulations differ.

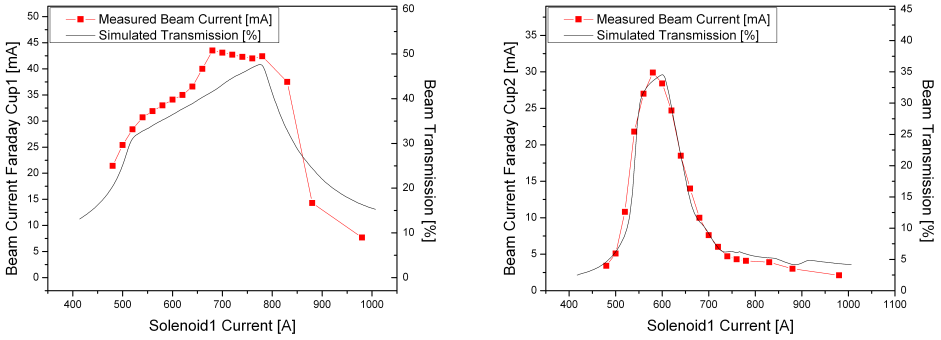

(1) Faraday Cup1 Signal

(2) Faraday Cup2 Signal

Figure 2.23: Faraday Cup Currents - Measurement and Simulation
In these plot the measured Faraday cup currents and the corresponding simulated beam transmission are shown. At the used source settings a source beam current of approximately $85\,mA$ *was measured. A good agreement between the LEBT transmission and the measurement results of Faraday cup2 is obtained. In the case of the Faraday cup1 measurements significant differences between measurement and simulations are noticeable.*

It was concluded that most likely the measurement results of Faraday cup1 are incorrect. This assumption is based on the fact that the Faraday cup signal showed a beam transmission above the simulated transmission at solenoid1 currents below $I_{sol1} = 640\,A$. This might be caused by a wrong setting of the Guard Ring voltage. During the beam current measurements at the source exit a malfunction of the Faraday cup was observed at higher RF-power levels. It was concluded that this misreading was caused by unwanted interaction of the source beam with the Guard ring material. At the LEBT commissioning a significant discrepancy between the magnetic axis of solenoid1 and the beam propagation axis was detected. As a consequence a transverse movement of the beam centre in dependence of the solenoid settings was caused. It is likely that the interaction of the beam with the Faraday cup material caused an additional discharge of the Guard ring leading to an enhanced Faraday cup signal. This effect might have been amplified by the transverse beam offset[11].
In Tab. 2.6 Faraday cup2 signals are summarised, which were measured with varying source settings. The listed LEBT settings were determined using emittance measurements reported in the next part of this section.
The maximum beam current at Faraday cup2 was measured at solenoid1 currents between $I_{sol1} = 580\,A$ and $I_{sol1} = 600\,A$ for varying source configurations. A maximum beam current of $30\,mA$ to $32\,mA$ was measured perfectly confirmed by the LEBT beam dynamics simulations in combination with the measured beam parameters at the source exit.
At the source exit a high transverse emittance was detected. The transverse emittance and the beam current are correlated and both parameters are in-

[11] Further studies of the measurement setup could not be conducted.

RF-Power **LEBT-Setting**	**20kW**	**30kW**	**40kW**	**50kW**	**60kW**
560-330-1000	15.1	23.2	27.5	29.1	29.9
580-330-1000	17.5	26.6	30.4	31.1	32.1
580-340-1000	17.6	26.6	30.3	31.1	32.1
600-330-1000	17.9	27.9	30.3	29.5	30.6
600-340-1000	17.9	28.0	30.4	29.6	30.5
600-350-1000	18.0	28.0	30.5	29.6	30.6
620-340-1000	17.1	25.5	26.7	25.1	25.5
620-350-1000	17.0	25.6	26.6	25.1	25.2
620-360-1000	17.1	25.5	26.5	24.5	24.6
665-355-1-*0.25*00	10.8	13.6	13.8	12.8	12.6
665-365-1-*0.25*00	10.2	12.7	12.7	11.7	11.5
665-375-1-*0.25*00	9.3	11.4	11.6	10.7	10.5
680-355-1-*0.25*00	8.4	10.4	10.4	10.0	10.0

Table 2.6: Beam Current Measurement at the LEBT Exit
In this table the measured beam currents [in mA] using Faraday cup2 are summarised. The beam current were recorded in dependence of the LEBT setting and the source RF-power. In order to indicate the LEBT setting a special nomenclature is used. E.g. the nomenclature 665-365-1-0.2500 identifies a solenoid1 current of $I_{sol1} = 665\,A$*, solenoid2 current of* $I_{sol2} = 365\,A$*, horizontal steerer1* $1\,A$ *and vertical steerer1* $-0.25\,A$*. A maximum beam current of* $30\,mA$ *to* $32\,mA$ *was measured.*

creasing with increasing source RF-power. Due to the significantly reducted beam current at the LEBT exit it is expected that the beam emittance exceeds the LEBT acceptance. The results of the beam current measurements at the source exit and LEBT exit indicate that the beam emittance exceeds the LEBT acceptance at a RF-power setting of approximately $30\,kW$. A detailed discussion is presented in section, 2.4.3.

2.4.2 Emittance Measurements

Based on the theoretical performance studies of the LEBT LEBT settings for the RFQ injection were defined, see chapter 2.2.2. The simulated phase space distributions are benchmarked with the corresponding emittance measurements. Based on the measured phase space distributions the expected RFQ performance is investigated.

Emittance Measurements

Due to the high transverse beam emittance at the source exit major particle losses along the LEBT were caused, predicted and measured. Based on the theoretical studies a suboptimal RFQ matching is predicted at LEBT settings characterised by maximised LEBT beam transmission, Fig. 2.24.
In the solenoid1 current range from $I_{sol1} = 560\,A$ to $I_{sol1} = 680\,A$ emittance measurements with varying solenoid2 settings were conducted. A comparison of the simulated phase space distributions with the emittance measurements is presented in Fig. 2.25.
As the beam dynamics is optimised for the transmission of the proton beam

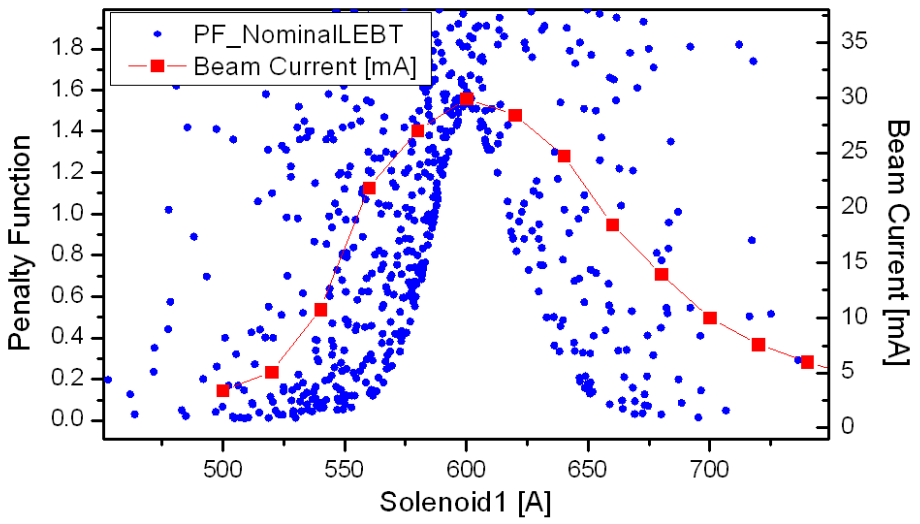

Figure 2.24: Beam Current and RFQ Matching
In this figure the beam current at the LEBT exit is plotted with the expected RFQ matching potential quantified by the penalty / mismatch function [36]. At LEBT settings with maximised beam transmission a suboptimal RFQ matching is expected.

fraction of the source beam vanishing transmissions for the H_2^+ ion and H_3^+ ion beams are determined. Due to the enhanced proton signal the detection of the H_2^+ ion distribution and H_3^+ ion distribution is hindered.
However, by means of the steerer magnets the proton intensity could be reduced allowing the measurement of the H_2^+ ion and H_3^+ ion distributions, Fig. 2.26.
A perfect agreement between the simulated and measured phase space distributions has been obtained.

Since the beam optics along the RFQ are highly influenced by space charge effects, it is needed to adapt the matching Twiss parameters to the beam characteristics transverse emittance and beam current, Tab. A.1. Based on the measured phase space distributions at the LEBT exit LEBT settings for the RFQ commissioning were defined, listed in Tab. A.2.
In the case of a longitudinal misalignment of the RFQ an adjustment of the beam focusing is required. Therefore, additional emittance measurements in the close parameter space of solenoid2 were conducted.
At these measurements a source RF-power of $50\,kW$ was used corresponding to a transverse beam emittance of $\varepsilon = 0.66\,\pi\,mm\,mrad$ at the source exit. At the LEBT exit transverse emittances below $\varepsilon = 0.4\,\pi\,mm\,mrad$ were measured. This emittance reduction caused by particle losses along the LEBT depends on the LEBT transmission or rather the settings of solenoid1, Fig. 2.16. This dependency is partly confirmed by the measurement results.
A major difference between simulation results and measurement results is the limit of the transverse emittance values. At LEBT settings with maximum beam

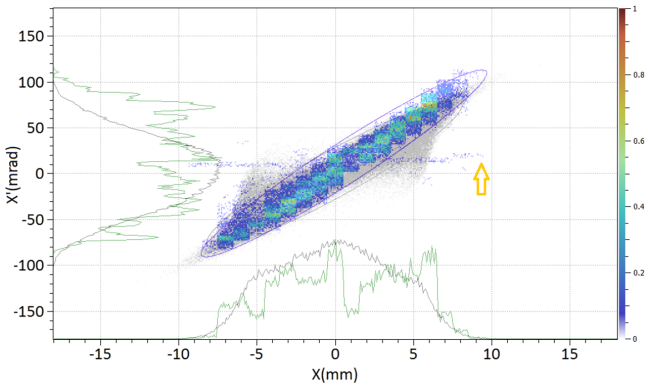

(1) 560A - 330A

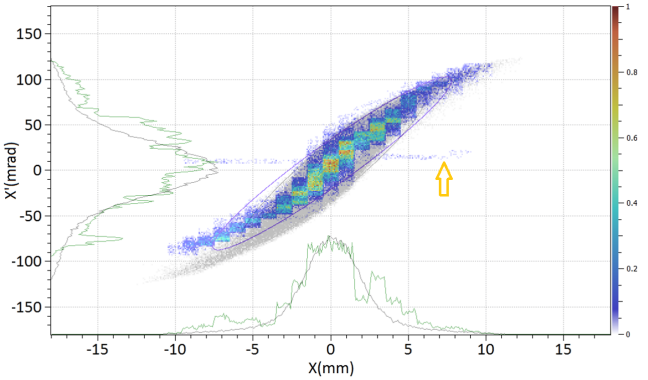

(2) 620A - 360A

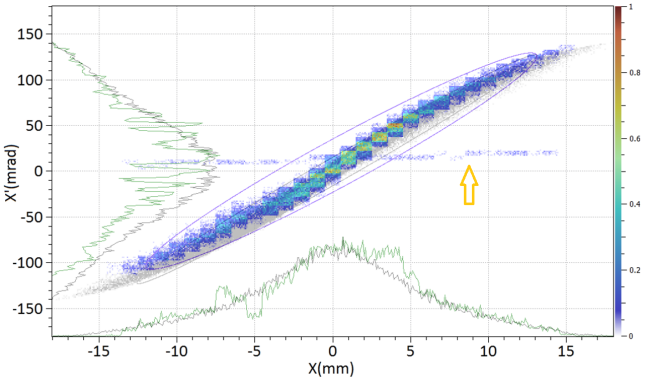

(3) 665A - 375A

Figure 2.25: Emittance Measurements and Emittance Simulations
In this figure three emittance measurements (colour) and their corresponding simulations results (monochrome) are shown. At the measurements a horizontal signal line is noticeable (marked). As the position of this line is maintained at varying LEBT settings, it was concluded that this signal was generated by neutral particles. A good agreement between simulation and measurement is accomplished.

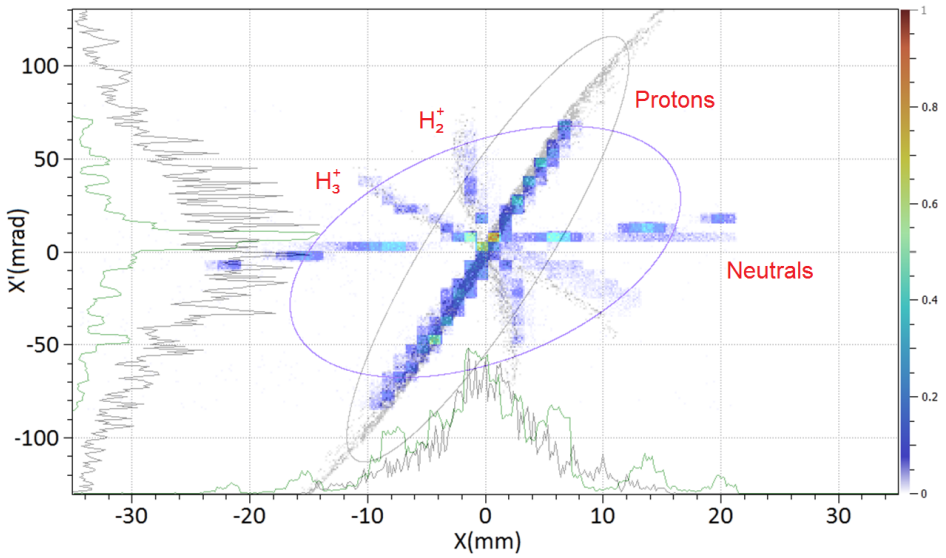

Figure 2.26: Emittance Scan with reduced Proton Beam Intensity
In this plot a specially measured phase space distribution (colour) is shown together with the corresponding LEBT simulation (monochrome). At this special measurement the proton beam intensity was significantly reduced by intended mis-steering leading to a scraping of the proton beam distribution. Due to this beam scraping the distribution tails of the proton beam were cut. A perfect agreement between simulation and measurement is obtained.

transmission a theoretical emittance of $\varepsilon = 0.5\,\pi\,mm\,mrad$ is predicted. The measured emittances are in the order of $\varepsilon = 0.4\,\pi\,mm\,mrad$. Possible sources of this difference are the precision of the emittance measurements and additional particle losses, which might be caused by the alignment errors.

RFQ Simulation

The beam matching to the RFQ determines the beam transmission through the RFQ and the transverse emittance growth. Based on the theoretical studies of the Test Stand LEBT a superior beam matching is expected at LEBT settings with a reduced LEBT beam transmission. In order to estimate the beam characteristics at the exit of the RFQ test beams based on the measured beam characteristics were generated and tracked through the RFQ[12][38]. Based on the RFQ transmission and the final emittance values optimised LEBT settings were identified. The results of the RFQ simulations are reported in Tab. A.3. Based on the RFQ simulation results several characteristics are predicted. A good RFQ transmission can be achieved by the adjustment of the solenoid2 focusing. At settings with maximised LEBT transmission suboptimal RFQ transmissions of approximately 80% are simulated. The maximum beam current at the RFQ exit is in the order of $23\,mA$ to $24\,mA$ predicted for settings with

[12]Thanks to P.A. Posocco for performing the RFQ simulations.

maximised LEBT beam transmission leading to higher transverse emittances at the RFQ exit. Based on these simulation results it can be concluded that the performance of the Test Stand accelerator is limited by the LEBT performance.

2.4.3 LEBT Acceptance

The acceptance is defined as the maximum phase space volume with 100 % particle transmission. It depends on the lattice optics and it simultaneously depends on the beam parameters, which define the impact of collective effects such as space charge effects and wake fields.

Theoretical LEBT Acceptance

In order to determine the theoretical acceptance of the Test Stand LEBT space charge effects were neglected in a first order approximation. This approximation is verified by the space charge compensation and the dimensions of the LEBT, which limit the impact of space charge on the LEBT acceptance.
Since the LEBT acceptance depends on the settings of the solenoids, a setting with maximised beam transmission is chosen. A test distribution, which covers the acceptance, was generated, Fig. 2.27(1), and tracked through the LEBT. The theoretical acceptance is defined as the initial phase space distribution of the transmitted particles, Fig. 2.27(2).

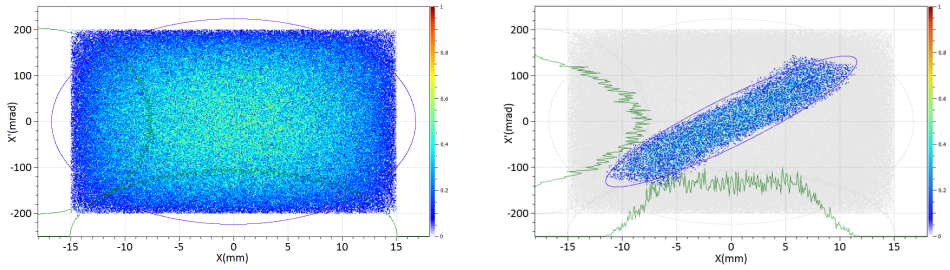

(1) Test Distribution (2) Theoretical Acceptance

Figure 2.27: Theoretical Acceptance
In order to identify the theoretical acceptance of the Test Stand LEBT a Test distribution (1) was generated, which covers the acceptance. This particle distribution was tracked through the LEBT. The initial coordinates of the transmitted particles define the LEBT acceptance (2) of the used LEBT settings. For (2) a LEBT setting was chosen characterised by the maximum measured beam transmission.

The implementation of space charge effect in this approach is rather complex. Also in the linear space charge model introduced in section 1.2 the impact of space charge is determined by the spatial distribution of the charged particles, at which the LEBT acceptance will be individually defined for each distribution. It is expected that due to space charge effects particles, which are beyond the acceptance, are influencing the final dimensions of the acceptance.

Semi-Experimental Acceptance

At the semi-experimental determination of the LEBT acceptance phase space measurements in combination with LEBT simulations are used.
For the reconstruction of the LEBT beam dynamics and for the preparation of the RFQ commissioning emittance measurements at the exit of the LEBT were conducted. The particles detected at the exit of the LEBT must have been inside the LEBT acceptance. Due to the high particle losses along the LEBT it can be concluded that the initial particle distribution at the source exit is exceeded beyond the acceptance. Therefore, the measured phase space distributions at the LEBT exit can be used to determine the overlap of acceptance and source beam distribution.
Based on the emittance measurement at the LEBT exit simulation beams were generated and 'back-tracked' to the source exit. The semi-experimental acceptance is determined by the simulated phase space distribution at the exit of the source. Fig. 2.28(1) shows a back-tracked phase space distribution representing the semi-experimental acceptance.

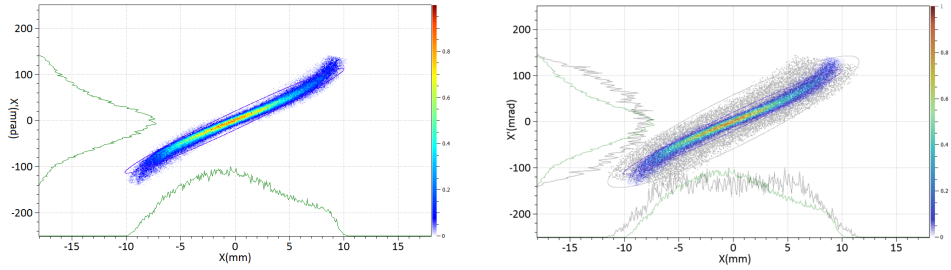

(1) Semi-Experimental Acceptance (2) Acceptance Comparison

Figure 2.28: Semi-Experimental Acceptance

The determination of the semi-experimental acceptance is based on the fact that each particle distribution, which was measured at the LEBT exit, has to be in the LEBT acceptance, as particles outside the LEBT acceptance were lost. Phase space distributions recorded at the LEBT exit have been tracked back to the source exit. The resulting phase space distribution at the source exit defines the semi-experimental acceptance, Fig. (1). As the semi-experimental acceptance is limited to the phase space area of the source beam, it will be included in the theoretical acceptance but not necessary vice versa. A comparison of both acceptances shows a good agreement, Fig. (2).

There are two major performance bottlenecks of this approach. The first bottleneck is that for the simulation of the solenoid focusing non-linear field distributions are required. At the used back-tracking routine the focusing impact of these non-linear field distributions was not perfectly inverted leading to a different focus of the distribution tails. Hence, discrepancies at the distribution tails were generated.
The second performance bottleneck is based on the space charge effect. The space charge effects are described by highly non-linear field distributions. At the back-tracking routine the defocusing impact of space charge effects needs

to be inverted into a focusing effect, which is not supported by the simulation codes. Therefore, space charge effects were neglected at the back-tracking procedure, at which the acceptance is overestimated.
A good agreement between theoretical acceptance and semi-experimental acceptance is obtained, Fig. 2.28(2).
As the semi-experimental acceptance is limited to the phase space distribution of the source beam, its area is included in the theoretical acceptance but not vice versa.

Empirical Acceptance

The empirical acceptance determination is based on source and LEBT measurements. Conditions of this approach are detailed investigations of the source beam emittance at varying source settings and detailed beam current measurements at the LEBT exit.
By means of variation of the source settings a defined variation of the source beam emittance can be conducted. As illustrated in section 2.1.2 an increase of the source RF-power leads to an increase of the beam emittance. By the increase of the beam emittance above the acceptance an enhancement of particle losses is caused leading to a decoupling of source RF-power and the beam current at the LEBT exit. At LEBT settings with maximised beam transmission the decoupling process starts at a source RF-power of $30\,kW$ to $40\,kW$, Tab. 2.6. Consequently, the empirical acceptance is defined by the phase space distribution at the source exit at the source RF-power of $30\,kW$. The distribution tails of the source beam have to be excluded, Fig. 2.29(1).
The empirical acceptance perfectly matches into the theoretical acceptance, Fig. 2.29(2), and a good agreement between empirical acceptance and semi-experimental acceptance is obtained, Fig. 2.29(3).

At the LEBT commissioning the source was operated at a nominal RF-power of $50\,kW$ with lowest stable hydrogen flux. Based on these parameters an updated reference simulation beam was generated. In Fig. 2.30 the phase space distribution of this source beam is plotted with the three determined acceptances.
At each determined acceptance a similar phase space region of the source beam is superimposed. The selected phase space area is characterised by an emittance of $\varepsilon = 0.3\,\pi\,mm\,mrad$ to $\varepsilon = 0.4\,\pi\,mm\,mrad$, which matched with the measured emittance values at the LEBT exit. As space charge effects and alignment errors were neglected at the determination of the acceptance, it is expected that the LEBT acceptance is over-estimated. At further studies the acceptances were used to remove particles from the source beam distribution, which are beyond the acceptance. The resulting phase space populations are comparable with the simulated LEBT transmissions. A minor overestimation of the LEBT acceptance was verified. A maximum overestimation of the LEBT transmission is in the order of 10%.
Although the acceptance is marginally overestimated, the results of the acceptance studies are in good agreement with the results of the theoretical and experimental investigations.

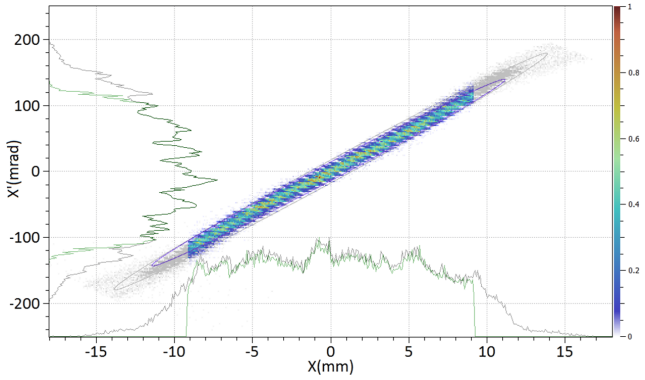

(1) Empirical Acceptance

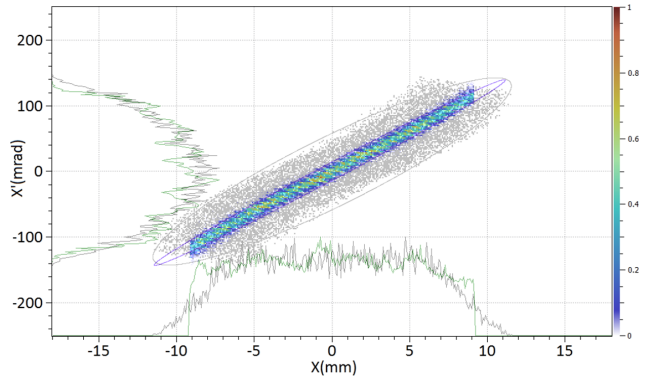

(2) Empirical Acceptance Vs. Theoretical Acceptance

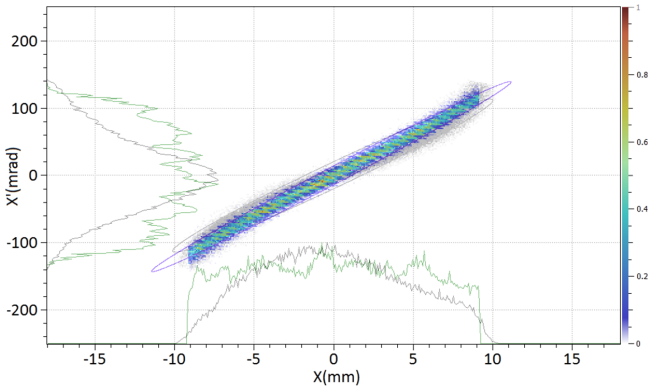

(3) Empirical Acceptance Vs. Semi-Experimental Acceptance

Figure 2.29: Empirical Acceptance

In (1) the empirical acceptance (colour) is shown. Its phase space area is defined by the beam phase space area of the source beam generated with a source RF-power of 30 kW (monochrome) excluding the distribution tails. The comparison of the empirical acceptance (colour) with the theoretical acceptance (2) and the semi-experimental acceptance (3) shows a good agreement of the three acceptances.

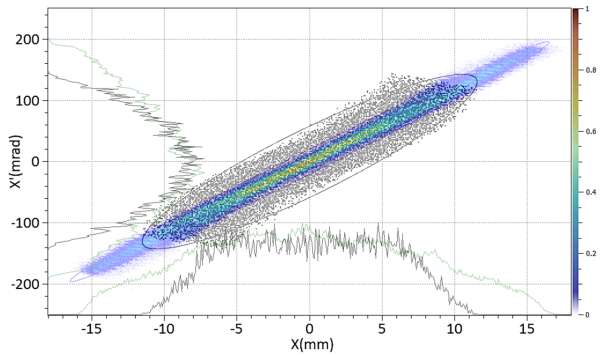

(1) Theoretical Acceptance

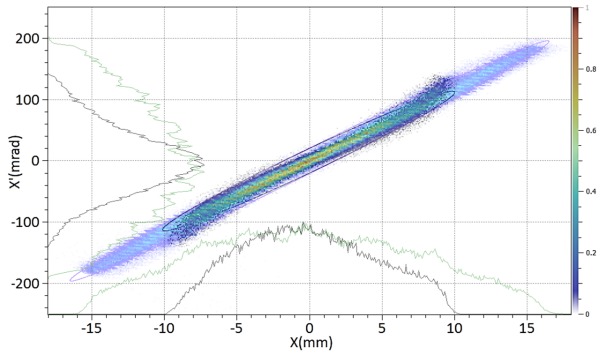

(2) Semi-Experimental Acceptance

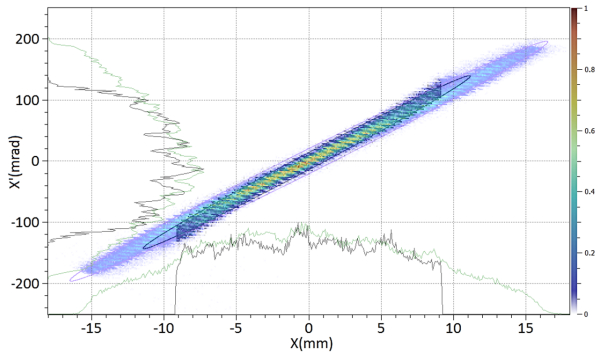

(3) Empirical Acceptance

Figure 2.30: Acceptance and Source Beam

In these three plots the theoretical acceptance(1), the semi-experimental acceptance(2) and the empirical acceptance(3) are plotted together with a representative source beam distribution(colour). At each acceptance an identical fraction of the source beam distribution is covered. This beam fraction has been isolated. The ratio between the population of the isolated beam fraction and the source beam is comparable to the measured LEBT transmission.

2.4.4 Pencil Beams

In addition to the nominal beam the generation of pencil beams is foreseen in the Linac4 commissioning and operation plan. These beams are characterised by reduced beam currents and lower transverse beam emittances. Due to these parameters the pencil beams are ideal probes for amongst others the beam based investigation of misalignments and aperture limitations. The generation of the pencil beams is achieved by means of an aperture limitation, namely two irises installed in between the two LEBT solenoids. The choice of an aperture limitation of $r = 5\,mm$ or $r = 11\,mm$ in combination with the adjustment of the first solenoid focusing allows a sensitive selection of the pencil beam current and of the pencil beam emittance.

Pencil Beam Current

For the adjustment of the beam current and beam emittance of the pencil beams two aperture limitations are crucial. One aperture restriction of the LEBT is the solenoid2 aperture. An enhanced beam focusing by means of the first solenoid leads to an over-focusing of the beam causing particle losses upstream and along the solenoid2. The second aperture bottleneck is defined by the iris aperture. The collimating impact of the iris has been studied using the first Faraday cup mounted directly downstream of the iris. In Fig. 2.31 the results of the beam current measurement for the two irises are plotted.

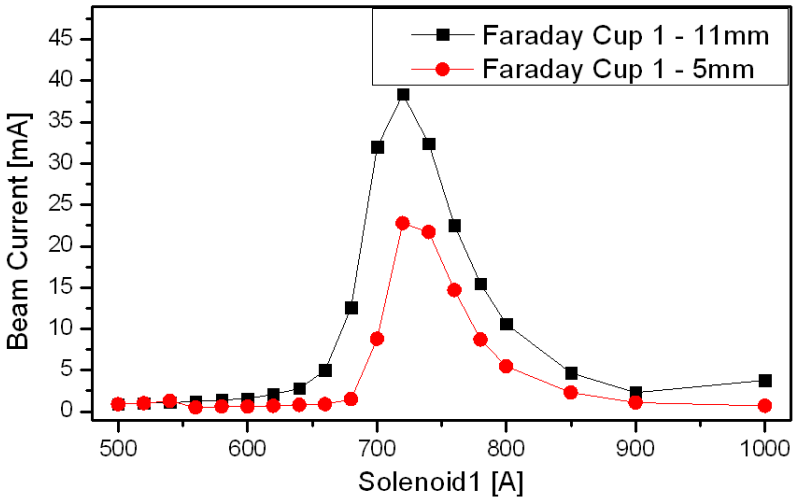

Figure 2.31: Pencil Beam Currents at Faraday Cup1

In this diagram the pencil beam current measurements at Faraday Cup1 are plotted in dependence of the settings of solenoid 1 for both irises. The peak beam currents are simultaneously obtained at a solenoid1 current of $I_{sol1} = 720\,A$. In the case of the $11\,mm$ iris a peak beam current of $38\,mA$ was detected. A significant reduction of the peak beam current to $23\,mA$ was measured for the pencil beam using the $5\,mm$ iris.

With increasing solenoid1 focusing the beam waist is moved upstream. At the signal maximum a maximised beam transmission is obtained, which means that the sum of the particle losses upstream of the first solenoid and at the iris are minimised. The maximum signal was measured at solenoid1 currents of $I_{sol1} = 720\,A$ to $I_{sol1} = 740\,A$ for each of the two irises. At this configuration a nominal beam current of approximately $40\,mA$ is expected. The pencil beam current using the $5\,mm$ iris in this LEBT setting is significant lower verifying particle losses at the iris.
It is expected that a further increase of the first solenoid focusing leads to an increase of the nominal beam current at Faraday Cup1. However, at a solenoid1 current of $I_{sol1} = 720\,A$ simultaneously the maximum beam current of the pencil beam with $5\,mm$ iris and $11\,mm$ iris is obtained. It is concluded that at these LEBT settings the beam is focused into the iris.
In Fig. 2.32 the results of the beam current measurements using Faraday cup2 are plotted.

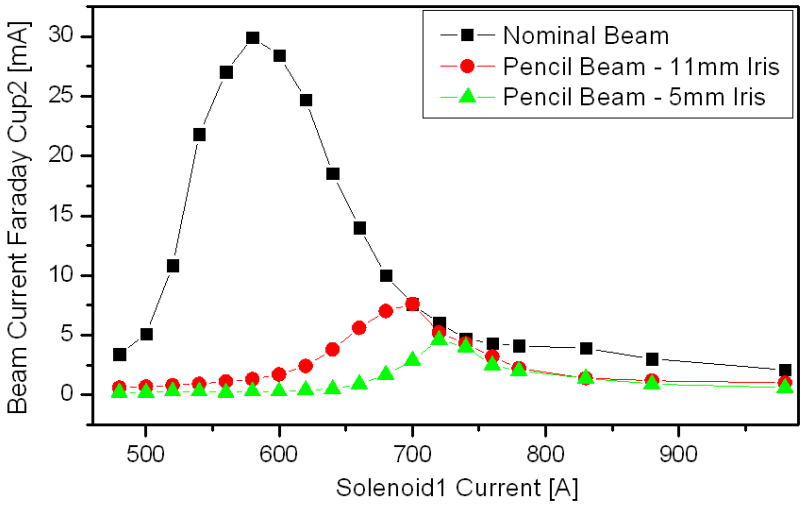

Figure 2.32: Pencil Beam Currents at Faraday Cup2
This plot shows the beam currents measured at the exit of the LEBT of the nominal beam and the pencil beams projected on the solenoid1 settings. The peak beam currents of the pencil beams are $7.6\,mA$ ($11\,mm$ iris) and $4.6\,mA$ ($5\,mm$ iris). At the LEBT settings, where a maximum pencil beam current was measured, values of the pencil beam current and the nominal beam current are almost identical. Beyond these LEBT settings significant discrepancies between nominal beam current and pencil beam current are detected.

The reduction of the maximum beam current of the pencil beams from Faraday cup1 to Faraday cup2 indicates further particle losses downstream of the first Faraday cup.
In the case of the $11\,mm$ iris at solenoid1 currents of $I_{sol1} = 720\,A$ to $I_{sol1} = 760\,A$ the pencil beam current and the beam current of the nominal beam at Faraday cup2 are almost identical. Hence, the losses of the nominal beam have

to be comparable with the particle losses of the pencil beam generated with the 11 mm iris. Based on the pencil beam current measurements using Faraday cup1 it was concluded that a minimisation of the particle losses is obtained by focusing the beam waist close to the 11 mm iris.
In the case of the pencil beam generated with the 5 mm iris the beam current maximum was observed at a solenoid1 current of $I_{sol1} = 740\,A$, where the beam is focused into the iris. The comparison of the nominal beam current with the pencil beam current (5 mm iris) at this solenoid1 setting shows a minor reduction of the beam current. The reduction of the final beam current with respect of the nominal beam current indicates further particle losses at the iris and that the beam size at the 5 mm iris exceeded 5 mm.
In the case of the 11 mm iris the maximum signal was obtained at a solenoid current of $I_{sol1} = 720\,A$. The increased aperture of the 11 mm iris with respect to the 5 mm iris leads to a mitigation of the particle losses at the iris. Hence, a beam waist shifted downstream leads to a further minimisation of the particle losses along the LEBT by minimisation of the particle losses at the second solenoid.

In summary of these conclusion:
In the case of the 5 mm iris at each LEBT setting a collimating effect was observed. At LEBT configurations, at which the beam is focused close to or onto the iris, the collimation impact of the iris is mitigated leading to higher pencil beam currents and so higher transverse emittances are expected. Hence, the generation of pencil beams by using one of the irises is only reasonably at solenoid1 currents below $I_{sol1} = 700\,A$ or above $I_{sol1} = 800\,A$. Below a solenoid1 current of $I_{sol1} = 700\,A$ LEBT settings for the RFQ commissioning were defined for nominal operations. At these settings the pencil beam current at the RFQ injection plane can be varied from 0.2 mA to 7.8 mA, Tab. A.4 (11mm iris) and Tab. A.5 (5mm iris).

Pencil Beam Emittance

In the solenoid1 parameter space from $I_{sol1} = 560\,A$ to $I_{sol1} = 680\,A$ emittance measurements of the pencil beams were conducted. The LEBT settings for RFQ injection listed in Tab. A.2 were used. The measurement results are listed in Tab. A.4 (11mm iris) and Tab. A.5 (5mm iris). Depending on the choice of the iris and LEBT configuration the transverse emittance varies from $\varepsilon = 0.3\,\pi\,mm\,mrad$ to $\varepsilon = 0.03\,\pi\,mm\,mrad$ related to the variation of the pencil beam current from 7.8 mA to 0.2 mA. The pencil beam Twiss parameters correspond to the Twiss parameters of the nominal beam.

Simulated RFQ Performance

In order to estimate the pencil beam parameters at the exit of the RFQ simulation beams based on the measured phase space distributions and beam currents of the pencil beams were generated and tracked through the RFQ[13][38]. The

[13]Thanks to P.A. Posocco for performing the RFQ simulation.

simulation results are summarised in Tab. A.6 (11mm iris) and Tab. A.7 (5mm iris).
At the injection of a beam into a periodical focusing structure such as the RFQ the matching of the beam parameters to the lattice optics is crucial. Due to non-linear field components a mismatch of the beam properties leads to an increase of the emittance. In presence of aperture constraints this emittance growth can lead to an enhancement of particle losses, as seen at the RFQ simulation results of the nominal beam, Tab. A.3.
Due to the smaller emittance of the pencil beams the RFQ transmissions are between 90% and 100%[14]. Due to the higher transmission the pencil beam current at the RFQ exit is determined by the settings of the first solenoid. The preservation of the pencil beam emittance is defined by the RFQ matching. By the adjustment of the second solenoid an intended mismatch can be generated leading to a degradation of the emittance preservation. The intended RFQ mismatch can be used to generate a specific increase of the transverse emittance.
Depending on the LEBT settings the generation of pencil beams with transverse emittances in the range from $\varepsilon = 0.04\,\pi\,mm\,mrad$ to
$\varepsilon = 0.5\,\pi\,mm\,mrad$ and pencil beam currents of $0.2\,mA$ to $7\,mA$ is posssible.

[14] At three scenarios a transmission below 90% was obtained caused by a high transverse emittance in combination with a RFQ mismatch.

3

Optimisation of the Linac4 Transfer Line

3.1 Introduction

The performance of Linac4 is determined and limited by the design and optimisation of its components. An additional performance limitation is given by the location of Linac4 at CERN. As the beam has to be guided from the exit of Linac4 to the PS-Booster injection point, the design of the transfer line becomes crucial in terms of preservation of beam quality. In the design phase several scenarios for the location of Linac4 were analysed and discussed. With respect to future upgrade scenarios the 'Green Field' solution was chosen, [39]. In this scenario Linac4 will be placed close to Linac2 to re-use parts of the existing transfer line between Linac2 and the PS-Booster, Fig. 0.8. To connect Linac4 with the existing accelerator complex the construction of a $70\,m$ long transfer line is required.
Due to radiation activation issues the vertical level of Linac4 is $2.5\,m$ lower than the vertical level of the Linac2, PS-Booster and PS. In order to compensate this offset a vertical chicane was implemented in the design of the new transfer line, [40]. The total length of the final transfer line between Linac4 and the PS-Booster amounts to $180\,m$, along which the beam has to be matched to the PS-Booster and its quality needs to be preserved.
An overview of the beam parameters at the Linac4 exit and of the different injection schemes is given in the first section. The second section is focused on the layout and the beam dynamics of the transfer line. On the basis of the transfer line optics of 2009 the critical sections of the transfer line beam dynamics are introduced. In the framework of this thesis several modifications of the transfer line optics were conducted. In the following these modifications, their motivations and their impact on the transfer line beam dynamics are explained. To ensure the feasible beam transport using the new transfer line optics its performance is tested and benchmarked with the former reference optics, i.e. transfer line optics of 2009. For the optimisation and control of the beam parameters beam diagnostics are essential. Three diagnostics lines are foreseen for the measurement of the transverse emittance, of the beam energy and of the beam energy spread. The working principle of the transverse emittance measurement line is briefly discussed. In the framework of this thesis a new layout of the spectrometer line, called LBS-line, used for the measurement of the beam energy and energy spread is developed. Its layout, beam dynamics and limitations are explained in detail concluding this chapter.

3.2 Linac4 Beam Parameters & PS-Booster Injection Requirements

3.2.1 Beam Parameters at the Exit of Linac4

Along the acceleration structure of Linac4 the transverse and longitudinal dimensions of the beam are maintained compact. The small transverse beam size is required to maximise the efficiency of the accelerator cavities by small bore radii. As a consequence the Linac4 layout is characterised by a high phase advance lattice with a high density of transverse focusing elements, i.e. quadrupole magnets. In order to maximise the acceleration efficiency synchronous phases close to the wave crest are chosen. With increasing particle energy a mitigation of the space charge effects is expected and the bunch length can be reduced allowing an adjustment of the synchronous phase closer to the wave crest. At the exit of Linac4 compact bunch dimensions with rms beam length of $2.3\,mm$, transverse rms beam sizes of $1.6\,mm$ (horizontal) and $2.3\,mm$ (vertical) are expected. The design beam parameters are listed in Tab. 3.1.

Parameter	**Horizontal Plane**	**Vertical Plane**	**Longitudinal Plane**
Emittance (rms)	0.299 $[\pi\, mm\, mrad]$	0.299 $[\pi\, mm\, mrad]$	0.160 $[\pi\, deg\, MeV]$
β (Twiss) α (Twiss)	5.51 $[m]$ 1.77 $[-]$	10.64 $[m]$ -2.91 $[-]$	22.41 $[\frac{deg}{MeV}]$ 0.147 $[-]$
Beam Size(rms)	1.64 $[mm]$	2.3 $[mm]$	1.9 $[deg]$ @352.2MHz 2.3 $[mm]$
Beam Divergence (rms)	0.61 $[mrad]$	0.67 $[mrad]$	85 $[keV]$

Table 3.1: Bunch Parameters at the Linac4 Exit
Due to the focusing structure of Linac4 compact bunch dimensions are expected at the exit of the accelerator structure. In this table the simulated bunch parameters are summarised. The Linac4 RF frequency is 352.2 MHz.

3.2.2 PS-Booster Injection Schemes and Parameters

At the PS-Booster injection several Linac4 bunch trains are combined into one PS-Booster bunch. The number of Linac4 bunches to be accumulated in one PS-Booster bunch depends on the later use of the bunch. An upper limit of the bunch train length is defined by the PS-Booster circumference and the synchronous phase. At Linac4 the H^- ions will be accelerated to a velocity of $\beta \cdot c = 0.5\,c$. The RF frequency of Linac4 is $352.2\,MHz$. A bunch train consisting of 355 bunches is characterised by a length of approximately $150\,m$. The synchronous phase and the RF frequency of the PS-Booster define the maximum length of bunch trains injectable into the RF-buckets of approximately 60 % of the PS-Booster circumference corresponding to a sequence of 222 Linac4 bunches. Consequently, 133 bunches in a periodicity of 355 bunches need to be

dumped from the beam pulse[1], [14].
The PS-Booster injection is a multi-turn injection using 65 to 100 bunch trains with 222 Linac4 bunches each combined into one PS-Booster bunch, Fig. 3.1.

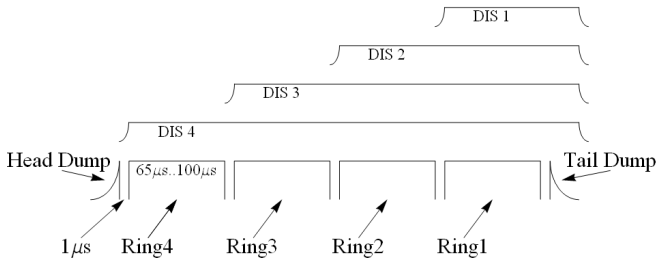

Figure 3.1: Pulse Scheme for PS-Booster Injection
This figure illustrates the beam pulse sequence for the beam injection into the different PS-Booster rings. Head and tail of the beam pulse are directed into beam dumps. The length of the pulse sequences for each PS-Booster ring is in the order of $65\,\mu s$ *to* $100\,\mu s$*, [14].*

The source beam pulse is segmented into six subsections. Due to the ignition process of the source and due to effects such as the RF-beam loading of the accelerator elements it is expected that the first segment of the beam pulse is characterised by a suboptimal beam quality. Therefore, the first pulse segment will be directed into the 'head' dump of the PS-Booster. The middle pulse segments will be injected into the PS-Booster buckets of the four PS-Booster rings. At the final segment of the beam pulse a degradation of beam quality is expected by the extinction of the source plasma. Hence, the final pulse segment will be directed into the 'tail' dump of the PS-Booster. In between the six segments time slots of approximately $1\,\mu s$ are needed for the field ramping of the distributor kicker magnets.
Since a mismatch between the beam properties and lattice optics leads to an emittance growth [36], the tuning of the transfer line optics for an optimised beam matching is crucial. In Fig. 3.2 the PS-Booster beam optics is shown, to which the beam has to be matched.
At the injection point the beam optics is characterised by a horizontal dispersion of $D_x = -1.4\,m$ and transverse β-functions of $\beta_y = 4\,m$ (vertical) to $\beta_x = 5.5\,m$ (horizontal). In order to vary the particle distribution of the transverse phase space of the PS-Booster bunches several sets of matching Twiss parameters were defined, Tab. 3.3. The impact of the different injection Twiss parameters is illustrated in Fig. 3.3.

The energy spread acceptance depends on the phase space painting mode. In the first phase of Linac4 operation a PS-Booster injection without longitudinal

[1]In a later upgrade phase of the CERN accelerator complex, at which Linac4 will be used as injector for the Super Conducting Proton Linac (SPL), a significantly higher performance of the chopper will be required, at which 3 of 8 bunches will have to be dumped.

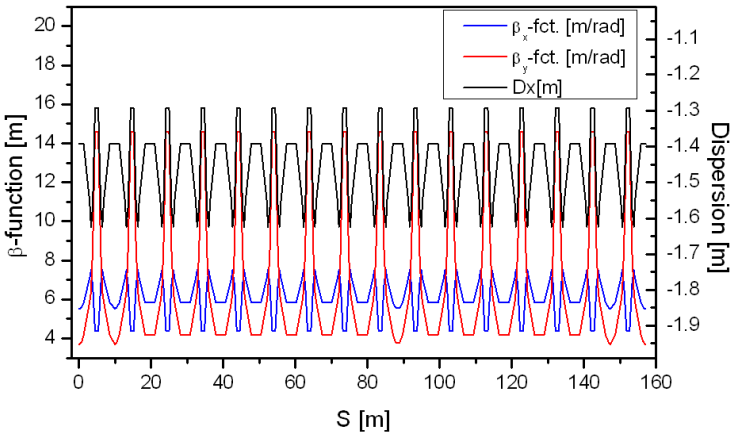

Figure 3.2: Optics of the PS-Booster

In this plot the development of the β-functions and the horizontal dispersion along the PS-Booster is shown. The injection point is at position $0\,m$. At this location the PS-Booster optics is characterised by the horizontal dispersion of $D_x = -1.4\,m$ and transverse β-functions of $5.5\,m$ (horizontal) and $4\,m$ (vertical).

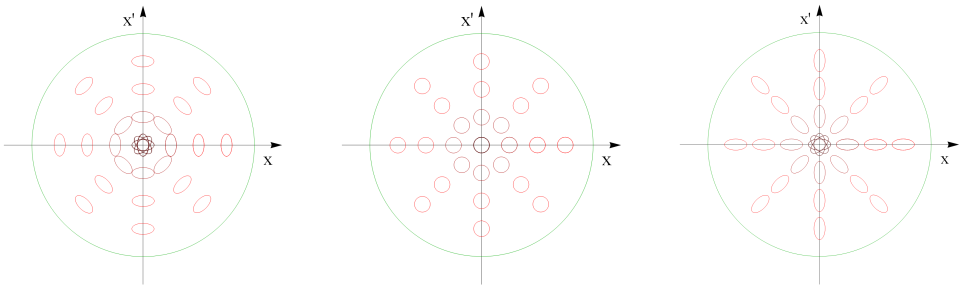

(1) Small Beta (2) Matched Beta (3) Big Beta

Figure 3.3: Transverse Phase Space Painting Schemes

For the PS-Booster injection a multi-turn bunch injection is planned. The phase space distribution of the PS-Booster bunch (green circle) will be defined by the Twiss parameters of the Linac4 bunches (red ellipses). In the case of a matched PS-Booster injection the shape of the phase space distribution of the Linac4 bunches is identical to the shape of the PS-Booster bucket (2). Due to an intended mismatch of the injection Twiss parameters a modulation of the transverse phase space distribution can be designed, (1) and (3). Studies of the PS-Booster performance with the different phase space painting schemes are ongoing [14][41].

phase space painting is envisaged. So, the energy spread limitation is determined by the height of the RF-bucket of the PS-Booster. In a later operation phase of Linac4 the use of longitudinal phase space painting schemes is planned. For this purpose an energy modulation of e.g. $\Delta E = \pm 1.2\,MeV$ along the bunch trains is needed. Due to this energy modulation the upper limit of the energy

spread is reduced. E.g. in the case of an energy modulation of $\Delta E = \pm 1.2\,MeV$ a limit of the Linac4 energy spread of $\sigma_e = 120\,keV$ is specified, Tab. 3.2.

Injection Scheme	**Energy Spread (rms)** $[keV]$
Without Energy Painting	450
With Energy Painting $[\pm 1.2 MeV]$	120

Table 3.2: PS-Booster Injection - Energy Spread Limitations
This table summarises the energy spread acceptance for the two main different injection schemes. The energy spread limit depends on the energy modulation. Additional longitudinal phase space painting schemes with reduced energy modulation are under discussion.

The energy modulation leads to a coupling of the longitudinal and transverse phase space painting in the case of dispersion matched PS-Booster injection. In order to decouple transverse and longitudinal phase space painting injection parameter sets with vanishing horizontal dispersion were defined, Tab. 3.3.

Configuration	α_x	β_x $[m]$	α_y	β_y $[m]$	D_x $[m]$	D'_x
SmallBeta-1.4m (Dispersion matched)	0	2.5	0	2	-1.4	0
MediBeta-1.4m (all matched)	0	5	0	4	-1.4	0
BigBeta-1.4m (Dispersion matched)	0	10	0	8	-1.4	0
SmallBeta0m	0	2.5	0	2	0	0
MediBeta0m (Twiss matched)	0	5	0	4	0	0
BigBeta0m	0	10	0	8	0	0

Table 3.3: PS-Booster Injection - Twiss Parameters
In this table the injection parameters for the transverse phase space painting are summarised. To optimise the transverse phase space distribution of the PS-Booster bunches three sets of transverse Twiss parameters were defined. The impact of the parameter variation is illustrated in Fig. 3.3. At the injection point the PS-Booster optics defines a horizontal dispersion of $D_x = -1.4\,m$. In the case of longitudinal phase space painting a dispersion matched injection will cause a coupling of the longitudinal and the transverse painting schemes. To avoid this coupling injection sets with vanishing dispersion were defined.

3.3 Transfer Line Optics

A major part of the present thesis is focused on the optimisation of the transfer line beam dynamics. In order to illustrate the complexity of the transfer line beam dynamics and the enhancement of the transfer line performance the status of the former reference transfer line optics is presented.

3.3.1 Former Transfer Line Optics

Former Transfer Line Layout

In the first design proposal parts of the transfer line between Linac2 and PS-Booster will be re-used [39]. Due to the location of Linac4 the construction of a new transfer line part to guide the beam to the re-used transfer line is required. At this new part two dipole magnets, each applying a beam deflection of $35\,deg$, are foreseen to direct the Linac4 beam towards the connection point with the existing transfer line. The transverse focusing scheme of the new transfer line is based a quadrupole doublet design. Due to radiation protection issues the vertical level of Linac4 is shifted down by $2.5\,m$. As a consequence a vertical step was implemented in the new transfer line [40].
In the existing part of the transfer line the main challenge is to ensure a low loss beam transport along the distributor section within PS-Booster matching. The PS-Booster consists of four accelerator rings. In addition to these four rings two beam dumps are installed. In order to distribute the six segments of the beam pulse into the accelerator rings and beam dumps a sequence of fast ramping kicker magnets[2] are installed. In the final design of these magnets the aperture is significantly reduced for sake of their performance leading to a higher potential of particle losses. To illustrate the complexity of the transfer line layout the sequence of beam optics elements such as dipole magnets (yellow) and quadrupole magnets (green - horizontal focusing, red - vertical focusing) is shown in Fig. 3.4.

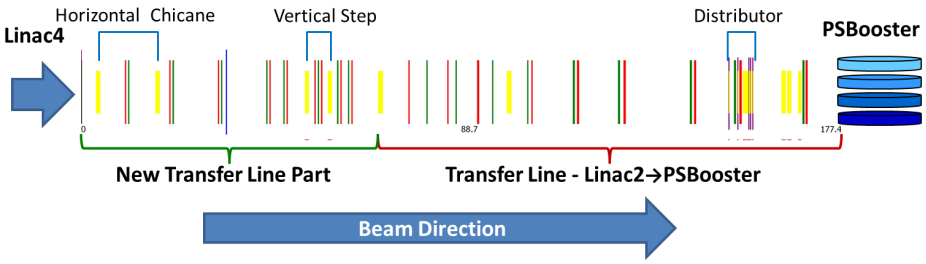

Figure 3.4: Schematic of Transfer Line Layout
In this schematic the layout of the transfer line elements is illustrated. Locations and longitudinal dimensions of quadrupoles (red and green lines), dipoles (yellow lines) and cavities (blue lines) are indicated by location and width of the line.

Beam Dynamics of the Transfer Line

The transfer line between Linac4 and the PS-Booster consists basically of two parts. A new transfer line from the exit of Linac4 to the transfer line between Linac2 and the PS-Booster will be constructed to transmit the beam to the existing accelerator complex. In this part the beam dynamics is optimised to

[2]Kicker magnets are short dipole magnets, whose magnetic field can be ramped up in less than $1\,\mu s$.

minimise transverse emittance growth and to adapt the bunch energy spread to the PS-Booster injection parameter. Parts of the existing transfer line between Linac2 and the PS-Booster will be re-used. The beam optics elements of this part will be upgraded for the increased beam rigidity of the Linac4 beams. In Fig. 3.5 and Fig. 3.6 the transverse β-functions and transverse emittances along the transfer line are plotted.

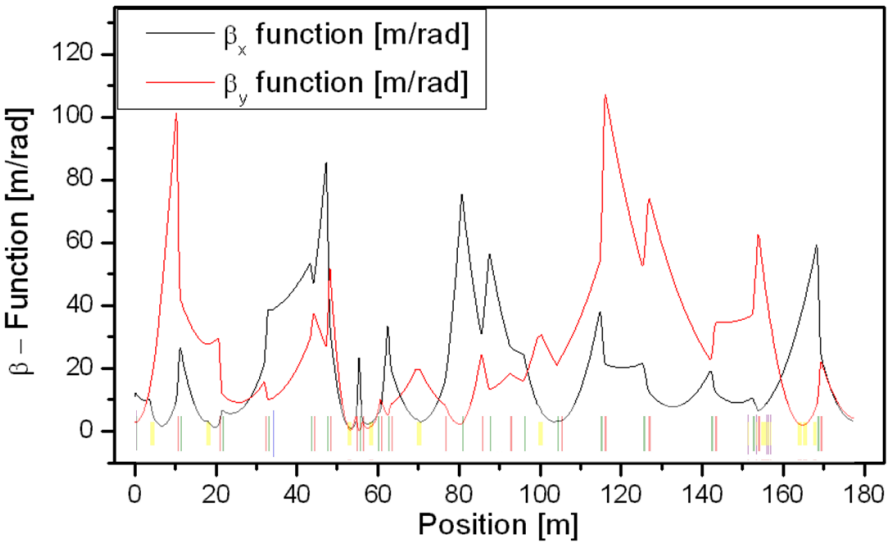

Figure 3.5: Transverse β-functions - Old Optics
In this figure the transverse β-functions along the transfer line are plotted.

Along the accelerator structure of Linac4 the beam dimensions are maintained compact to maximise the RF-power use. This is accomplished using a dense focusing scheme of quadrupole magnets and cavities. These compact beam dimensions lead to intense space charge fields. In order to minimise the space-charge-driven emittance-growth the variation of the beam size needs to be minimised. Along the transfer line the average space between transverse focusing elements is increased. This leads to a beam transport with lower phase advance and higher average beam dimensions. Due to the different focusing strategies of Linac4 and transfer line the beam optics of the first transfer line part is crucial in terms of the transverse emittance preservation.
As at the exit of Linac4 two dipole magnets will be used to deflect the Linac4 beam, the preservation of transverse emittance has to be accomplished in presence of dispersion control. The increase of transverse emittance is caused by space-charge-driven emittance-growth and the interplay of space charge effects and dispersion. In the old design the transverse emittance growth could be limited below 30 %. By changes of the layout in the first 15 meter of the transfer line and the optimisation of the beam optics the transverse emittance growth could be reduced to less than 10%, section 3.3.2.
Downstream the first bending section the use of a debuncher cavity is foreseen to reduce the energy spread of the Linac4 bunches to match the PS-Booster

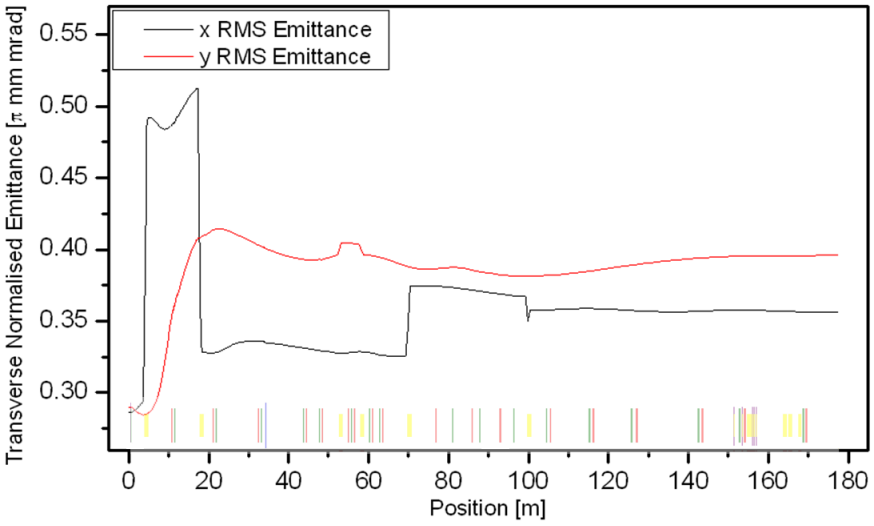

Figure 3.6: Transverse Emittances - Old Optics

In this figure the transverse emittances along the transfer line are plotted. The steps of the transverse emittance, e.g. at the first dipole magnet at 4 m, are calculation artefacts based on a non-vanished internal dispersion. A significant increase of the vertical emittance at the first 20 meter is simulated. At this section intense space charge effects are expected. The rapid changes of the vertical beam size leads to an enhancement of the space-charge-driven emittance-growth.

injection parameters. The design of the debuncher cavity is based on the design of the PiMS cavities. Due to the different phase advances lattices of the Linac and the transfer line the bore radius of the debuncher cavity had been increased from $r = 20\,mm$ to $r = 30\,mm$, [42]. With respect to the surrounding beam optics elements the debuncher cavity poses an aperture bottleneck. To reduce potential particle losses at the cavity the transfer line optics was adapted to this aperture limitation.
For the performance optimisation of the debuncher cavity its position is crucial, as it determines the bunch length inside the cavity and the required synchronous phase adjustment. These parameters define the RF-power needed and the energy spread at the PS-Booster injection, section 3.3.3.
A third critical section of the transfer line beam dynamics is the vertical chicane. This chicane is designed achromatic within a short length to minimise the coupling between the transverse planes. Due to the compact design the vertical chicane is characterised by a higher phase advance. The challenge of the beam dynamics is the matching between the low phase advance sections and the chicane optics within the minimisation of particle losses, section 3.3.4.
In the second part of the transfer line the main challenge of the beam dynamics design is the beam matching to the PS-Booster within a low-loss beam transport through the distributor section. To cope with the higher beam rigidity of the Linac4 beams the design of the distributor kicker magnets is changed. In the updated design the aperture of these magnets is significantly reduced allowing

higher field strengths within a comparable field ramping time. As a consequence the distributor section is the main aperture limitation of the transfer line. In between the distributor section and the PS-Booster injection point only two quadrupoles are installed. Hence, the freedom of the PS-Booster matching is strongly restricted by this aperture limitation.

3.3.2 Preservation of the Transverse Emittance

The beam dynamics of the accelerator structure and the transfer line are characterised by different focusing schemes leading to a beam transport marked by different phase advances. In order to illustrate the contrast between the different focusing strategies the sequence of elements (cavities blue, dipole magnets yellow, quadrupole magnets red and green) of the last PiMS segment and of the transfer line are plotted in Fig. 3.7.

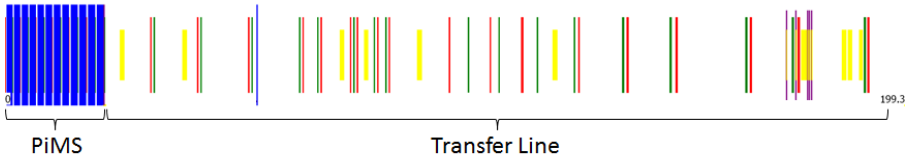

Figure 3.7: Layout of the Beam Optics Elements - last Module of PiMS and old Transfer Line

In this scheme the sequence of beam optics elements of the last modules of the PiMS and of the transfer line are illustrated. The locations and thickness of the lines are based on the locations and longitudinal dimensions of the represented elements, which are cavities (blue), dipole magnets (yellow) and quadrupole magnets (red and green).

In order to minimise the space-charge-driven emittance-growth major variations of the transverse beam size within short distances have to be avoided. In the old beam optics design intense variations of the vertical beam size along the first $20\,m$ meter of the transfer line were conducted to minimise the potential of particle losses. Based on investigations of the beam optics development along this section a new layout of the transfer line elements was developed in the framework of this thesis, so called "new optics". Due to this modified layout the strong variations of the transverse beam sizes were reduced within the minimisation of potential particle losses. In Fig. 3.8 the development of the transverse beam sizes along the first transfer line section is plotted. In the old transfer line layout a quadrupole doublet in between the first two bending magnets is used to close the space-charge dispersion-bump, section 1.2.1. In this configuration a significantly increased, vertical beam size is needed at the entrance of the quadrupole doublet to minimise potential particle losses at the second dipole. The focusing impact of the quadrupole doublet leads to a rapid reduction of the vertical beam size. Within the first 20 metre of the transfer line the vertical beam size increases from $\sigma_y = 1\,mm$ to $\sigma_y = 8\,mm$ and is reduced from $\sigma_y = 8\,mm$ below $\sigma_y = 5\,mm$. This leads to an increase of the vertical emittance

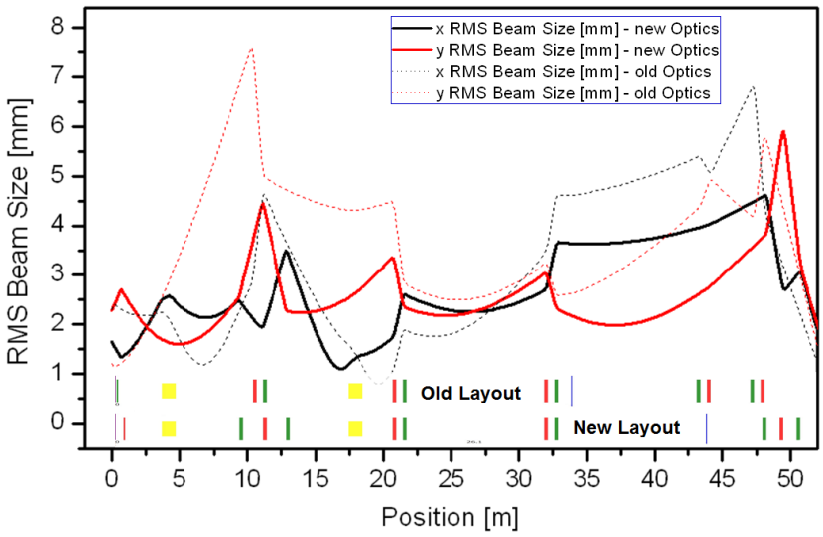

Figure 3.8: Development of the transverse Beam Sizes

In this plot the development of the transverse beam sizes along the first 50 *meter of the transfer line is shown. Due to the intense variations of the vertical beam size a significant increase of the vertical emittance is caused, Fig. 3.6. In the new transfer line optics the variation of the transverse beam sizes are mitigated and an almost perfect preservation of the transverse emittance has been accomplished.*

from $\varepsilon_y = 0.3\,\pi\,mm\,mrad$ to $\varepsilon_y = 0.4\,\pi\,mm\,mrad$, Fig. 3.9.
Two major changes of the transfer line layout were realised. The first change is the re-location of the final quadrupole of the PiMS at the entrance of the transfer line. This magnet is shifted downstream by $0.5\,m$. The second and more important modification of the layout is the replacement of the quadrupole doublet between the dipole magnets by a quadrupole triplet with a significantly increased drift space between the quadrupoles.
The performance limitation of the old layout is based on the focusing structure in between the two dipole magnets. The quadrupole doublet is used to close the horizontal space-charge dispersion-bump and it is needed to control the development of the transverse beam sizes.
Due the short drift space of $0.5\,m$ between the doublet quadrupoles high field gradients of the quadrupoles are required to control the dispersion. To ensure a low-loss beam transport a high sensitivity of the vertical beam size is created at the entrance of the quadrupole doublet. The high field gradients of the doublet quadrupoles lead to a significant variation of the vertical beam size. In order to mitigate the variation of the vertical beam size lower field gradients of the doublet quadrupoles are needed. The reduction of the field gradients is accomplished by increasing the drift space between the doublet quadrupoles[3].

[3] A further reduction of the variation of the transverse beam size could be accomplished by a further increase of the quadrupole spacing. For the integration of diagnostics elements a quadrupole spacing of $1.5\,m$ is chosen.

Furthermore, the doublet structure in between the dipole magnets was replaced with a triplet quadrupole structure to lower maximum vertical beam size.
The re-location of the final PiMS quadrupole magnet is required to optimise the beam transport between the dipole magnets. In the new transfer line optics the beam sizes of both transverse planes are maintained within the beam dimensions, which are expected along the Linac. Due to these changes the emittance growth is limited below 10 % in the new transfer line optics. A comparison of the development of the transverse emittance along the transfer line is presented in Fig. 3.9.

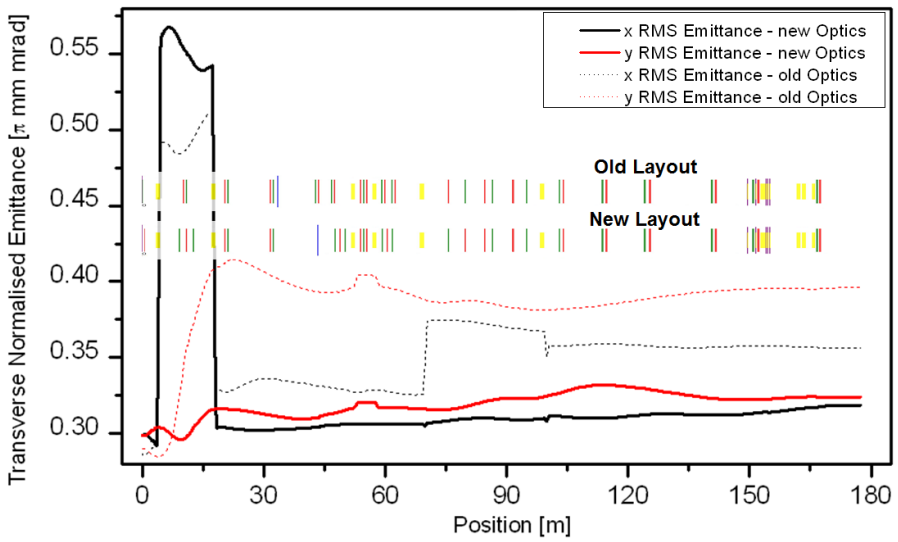

Figure 3.9: Development of the Transverse Emittance
This plot shows the development of the transverse emittances along the transfer line for the old and new optics. At the development of the emittances steps are plotted at the locations of dipole magnets. These emittance steps are calculation artefacts of the simulation code, which are used to close the space-charge dispersion-bumps and to minimise the transverse emittances. The comparison of the emittance developments shows that the increase of the vertical emittance of the old transfer line optics has been significantly reduced. In the final transfer line optics the emittance growth is limited below 10 %.

3.3.3 Debuncher Cavity

For the intended longitudinal phase space painting an upper limitation of the bunch energy spread of $\sigma_e = 120\,keV$ is defined, [43]. In order to meet the energy spread parameter the use of a debuncher cavity in the transfer line is required. For the reduction of the energy spread of the Linac4 beam two effects will be used.
The first effect is based on the low relativistic velocity of the particles at the Linac4 exit. As the particle velocity is far below the speed of light, the energy spread equals to a considerable velocity spread. Thus, particles with higher

kinetic energy travel faster and arrive earlier at certain locations in the transfer line such as the debuncher cavity, called dispersive effect. Due to this effect the uncorrelated energy spread of the beam at the Linac4 exit will be transformed within tens meter of the transfer line into a correlated energy spread, at which the longitudinal position of the particles are correlated to their energy, Fig. 3.10.

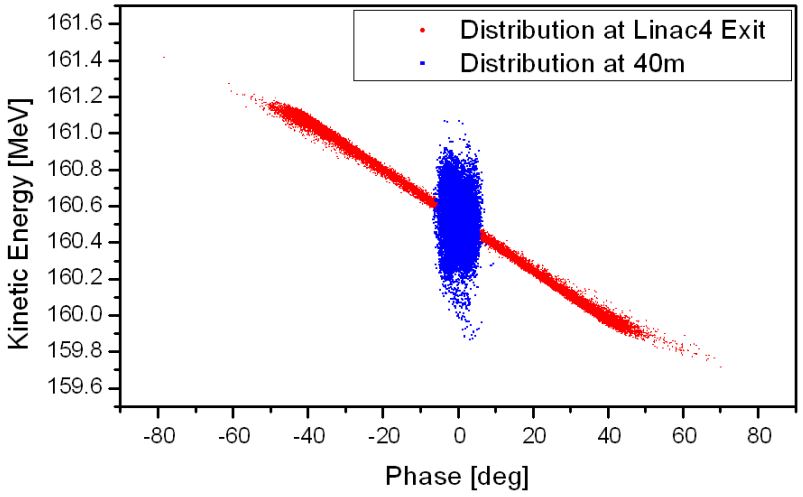

Figure 3.10: Energy-Phase Distribution at Linac4 Exit and at Debuncher Cavity
In this diagram the longitudinal phase space distributions at the exit of Linac4 and 40 m further downstream are plotted. At the exit of Linac4 the longitudinal phase space distribution is uncorrelated. Due to the impact of a transfer section without longitudinally focusing elements the uncorrelated energy spread is transformed into a correlated energy spread, at which particle energy and particle position are correlated.

At the debuncher cavity the synchronous phase of the RF-field will be set to $\varphi = -90$ degree[4], i.e. particles at the bunch centre will not be accelerated. Those particles, which are higher energetic, will arrive the cavity earlier and they will be decelerated. Particles, which are lower energetic, will arrive the cavity after the bunch centre. During the bunch centre passes the cavity the direction of the RF-field changes and the lower energetic particles will be accelerated. The amount of acceleration or deceleration is determined by the arrival time and the field strength of the RF-field. An illustration is presented in Fig. 3.11.
Due to the individual acceleration of the particles according to their longitudinal positions the energy spread will be reduced. The longitudinal emittance and the bunch length are maintained.
The applied acceleration or deceleration of a particle is determined by the RF-field strength, i.e. cavity voltage, and by the RF-phase, at which the particle passed through the debuncher cavity. Due to the energy spread the bunch length

[4]The definition of the RF-phase is not fixed determined. In Linac accelerators the phase "0 degree" marks the crest of the RF-wave (maximum acceleration). In circular accelerators the phase "0 degree" characterises the RF-phase, at which the bunch centre will not be accelerated and a longitudinal focusing is applied on the particle ensemble (steady state).

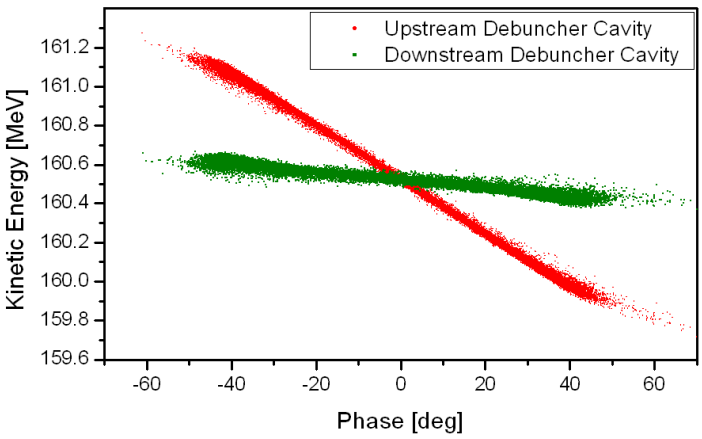

Figure 3.11: Impact of the Debuncher Cavity
In this plot the longitudinal phase space distribution upstream and downstream of the debuncher cavity is shown. As the difference between particle energy and average particle energy is correlated with the longitudinal distance between the particle and the bunch centre, a controlled acceleration of the particle can be realised by the adjustment of the RF-field strength and RF-phase.

increases along the transfer line. Thus, the bunch length at the cavity depends on the position of the debuncher cavity.
For the longitudinal phase space painting a modulation of the average particle energy of e.g. $\Delta E = \pm 1.2\,MeV$ along the bunch trains is needed. This energy modulation leads to a variation of the arrival time of the particle ensembles, at which an adjustment of the RF-phase will be required, so called RF-phase swing. The final RF-power needed of the debuncher cavity are defined by the cavity voltage and the RF-phase swing. These two parameters are determined by the position of the debuncher cavity and the beam characteristics.

Cavity Voltage

The development of the energy spread of the Linac4 bunches is determined by space charge effects. At the exit of Linac4 the high charge density leads to intense space charge effects causing an increase of the energy spread, Fig. 3.12.

As the transverse focusing structure of the transfer line is used to maintain the transverse beam dimensions, the intensity of the space charge fields is directly coupled to the development of the bunch length, Fig. 3.13.
The amount of energy spread reduction is mainly determined by the cavity voltage and by the bunch length. Due to this interplay the further development of the bunch length will be affected, Fig. 3.13. A limitation of the cavity position is defined by the bunch length. In order to reduce the energy spread the bunch length must not exceed the half RF wave length, i.e. the bunch length is limited

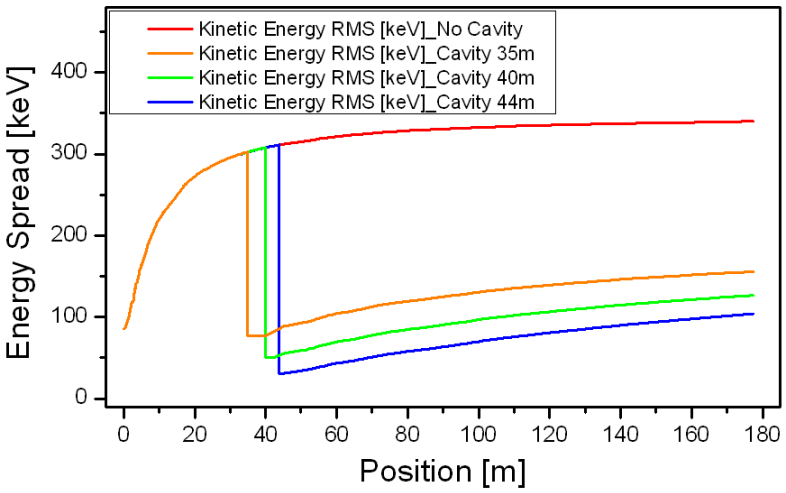

Figure 3.12: Energy Spread Development along the Transfer Line
In this diagram the development of the energy spread along the transfer line is plotted. The impact of a debuncher cavity with a cavity voltage of $700\,kV$ *on the energy spread development is shown for three different cavity positions. Due to the increased bunch length at further downstream cavity positions a superior energy spread reduction is obtained.*

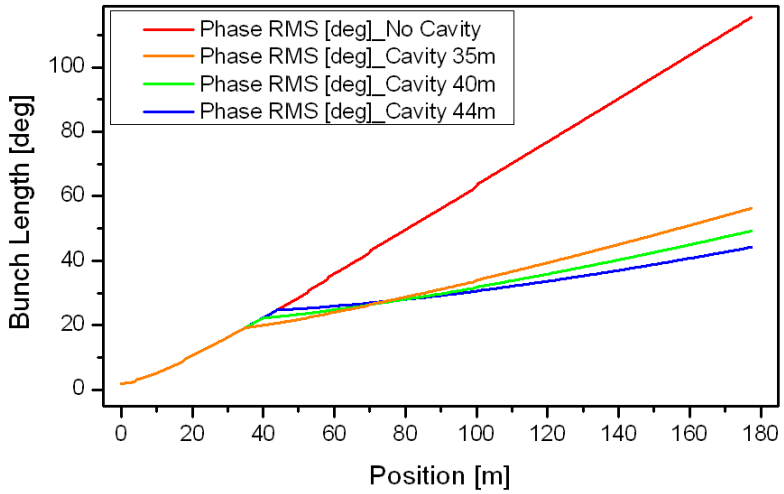

Figure 3.13: Development of the Bunch Length along the Transfer Line
In this plot the development of the bunch length along the transfer line is shown. The use of the debuncher cavity leads to a lower beam energy spread causing a reduction of the expansion velocity of the bunch length. Due to the increased bunch length at further downstream positions of the debuncher cavity an enhanced energy spread reduction for a constant cavity voltage of $700\,kV$ *is obtained leading to a stronger reduction of the bunch length expansion. The Linac4 RF-frequency is* $352.2\,MHz$.

to:

$$\Phi_{bunch} < \beta \cdot \lambda_{RF}/2 \ . \tag{3.1}$$

For the Linac4 operation also the use of special beams with reduced intensity are planned and foreseen for a PS-Booster injection. Due to the lower intensity less intense space charge effects are expected, which leads to a lower increase of the energy spread. As a consequence less reduction of the energy spread will be required and a lower cavity voltage for these special beams is needed. In order to meet the specified energy spread the cavity voltage has to be adjusted to the cavity position and the beam intensity. For the nominal beam intensity of $I = 62.5\,mA$ and for a reduced beam intensity of $I = 30\,mA$ the required cavity voltages for different cavity position are plotted in Fig. 3.14.

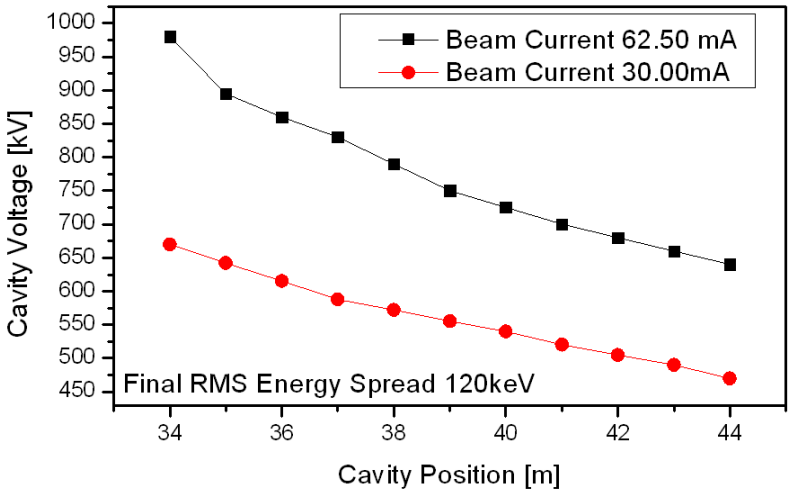

Figure 3.14: Cavity Voltage Requirement

In this plot the required cavity voltage to accomplish an energy spread of $\sigma_{energy} = 120\,keV$ *is plotted in dependence of the cavity positions. For the simulation of the space charge impact the nominal beam current of* $I = 62.5\,mA$ *and a reduced beam current of* $I = 30\,mA$ *were assumed. Due to the lower beam current less intense space charge effects are leading to a lower cavity voltage needed. At upstream cavity positions such as* $34\,m$ *intense space charge effects are expected for the nominal beam, which lead to a significant increase of the energy spread downstream of the cavity. At these positions an enhanced reduction of the energy spread is needed to compensate the further energy spread growth.*

RF-Phase Swing

Due to the modulation of the average bunch energy along the bunch trains a variation of the arrival time of the single bunches is caused. As the cavity

phase has to be matched with the arrival time of each bunch, a modulation of the RF-phase of the cavity according to the energy modulation has to be accomplished, called RF-phase swing. In Fig. 3.15 the required phase swing for different cavity positions and different energy modulations is plotted.

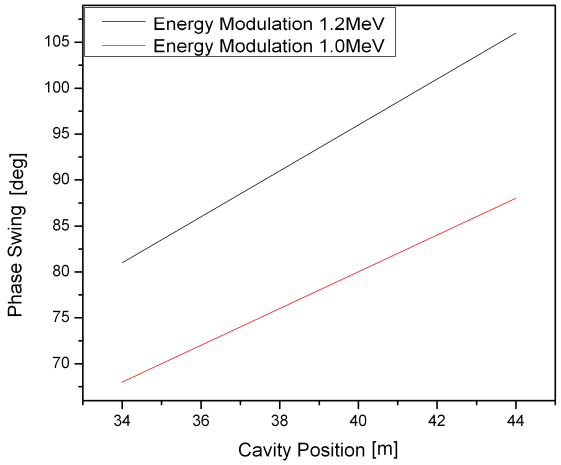

Figure 3.15: RF-Phase Swing

In this plot the required RF-phase adjustment, called RF-phase swing, depending on the debuncher cavity position is plotted. Two different scenarios of energy modulation, $\Delta E_1 = \pm 1.2\,MeV$ *and* $\Delta E_2 = \pm 1.0\,MeV$*, were studied. The minimum required phase swing will be approximately* $65\,deg$ *for an energy modulation of* $\Delta E = \pm 1.0\,MeV$ *and the maximum required phase swing will be in the order of* $105\,deg$ *for an energy modulation of* $\Delta E = \pm 1.2\,MeV$*.*

These phase swing values are calculated under the assumption of negligible dispersion effects. At the calculation procedure the kinetic energy is used to compute the relativistic velocity, Eq. 3.2. Based on the relativistic velocities the travel time t for a certain distance l is determined, Eq. 3.3. The combination of the RF-frequency of $352.2\,MHz$ and the time difference between particle with nominal energy and modulated energy leads to the RF-phase swing, Eq. 3.4.

$$\beta = \sqrt{1-\gamma^{-2}} = \sqrt{1-\frac{E_0}{E_0+T}} \tag{3.2}$$

$$t\,(l) = \frac{l}{c\beta} \tag{3.3}$$

$$\Phi_{Swing}\,[deg] = 360deg \cdot \frac{l \cdot f}{c} \cdot \left(\frac{1}{\beta_0} - \frac{1}{\beta_{\pm 1.2MeV}}\right) \tag{3.4}$$

An alternative approach to calculate the phase swing is given by the 6×6 transfer matrix formalism, section 1.1 [18][24]. The following convention of the

coordinate system is used,

$$\vec{x} = \begin{pmatrix} x \\ x' \\ y \\ y' \\ \delta l \\ \frac{\Delta p}{p} \end{pmatrix}. \tag{3.5}$$

A longitudinal displacement is determined by:

$$\delta l = x_0 \cdot R_{51} + x_0' \cdot R_{52} + y_0 \cdot R_{53} + y_0' \cdot R_{54} + \delta l_0 \cdot R_{55} + \frac{\Delta p}{p} \cdot R_{56}. \tag{3.6}$$

At the exit of Linac4 a correction of transverse displacements in position and angle is assumed. Furthermore, it can be assumed that the initial longitudinal distance between the bunches will be an integer of the RF-wave length. Hence, the coefficient δl_0 can be set to zero. The resulting longitudinal displacement is caused only by the momentum variation. The correlation between longitudinal displacement and momentum variation is determined by the matrix element R_{56} of the transfer matrix with,

$$\delta l = \frac{\Delta p}{p} \cdot R_{56}. \tag{3.7}$$

The analytical formula of the matrix element R_{56} for a dispersion free path length is:

$$R_{56} = \frac{l}{\gamma^2}. \tag{3.8}$$

For a distance $l = 43.9\,m$ and a kinetic energy of $160\,MeV$ of the H^- ions Eq. 3.8 leads to:

$$R_{56} = \frac{43.9m}{1.171^2} = 32m. \tag{3.9}$$

With Eq. 3.7 this leads to a longitudinal displacement of $\delta l \approx 0.128m$ in the case of an energy change of $\Delta E = 1.2\,MeV$. For the calculation of the phase swing the RF-frequency f_{RF} and the relativistic velocity $\beta\,c$ are required, Eq. 3.10,

$$\Phi_{swing}[deg] = 360\,deg \frac{\delta l \cdot f_{RF}}{\beta c}. \tag{3.10}$$

For a cavity position of $43.9\,m$ Eq. 3.10 leads to a phase swing of $105\,deg$, which perfectly agrees with the calculated value using Eq. 3.4.
However, this formalism can also be used to compute the required phase swing including dispersive effects. The transfer matrix $R(43.9m)$ from the exit of Linac4 to the entrance of the debuncher cavity at $43.9\,m$ was determined using

the particle tracking code Path [22],

$$R(43.9m) = \tag{3.11}$$
$$\begin{pmatrix} 0.45411E+01 & 0.85946E+01 & 0.49308E-05 & -0.39869E-05 & 0.00000E+00 & 0.18258E+01 \\ -0.41537E-01 & 0.14160E+00 & 0.33498E-06 & -0.18025E-05 & 0.00000E+00 & 0.17726E+00 \\ 0.14359E-04 & 0.28618E-04 & 0.27780E+01 & -0.45538E+01 & 0.00000E+00 & -0.11150E-03 \\ 0.66027E-06 & 0.82369E-06 & -0.10238E-01 & 0.37676E+00 & 0.00000E+00 & -0.10949E-04 \\ -0.88081E+00 & -0.12650E+01 & 0.30583E-04 & -0.89025E-04 & 0.99998E+00 & 0.34082E+02 \\ 0.00000E+00 & 0.00000E+00 & 0.00000E+00 & 0.00000E+00 & 0.00000E+00 & 0.10000E+01 \end{pmatrix}.$$

Since this transfer matrix was obtained using a particle tracking code, several matrix elements, which are supposed to be zero by analytical calculations, are showing a numerical zero, e.g. $R_{13} = 0.49308E{-}05$. The transfer matrix element R_{56} is $R_{56} = 34.08\,m$. Thus, an additional path length $\delta(\delta l)$ of

$$\delta(\delta l) = \delta R_{56} \cdot \frac{\Delta p}{p} = (34.08\,m\ -\ 32\,m) \cdot 4.0 \cdot 10^{-3} = 8.32\,mm \tag{3.12}$$

is caused due to the dispersive effects. This path length discrepancy corresponds to an additional phase swing of $\delta\Phi_{swing} = 6.76\,deg$. This phase swing variation amounts to just 6 % the required phase swing and it can be compensated by e.g. an adjustment of the energy modulation or an adjustment of the cavity voltage.

The advantage of the last calculation method is the high precision of the determined phase swing. This method is rather complex and has to be re-performed in the case of changes of the transfer line optics to maintain the precision. In conclusion, for the estimation of the phase swing both methods are suitable and a final phase swing between 85 *deg* and 105 *deg* is expected.

RF-Power Needed

The RF-power needed is determined by the cavity voltage, the RF-phase swing and the beam current. In order to minimise the RF-power needed several scenarios were studied[5][44]. The most important scenarios are summarised in Tab.3.4.

Position $[m]$	Phase Swing $[deg]$	Voltage $[kV]$	RF-Power [kW] $I_{beam} = 0\,mA$	RF-Power [kW] $I_{beam} = 20\,mA$	RF-Power [kW] $I_{beam} = 40\,mA$	RF-Power [kW] $I_{beam} = 64\,mA$
35m	85	900	62.3	70.7	80.2	93.1
42m	105	680	43.9	51.8	60.7	73.0
42m	105	820	63.8	73.2	83.7	97.8
46m	112	700	50.0	58.6	68.3	81.4

Table 3.4: Debuncher Cavity Positions & RF-Power Need
In this table the RF-Power needed for different combinations of cavity positions and cavity voltages are listed. As the RF-power needed strongly depends on beam current, the list includes the RF-power consumption for different beam currents such the nominal beam current and the beam current of special probe beams with reduced intensity. A boundary condition for the choice of cavity position is that the maximum RF power is restricted below 100 kW. In the final line the RF-power requirement for the chosen cavity position is listed with a margin of the cavity voltage of 20 %.

[5]Thanks to R.Wegner for performing the RF-Power needed calculations.

For the calculation of the RF-power consumption the beam current is needed to estimate the beam loading of the cavity. The impact of four different beam currents were studied, $I_{beam} = 0\,mA$, $I_{beam} = 20\,mA$, $I_{beam} = 40\,mA$ and $I_{beam} = 64\,mA$. The case $I_{beam} = 0\,mA$ corresponds to the test of the debuncher cavity performance without beam.
In the old transfer line layout the debuncher cavity was located $35\,m$ downstream of the exit of Linac4. In this configuration a cavity voltage of $900\,kV$ and a phase swing of $85\,deg$ are required. This leads to a power consumption of approximately $93\,kW$ for the maximum beam current.
Based on the new transfer line layout the furthermost downstream position of the debuncher cavity is $46\,m$ leading to a phase swing of $112\,deg$. Due to the increased bunch length a lower cavity voltage of less than $650\,kV$ is required to meet the energy spread threshold of $\sigma_{energy} = 120\,keV$. For the calculation of the RF-power needed of this scenario a margin of the cavity voltage of 15 % was assumed. In comparison to the first scenario the RF-power consumption is considerably reduced. At this scenario a rms bunch length of approximately $26\,deg$ is obtained at the debuncher cavity. As a consequence an altered correlation between particle acceleration / deceleration and particle position will be caused at the head and tail distribution of the bunches.
In the final transfer line layout the debuncher cavity is located at $42\,m$. A phase swing of $105\,deg$ is needed. For the nominal beam a cavity voltage of $680\,kV$ is required. The maximum RF-power consumption is in the order of $73\,kW$. A margin of the cavity voltage of 20 % was requested leading to a maximum cavity voltage of $820\,kV$. The maximum RF-power consumption of this scenario is $98\,kW$.

3.3.4 Focusing Scheme at the Vertical Offset

Due to radiation protection issues the vertical level of Linac4 needed to be lowered by $2.5\,m$. Consequently, a vertical chicane was implemented in the transfer line layout to compensate this vertical offset [40]. In order to minimise a coupling between both transverse planes and to minimise the space charge impact on the vertical dispersion the chicane was design compact and achromatic. The implementation of the chicane in the transfer line layout was accomplished by re-positioning of several quadrupole doublets. In the updated layout two quadrupole doublets are located upstream and two quadrupole doublets are located downstream of the vertical chicane. These four quadrupole doublets are used to focus the beam into the chicane and to match the beam from the chicane to the downstream transfer line. At survey measurements in 2010 a potential conflict between this layout and an already existing elements was identified. Hence the beam dynamics of the vertical chicane was re-investigated to generate a feasible, alternative focusing strategy [45].

Vertical Chicane - Old Beam Optics

A compact and achromatic design of the chicane was chosen to compensate the vertical step of $2.5\,m$. The components of the chicane are two dipole magnets

and three quadrupole magnets, Fig. 3.16.

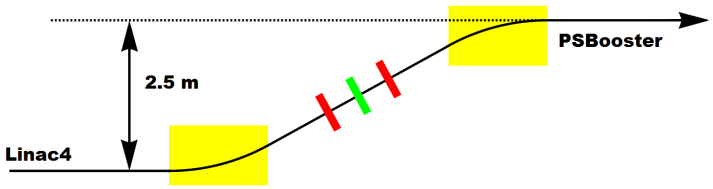

Figure 3.16: Vertical Chicane - Schematic
Between Linac4 and the PS-Booster a vertical offset of 2.5 *m has to be compensated by means of a vertical chicane. In this schematics the layout of the vertical chicane is illustrated. Its three quadrupoles are foreseen to close to dispersion bump and to ensure a low-loss beam transport.*

The dipole magnets are used to generate a beam deflection of 28.75 *deg* each. In between the dipole magnets the layout of the quadrupoles is optimised to close the vertical dispersion bump and providing a low-loss beam transport. The symmetry of the chicane in combination with the different bending directions allows to match a vanishing vertical dispersion by means of the two outer quadrupoles. The vertical dispersion vanishes in the centre of the chicane. Therefore, the impact of the middle quadrupole on the vertical dispersion is negligible. This quadrupole is used to focus the horizontal beam size and to control the horizontal dispersion. Due to this compact design high field gradients in the order of $g = 15\,\frac{T}{m}$ are required to close the dispersion bump.
In order to minimise the impact of the three chicane quadrupoles on the transverse beam sizes and on the horizontal dispersion the four quadrupoles upstream the chicane are used to reduce the transverse beam sizes as well as the horizontal dispersion along the chicane. In Fig. 3.17 the development of the transverse β-functions and the horizontal dispersion along the vertical chicane including the surrounding matching quadrupoles are shown.

The first quadrupole doublet is used to generate a different beam sensitivity in horizontal and vertical plane at the location of the second quadrupole doublet. The quadrupoles of the second doublet are powered in series causing identical field gradients with opposite orientation. Due to the different sensitivities of both transverse beam sizes both transverse β-functions are focused into the chicane.
The downstream quadrupole magnets are used to match the beam from the high phase advance lattice of the chicane to the low phase advance lattice of the downstream transfer line. While the first quadrupole is used to generate a small discrepancy between horizontal and vertical β-function, the remaining three quadrupoles are combined to a focusing structure similar to a quadrupole triplet. The sequence of the quadrupole polarity is determined by the control of the horizontal dispersion.

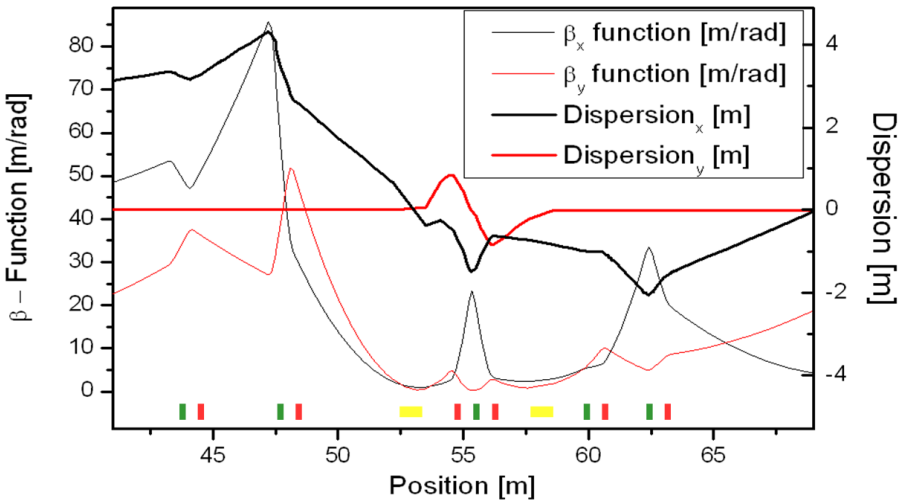

Figure 3.17: Beam Optics along the Vertical Chicane - Old Layout
In this diagram the development of the transverse β-functions and of the dispersion along the vertical chicane section is plotted. The two quadrupole doublets upstream of the vertical chicane are used to minimise the transverse beam sizes and the horizontal dispersion along the chicane leading to a low-loss beam transport through the chicane. Downstream of the chicane three of the four quadrupoles are used in a focusing configuration similar to a quadrupole triplet. In this configuration the beam is matched to the downstream transfer line optics within excellent control of the horizontal dispersion.

Vertical Chicane - New Beam Optics

In the new transfer line layout the four quadrupole doublets are replaced by two quadrupole triplets. The design of the vertical chicane is maintained. The beam optics is shown in Fig. 3.18.

To ensure a low-loss beam transport the transverse beam sizes and the horizontal dispersion are minimised along the vertical chicane. The optimisation of the beam optics is conducted by the adjustment of the quadrupole field gradients of the triplet quadrupoles and of four quadrupoles upstream of the debuncher cavity. In order to tune the transverse beam sizes independently from the horizontal dispersion the horizontal dispersion is minimised at the location of the quadrupole doublet upstream of the debuncher cavity.
Downstream the vertical chicane the quadrupole triplet is used to match the beam to the low phase advance lattice of the downstream transfer line. By the adjustment of the field gradients of the downstream quadrupole triplet the transverse β-functions are focused into the following bending magnet to minimise potential particle losses within excellent control of the horizontal dispersion.

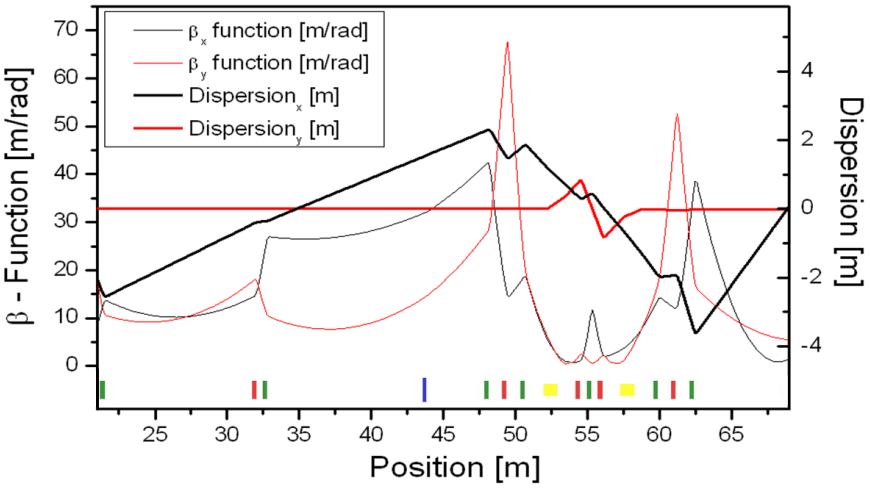

Figure 3.18: Beam Optics along the Vertical Chicane - New Layout
In this plot the development of the transverse β-functions and the development of the dispersion upstream and along the chicane is shown. To enhance the tunability of the beam optics along the chicane the horizontal dispersion was minimised at an upstream quadrupole doublet. This allows the optimisation of the beam sizes development along the chicane within a minimised impact on the development of the dispersion.

3.3.5 Performance Evaluation

The performance of lattice optics includes several aspects [46]. Major aspects for transfer line lattices are the preservation of beam quality, the stability of the optical solution in presence of alignment errors and field jitters and the tunability of the lattice optics to provide a high flexibility in the PS-Booster matching parameters.

Emittance Preservation

For the PS-Booster beam injection it is planned to apply longitudinal and transverse phase space painting. For the transverse phase space painting the preservation of the transverse emittance is in particular important. In order to enhance the transverse emittance preservation the layout of the first transfer line section was re-design, section 3.3.2. The space-charge-dispersion bumps are closed leading to a minimisation of the horizontal emittance.
For the longitudinal phase space painting an upper limit of the energy spread of $\sigma_E = 120\,keV$ at an energy modulation of $\Delta E = \pm 1.2\,MeV$ is defined. Due to the intense space charge effects at the first transfer line section the energy spread increased above $\sigma_E = 300\,keV$. To reduce the energy spread a debuncher cavity was implemented in the transfer line layout. As a result of the optimisation of the debuncher cavity performance a reduction of the longitudinal emittance is obtained. In Fig. 3.19 the developments of the transverse and longitudinal emittances of the old and new transfer line optics are plotted.

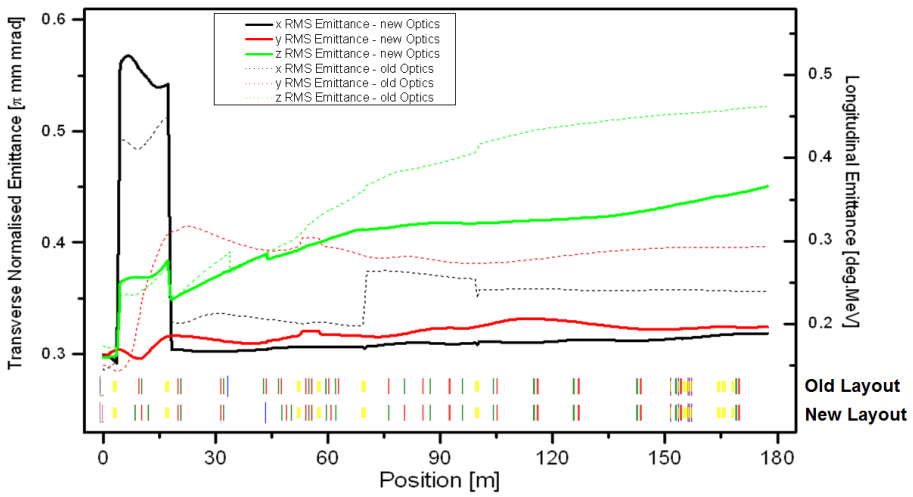

Figure 3.19: Emittance Preservation along the Transfer Line

In this figure the development of the transverse and longitudinal emittances along the transfer line are plotted. The steps in the development of the emittances are calculation artifacts of the simulation program.

Due to the modifications presented in this thesis the transverse emittance growth could be limited below 10 % and the longitudinal emittance growth is reduced by 30 %.

Stability Test

Alignment errors, field jitters and other influences such as ground motion are causing disturbances of the optical solution. In order to ensure a stable beam transport a low sensitivity of the beam optics to such disturbances has to be established. The sensitivity is determined by the lattice layout and by the beam optics itself. To examine the sensitivity of the transfer line error study runs were performed using the code Path. At these runs the transfer line optics is simulated including feasible misalignment errors and field jitters, which are randomly distributed, Tab. 3.5.

Component	**Misalignment**	**Field Jitter**
Quadrupole	$\sigma_{hor.} = 0.2\,mm$ $\sigma_{ver.} = 0.2\,mm$ $\sigma_{rot.} = 0.1\,mrad$	$\sigma_{jitter} = 0.5$ %
Dipole	-	$\sigma_{jitter} = 0.01$ %

Table 3.5: Summary of examined Error Scenarios

The field errors are randomly applied to the beam optics elements. Its distribution is Gaussian with an error range of three sigma.

The stability test is separated into sequences to identify the individual effects of

each error scenario. In the first scenario the impact of quadrupole misalignments and quadrupole field jitter on the transfer line beam dynamics is investigated. Based on the simulation results the steering strategy of the transfer line is adjusted and its performance evaluated. In the second step the stability of the beam transport in presence of field jitters of the dipole magnets is examined. Here, the limits of the field jitters within stable beam transport are determined, which are used to define the interlock thresholds of the dipole magnets. In the third step the stability of the optical solution in presence of quadrupole alignment errors and field jitters of the quadrupole magnets and dipole magnets is examined.

Quadrupole Misalignment and Field Jitter
In this scenario the impact of the quadrupole misalignments and field jitters on the beam transport are examined. For this purpose transverse horizontal and vertical displacements ($\sigma_{hor.}$ and $\sigma_{ver.}$), rotation of the quadrupole ($\sigma_{rot.}$) and quadrupole field jitter of 0.5 % are assumed. More than 1000 different error combinations are simulated for each of the two transfer line optics.
An average transmission of 98.3 % (old optics) and 99.8 % (new optics) is obtained. Due to the changes of the transfer line optics the average potential of particle losses is reduced by a factor of 10. In Fig. 3.20 the numbers of runs with beam transmissions below 95 % are listed.

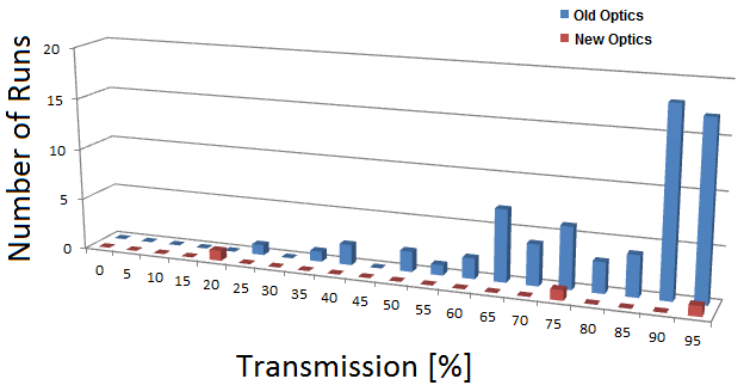

Figure 3.20: Statistics of the Beam Transmission
In this diagram the numbers of error combinations with beam transmission below 95 % *are listed. For the two transfer line optics more than* 1000 *error combinations each were simulated. A significantly higher performance of the new transfer line optics is observed.*

A transmission below 95 % is observed at only 6.8 % of the simulated error combinations in the case of the old transfer line optics. At the new transfer line optics only 3 combinations are detected, which corresponds to 0.25 % of the simulated combinations. The locations of the particle losses are illustrated in Fig. 3.21.

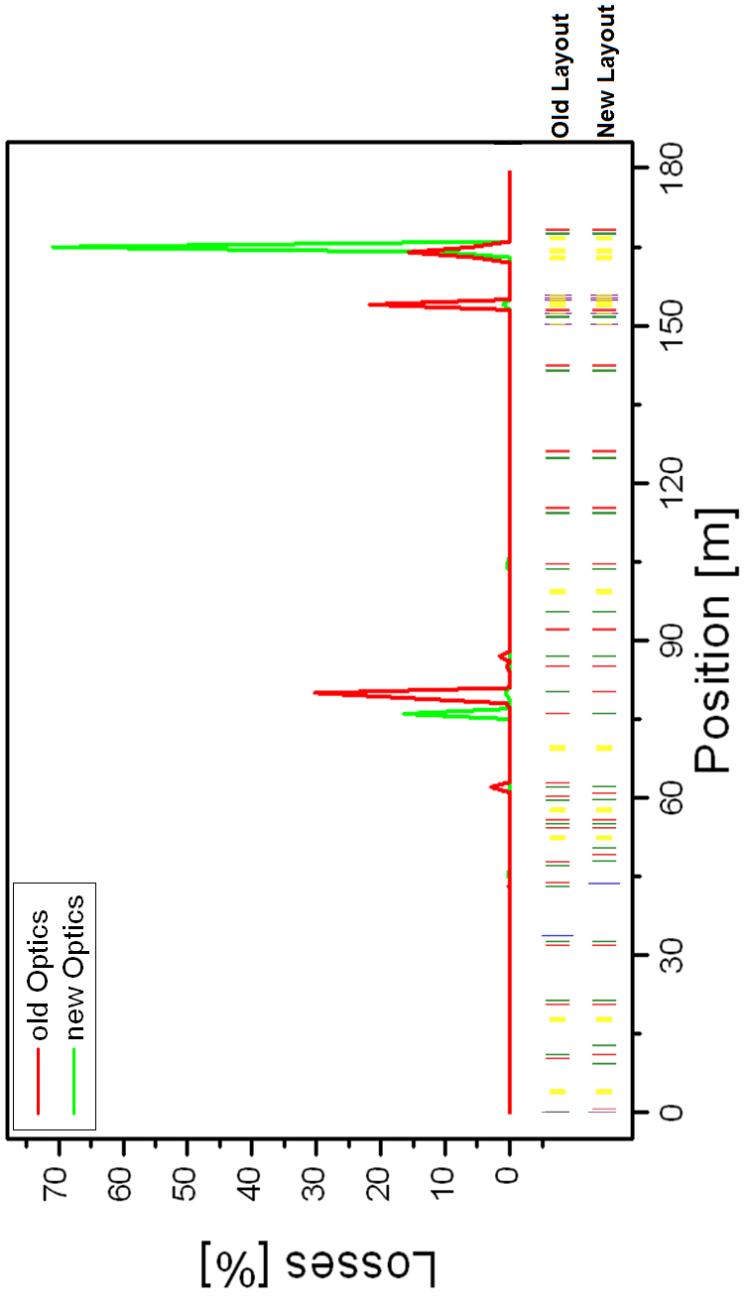

Figure 3.21: Locations of Particle Losses

In this diagram the locations of the lost particles are illustrated. Thereby, the relative losses, i.e. losses divided by the total amount of losses, are displayed. The major losses are concentrated at the quadrupole doublet downstream of the dipole BHZ20 (at 75 m), at which the new transfer line joins the existing accelerator structure, and near the injection region of the PS-Booster, which is characterised by a reduced aperture.

The evaluation of the loss locations of the old optics is indicating several "hot zones", where higher radioactive loads are expected. These locations are the quadrupole doublets downstream of the vertical chicane ($s = 60\,m$), the first quadrupoles downstream the bending magnet BHZ20 ($s = 75\,m$) as well as the distributor section near the PS-Booster injection point ($s = 155\,m$ and $s = 175\,m$). In the new transfer line optics a concentration of the losses is observed at the first quadrupole downstream of dipole magnet BHZ20 ($s = 80\,m$) and at the septum magnet ($s = 175\,m$).

Dipole Field Jitter
Due to jitter of the dipole fields variations of the orbit are caused. In the case of the expected dipole jitter of 0.01 % no significant changes of the beam transmission are simulated at both lattice optics.
For the determination of the interlock thresholds of the dipole magnets the range of stable beam transport needs to be identified. Therefore, the magnetic field of the dipole magnets has been varied by 9 %. This corresponds to a beam deflection in the range of 18 $mrad$ at the horizontal dipole magnets and 15 $mrad$ at the vertical dipole magnets. 1200 different error combinations are simulated for each of the transfer line optics. The simulation results are showing a hard edge separation between scenarios with good beam transmission near 100 % and scenarios with beam transmission close to 0 %, Fig. 3.22.

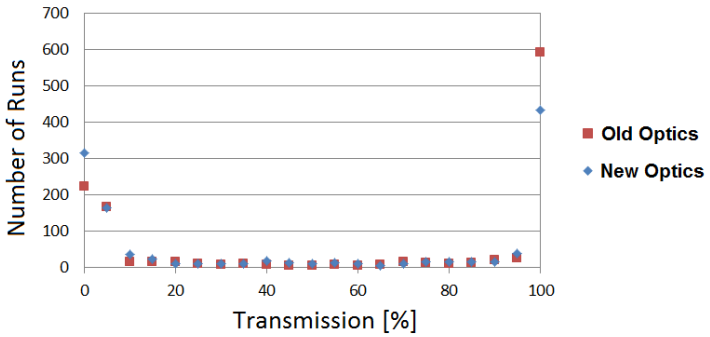

Figure 3.22: Statistics of the Beam Transmission
In this diagram statistics of the beam transmission for the dipole error tests are plotted. A clear separation between scenarios with excellent transmission and with vanishing transmission is observed.

In Fig. 3.23 the simulated transmission depending on the deflection angle for the two transfer line optics are plotted.

A special feature of the transmission plots is the rectangular shape. This shape indicates that the field jitter impact of the horizontal and vertical bending magnets on the beam transmission are independent from each other. Therefore, the limits of acceptable field variation in horizontal dipoles and vertical dipoles are separable. As a limit for horizontal dipole jitters a maximum angle variation of

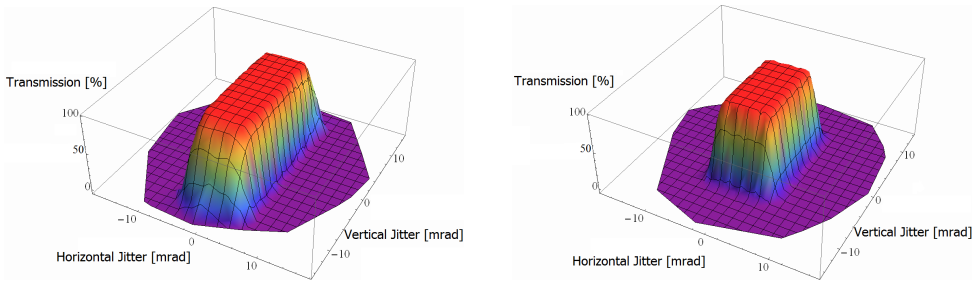

(1) Dipole Jitter - Old Optics (2) Dipole Jitter -New Optics

Figure 3.23: Transmission in Presence of Dipole Jitter
In these diagrams the dependence between transmission and field jitter of the horizontal and vertical dipoles is plotted. Based on the detected shape of the parameter space characterised by an excellent beam transmission it is concluded that the impact of the horizontal and vertical field variation on the beam transmission are decoupled.

$\pm 3\,mrad$ was detected at both lattice optics, which corresponds to field variation of 0.5 %. The limits of the vertical dipole field variation are 1.5 % (old optics) and 1.1 % (new optics).
To define interlock thresholds the Linac4 operation mode has to be taken into account. Based on Eq. 3.13 a change of the dipole field strength can also be interpreted as a change of the design energy or particle momentum,

$$B \cdot \varrho = \frac{p}{q}; \tag{3.13}$$

$$\frac{\Delta B}{B} = \frac{\Delta p}{p}, \tag{3.14}$$

with B magnetic flux density, ϱ curvature radius, p particle momentum and q particle charge. Since at some operation modes of Linac4 also a variation of the average particle energy along the bunch train is planned, the variation of the particle momentum needs to be considered. The energy modulation of $\Delta E = \pm 1.2\,MeV$ corresponds to a relative momentum change of $\left(\frac{\Delta p}{p}\right)_{painting} = 0.4\,\%$. Hence, a maximum field jitter range of $\left(\frac{\Delta B}{B}\right)_{hor.} \sim 10^{-3}$ at the horizontal dipoles and of $\left(\frac{\Delta B}{B}\right)_{ver.} \sim 10^{-2}$ at the vertical dipoles is determined. In the case of a lower energy modulation along the bunch train a re-definition of the interlock thresholds towards larger field variations is possible.

Dipole Field Jitter and Quadrupole Field Errors
For the studies of combined dipole and quadrupole errors the parameters listed in Tab. 3.5 are used. At the individual studies of the error parameters a minor impact of the dipole jitter on the beam transmission was observed. The reduction of the average beam transmission caused by the dipole jitters is in the order of 10^{-3} %. These particle losses are mainly concentrated in the new

transfer line part, Fig. 3.24.

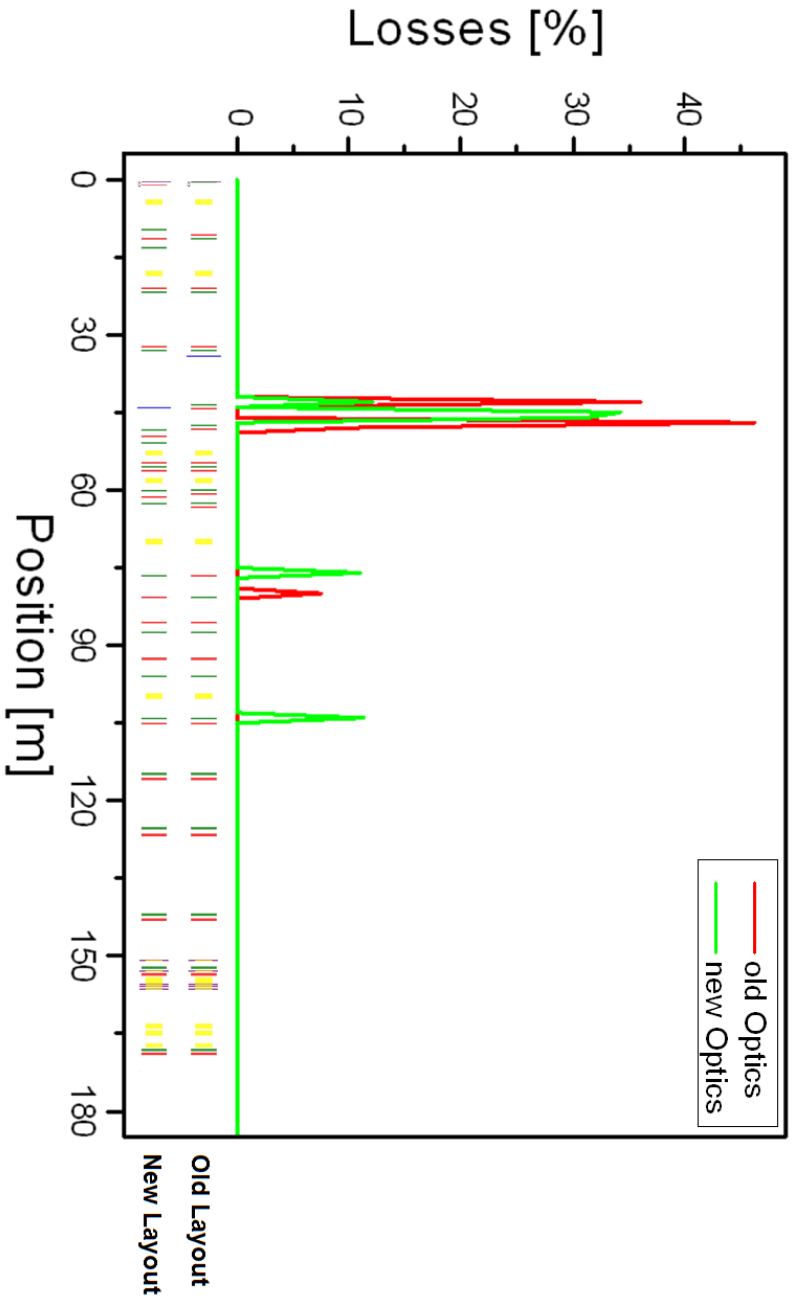

Figure 3.24: Dipole Jitter - Map of Losses

In this diagram the distributions of the relative particle losses along the transfer line in presence of dipole jitters are plotted. At the specified jitter level of $\frac{\Delta B}{B} = 10^{-4}\,\%$ *minor losses are observed. These losses are mainly concentrated in the first part of the transfer line between* $40\,m$ *and* $50\,m$ *downstream of the exit of Linac4.*

At the quadrupole error studies the particle losses are focused at the quadrupoles at 75 m and at the distributor section, Fig. 3.21. The combination of dipole and quadrupole magnet errors leads to an increase of the average particle losses, Tab. 3.6.

Error Scenario Beam Optics	**Dipole Jitter**	**Quadrupole Errors**	**Combined Errors**
Optics 2009	$3 \cdot 10^{-3}$ %	1.65%	1.98%
Optics 2011	$5 \cdot 10^{-4}$ %	0.15%	0.19%

Table 3.6: Average Particle Losses - Error Scenario
In this table the average particle losses per simulated error combination are listed. The combination of the dipole jitter and the quadrupole errors caused an amplification of the particle losses of approximately 15 %. *The statistic of the different error combinations shows further that the new transfer line optics leads to a reduction of the potential particle losses of* 90 %.

In Fig. 3.25 the statistics of the beam transmission are shown.

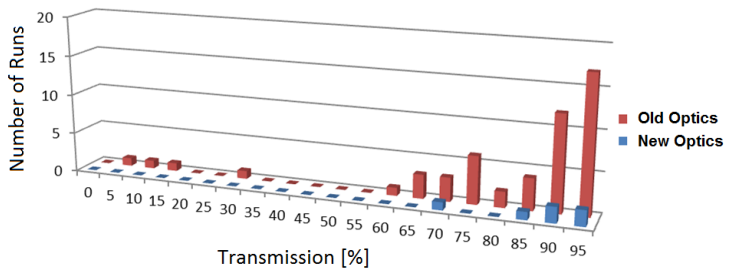

Figure 3.25: Statistics - Beam Transmission
In this statistics the numbers of simulated error combinations are listed with beam transmissions below 95 %. *In the case of the old transfer line optics* 9 % *of the simulated combinations are characterised by transmissions below* 95 %. *For the new transfer line optics only six combinations with a beam transmission below* 95 % *are detected, which corresponds to* 1 % *of the total number of tested error combinations.*

The average transmission increased from 98.0% (old optics) to 99.8% (new optics).
The losses are also concentrated at the first quadrupoles at approximately 75 m and at the distributor section, Fig. 3.26.

A comparison of the relative losses of the quadrupole error studies with the losses of the combined error scenarios shows that the particle losses are partly shifted upstream to the quadrupoles at 75 m. The detailed analysis of the losses verifies that the losses at the distributor section are almost preserved. The increase of losses near the vertical chicane corresponds well with the increase of

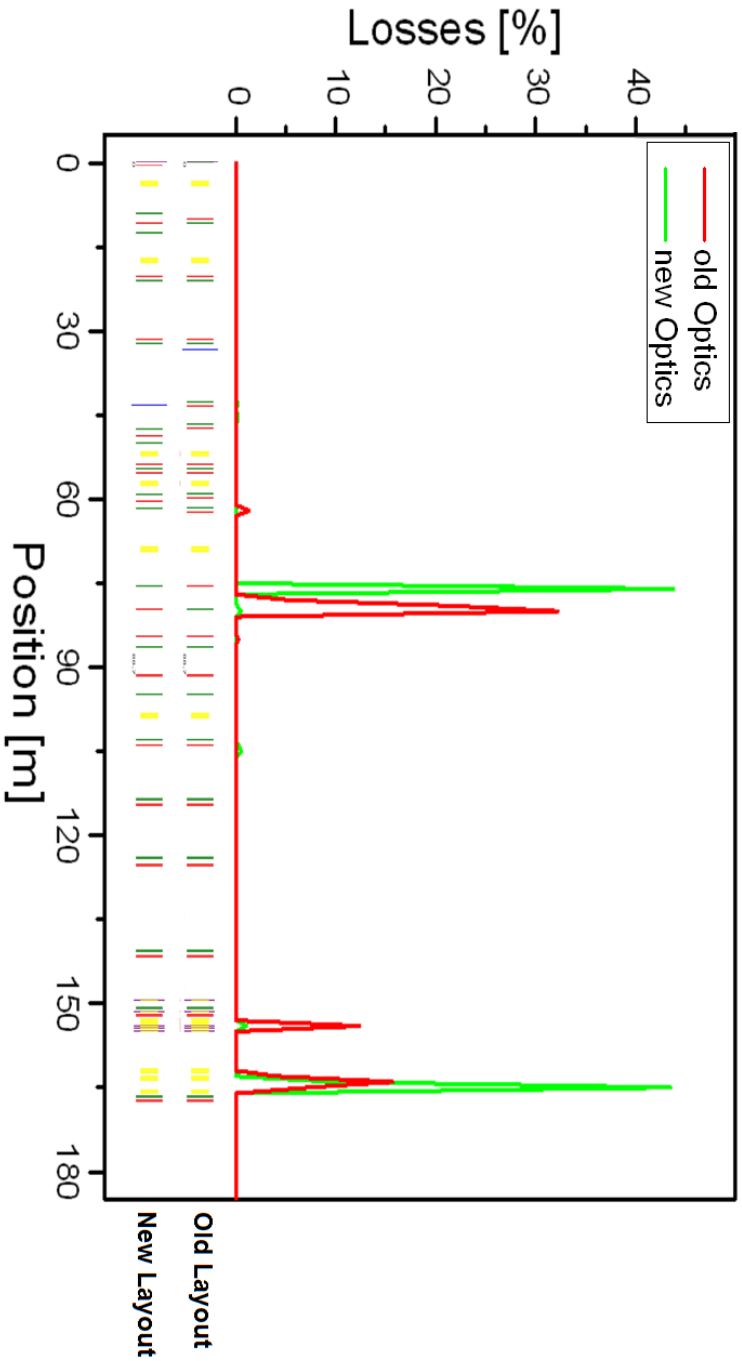

Figure 3.26: Locations of Particle Losses - Combined Errors

In this diagram the locations of the particle losses caused by the impact of dipole field jitter, quadrupole field jitter and quadrupole alignment errors are plotted. The losses are mainly concentrated at the first quadrupoles of the re-used transfer line section from Linac2 to the PS-Booster and near the PS-Booster injection point.

the total losses at both optics.
In operation the quadrupole alignment errors will be partly compensated by means of steerer magnets. Consequently, a loss less beam transmission within reasonable beam quality preservation is expected.

Tunability

Several different sets of beam parameters are defined for PS-Booster injection, section 3.2.2 and [45]. In dependence of the foreseen use of the beam different filling schemes will be used to optimise the phase space distributions. Therefore, the flexibility to match the beam in a wide phase space range is another important aspect of the transfer line performance. In order to investigate the tunability several hundred test runs were conducted with randomly varied field gradients of several transfer line quadrupoles. In Fig. 3.27 the theoretical range of matching parameters is plotted.

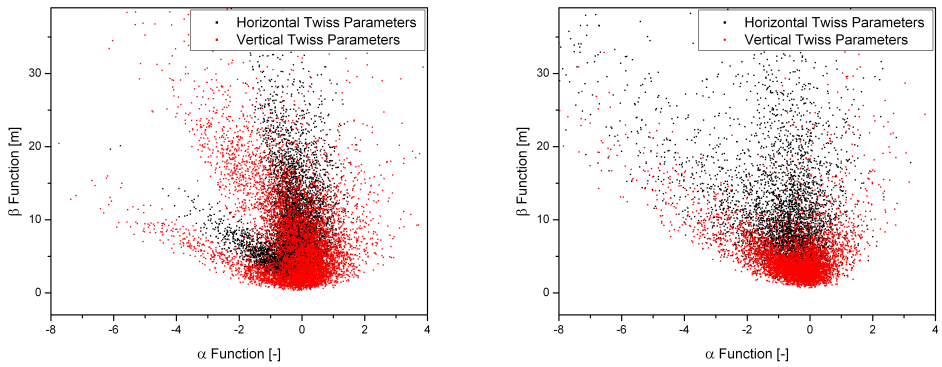

(1) Dispersion $D_x \neq 0$ (2) Dispersion $D_x = 0$

Figure 3.27: Twiss Parameters - Matching Range
At these plots the variation range of the injection Twiss parameters of the transfer line of optics 2011 is shown. Here, settings with transfer line transmissions below 99.9% *are excluded.*

Results from runs with a beam transmission below 99.9% are excluded from these plots. Due to two aperture bottlenecks close to the injection point the tuning range in horizontal plane is larger than in vertical plane. In addition to the variation of the transverse Twiss parameters the tunability of the horizontal dispersion is required. For the longitudinal phase space painting an energy modulation of $\Delta E = \pm 1.2\,MeV$ is planned. This energy modulation leads to transverse beam movements at dispersive sections. At the injection point the PS-Booster optics is characterised by a horizontal dispersion of $D_x = -1.4\,m$. In the case of a dispersion matched PS-Booster injection a transverse beam movements due to the energy modulation will be induced. This leads to a coupling of the transverse and longitudinal phase space painting schemes. In order to decouple the transverse phase space painting scheme from the energy modula-

tion the PS-Booster injection with a vanishing horizontal dispersion are studied. Several additional scenarios with reduced dispersion mismatch are under investigation, at which a tunability of the horizontal dispersion has to be ensured. In Fig. 3.28 the detected range of dispersion variation is plotted.

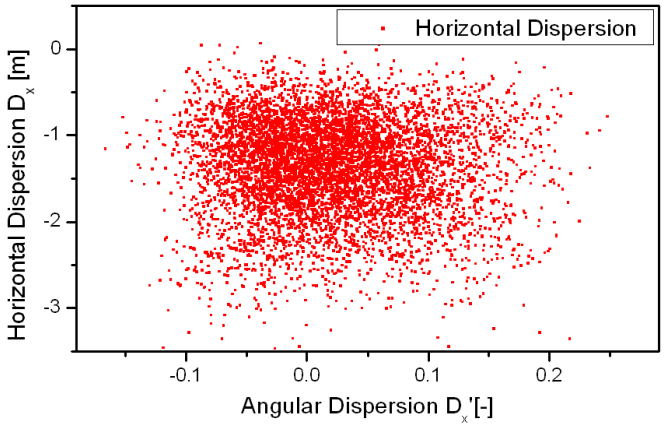

Figure 3.28: Dispersion Tune Range
In this plot the variation range of the horizontal dispersion D_x and horizontal angular dispersion D'_x is shown. The variation range of the horizontal dispersion is between $D_x = 0\,m$ and $D_x = -2.5\,m$. A further extension of the variation range can be accomplished by the use of different transfer line optics.

It can be concluded that a variation of the PS-Booster injection parameters far beyond the defined matching sets can be accomplished within reasonable beam transmission.

3.3.6 PS-Booster Matching

For the PS-Booster injection several Twiss parameter matching sets are defined. By specified Twiss parameter mismatch a variation of the transverse phase space filling of the PS-Booster buckets is intended to optimise the phase space distribution to the later purpose of the beam.
In addition to the variation of the Twiss parameters different horizontal dispersion values, $D_x = -1.4\,m$ and $D_x = 0\,m$, were specified. The matching strategies of the two dispersion matchings differ.

Dispersion Zero - Matching Procedure

In the case of PS-Booster injection with vanishing horizontal dispersion it is required to match the horizontal dispersion to zero with the last horizontal bending magnet, i.e. bending magnet BHZ30 at $100\,m$. In order to maintain the transverse emittance the beam optics of the transfer line section from the dipole BHZ20 at $70\,m$ to dipole BHZ30 has to be designed almost achromatic.

The beam sizes and the horizontal dispersion need to be minimised at the entrance of the bending magnet BHZ20 to reduce the potential of particle losses. The remaining quadrupoles downstream of the magnet BHZ30 are used to provide a low loss beam transport within Twiss parameter matching. In Fig. 3.29 the development of the dispersions and β-functions along the transfer line is plotted.

Dispersion $D_x = -1.4m$ - Matching Procedure

In the case of dispersion matched injection the transfer line upstream of bending magnet BHZ30 at $100\,m$ is optimised for maximum performance, i.e. minimum potential of particle losses within maximised transverse emittance preservation. Since the horizontal, space-charge-dispersion bump, section 1.2.1, was closed at the second horizontal dipole magnet at $18\,m$, it is required to design the transfer line section between the dipole magnets BHZ20 and BHZ30 achromatic. Downstream of magnet BHZ30 six quadrupole doublets are used to match the horizontal dispersion and transverse Twiss parameters. For this matching the main aperture limitations near the PS-Booster injection point have to be considered to minimise potential particle losses. As any energy modulation leads to a transverse beam movement, a minimisation of the horizontal dispersion at these aperture constraints needs to be accomplished. In the new transfer line optics the two quadrupoles downstream the distributor section are mainly used to adjust the intended horizontal dispersion. As simultaneously the transverse beam sizes have to be minimised at the two aperture constraints near the injection point, significantly higher β-functions upstream of the distributor section are required. To enhance the transfer line optics performance, the horizontal dispersion is minimised at the quadrupole doublet at $115\,m$. In this configuration the dispersion is minimised at four quadrupoles causing a minor sensitivity of the dispersion development on the settings of these quadrupoles. This leads to an enhancement of the tunability of the beam sizes within minimised impact on the development of the dispersion. A representative optics is shown in Fig. 3.30.

3.4 Diagnostics

Fundamental for the operation of each accelerator is to monitor its performance. For this purpose the use of special diagnostic lines are foreseen, which are located at the exit of Linac4 and directly upstream of the PS-Booster injection. To ensure a low-loss beam transfer within maximised preservation of the transverse beam emittance additional diagnostics elements such as Beam Loss Monitors, Beam Current Transformer and Beam Position Monitors are implemented in the transfer line layout. Their proposed positions are based on the beam dynamics of the transfer line and on the results of the error studies presented in section 3.3.5. In the framework of this thesis a proposal of the positioning of the diagnostics elements as well as a steering strategy for the new transfer line optics

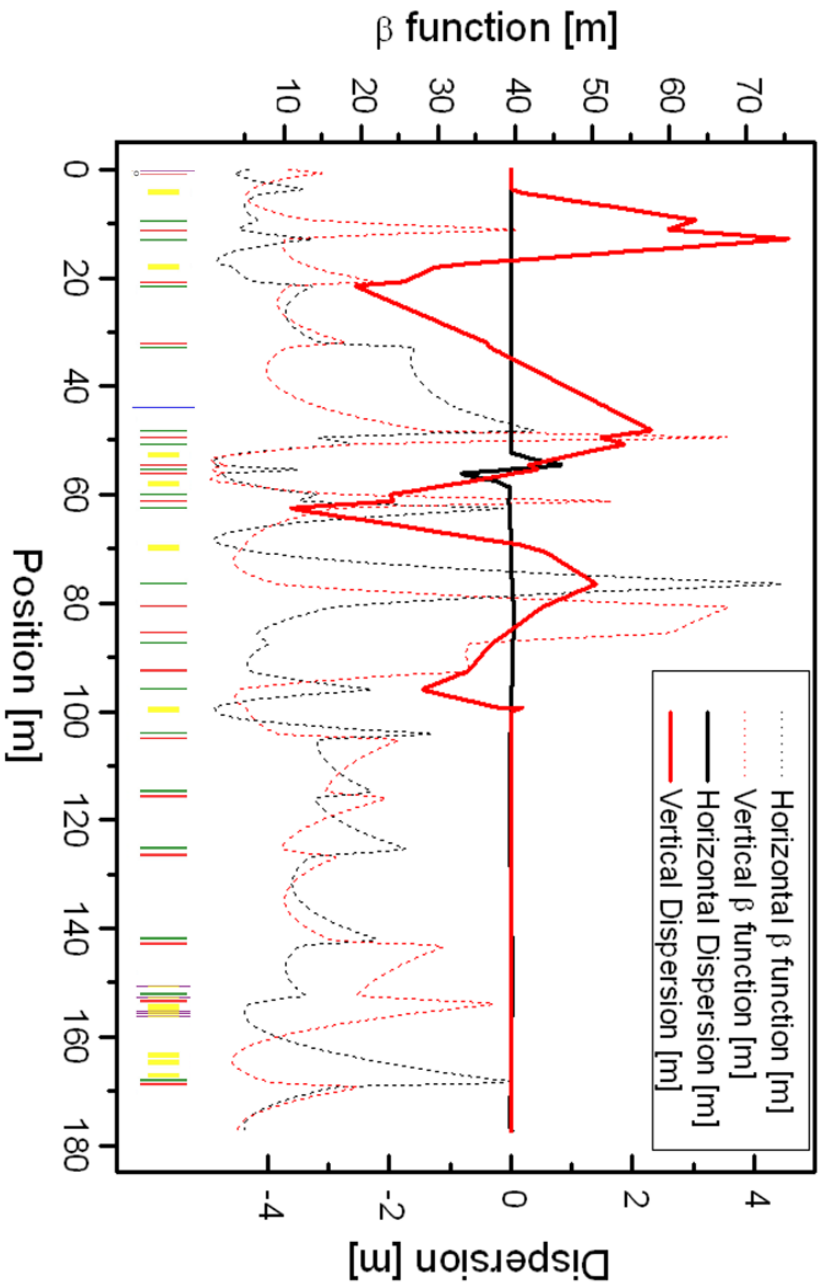

Figure 3.29: Dispersions and β-functions along the Transfer Line - Dispersion Zero Matched

In this plot the developments of the dispersions and transverse β-functions along the transfer line are shown. Downstream of dipole BHZ30, where a vanishing horizontal dispersion is matched, the quadrupole doublet structure is used to match the injection Twiss parameters.

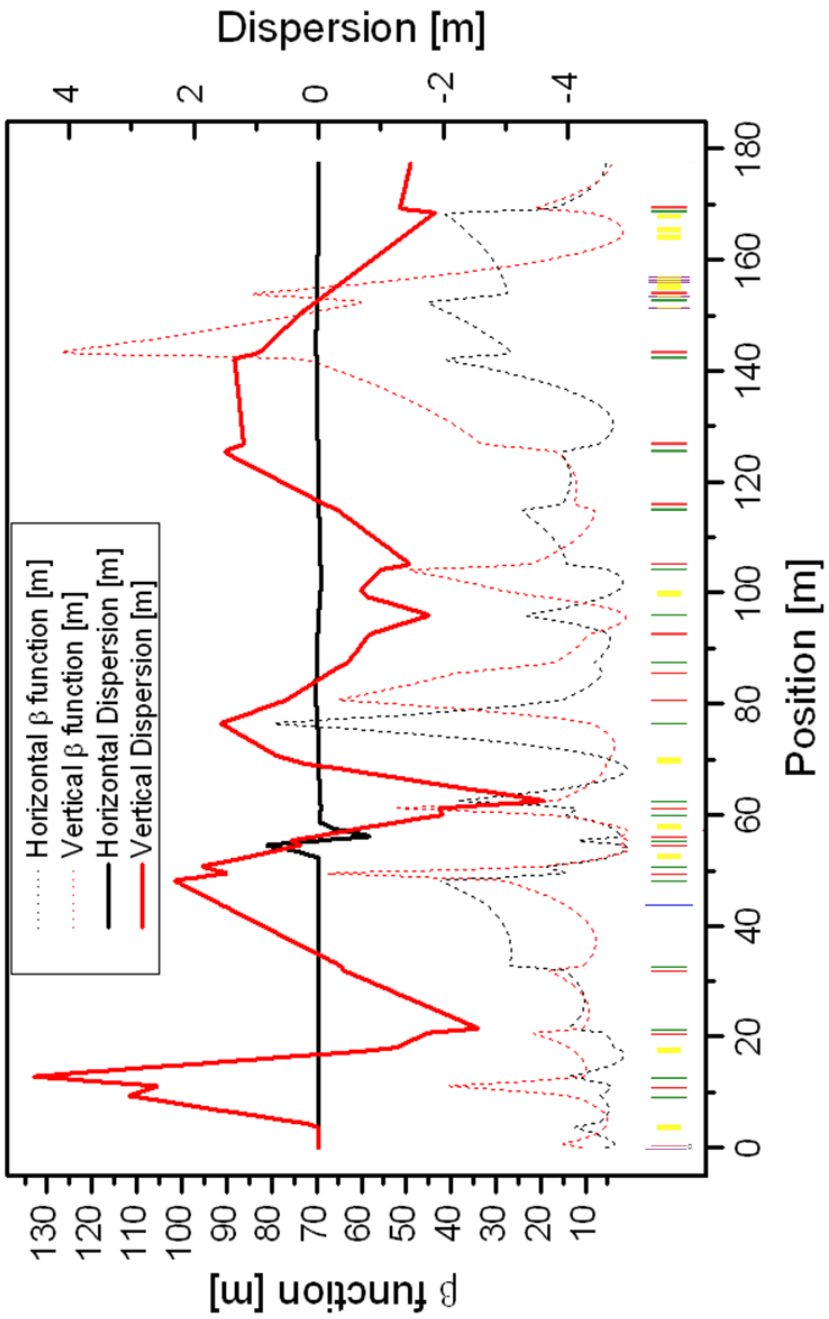

Figure 3.30: Dispersions and β-functions along the Transfer Line - Dispersion-1.4m Matched

In this plot the development of the dispersions and transverse β-functions along the transfer line are shown. In order to ensure a low-loss beam transport along the main aperture bottlenecks close to the PS-Booster injection within PS-Booster matching high β-functions upstream of the distributor section are required.

were developed. The developed strategy is mainly based on the measurement of the beam current and the transverse beam position upstream and downstream of transfer line sections with significantly increased potential of particle losses such as the quadrupole triplet in between the first two dipole magnets and the vertical chicane, at which a mismatched beam optics will lead to high particle losses.
In order to optimise the preservation of the transverse emittance and to ensure a correct PS-Booster matching measurements at the three diagnostics lines, L4Z, LBE and LBS, are essential, Fig. 3.31.

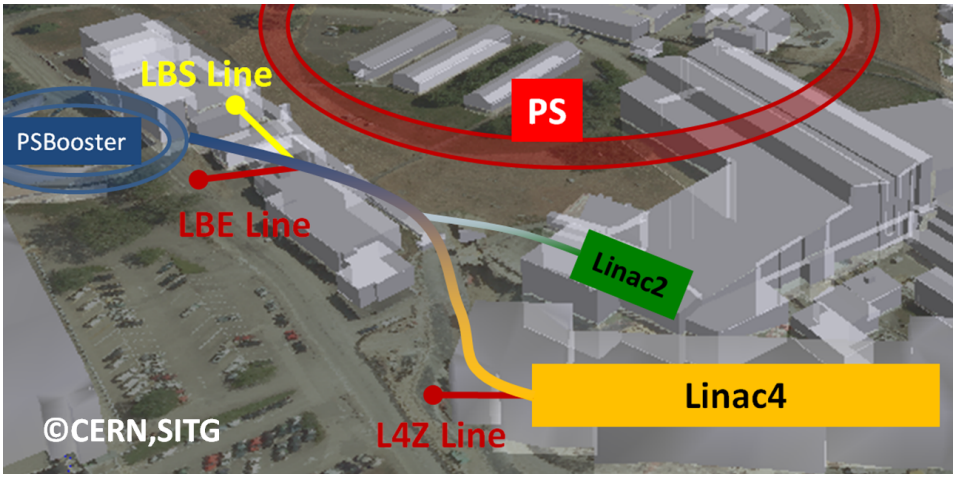

Figure 3.31: Locations of the Diagnostic Lines
In this scheme the locations of the diagnostics lines L4Z, LBE and LBS are shown. At the exit of Linac4 the measurement of the transverse emittances will be accomplished using the L4Z diagnostics line. Directly upstream of the PS-Booster injection two diagnostic lines for the measurement of the transverse emittances, LBE line, and for the measurement of the energy spread, LBS line, were installed. These two diagnostic lines are currently used for the investigation of the beam parameters of the Linac2 bunches.

The diagnostics lines L4Z and LBE will be used to study the transverse emittances at the exit of Linac4 and at the end of the transfer line. The measurement of the beam energy spread will be accomplished using the LBS line. In order to use the diagnostic lines LBE and LBS for the Linac4 operation major changes of their current working principle have to be conducted. In the following sections the new working principles and layout proposals of the three diagnostics lines are discussed.

3.4.1 Transverse Emittance Measurements

The measurement procedure of the transverse emittance at the L4Z line and LBE line is based on the Three-Monitor-Method [47].
At the Three-Monitor-Method the transverse emittance and transverse Twiss

parameters are determined by the measurement of the transverse beam size at a minimum of three different positions and the knowledge of the beam transformation between the measurement points. In order to reduce the complexity of the measurement procedure no optics elements will be placed in between the monitors. Hence, the beam transformation between the monitors is completely characterised by their distances. In Fig. 3.32 a scheme of the layout of the L4Z line is presented.

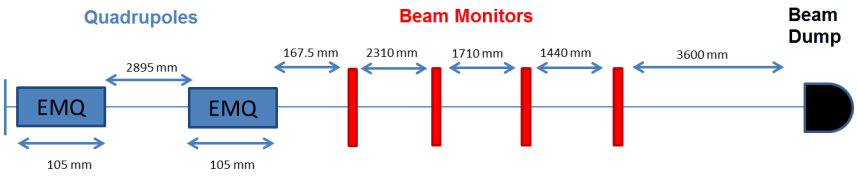

Figure 3.32: Schematical Layout of the L4Z Line
At the L4Z line two quadrupole magnets (blue) and four beam size monitors (red) will be used to measure the transverse emittances. It is foreseen to use the Three-Monitor-Method in combination with the quadrupole scan method [47]. For the emittance measurement at the LBE line the use of a similar layout is under investigation [48].

The transverse Twiss parameters, transverse emittance and the measured beam sizes are correlated by Eq. 1.43 or rather by:

$$\sigma_1^2 \quad = \quad R_{11}^2\,\beta_0 \cdot \varepsilon - 2\,R_{11}\,R_{12}\,\alpha_0 \cdot \varepsilon + R_{12}^2\,\gamma_0 \cdot \varepsilon \tag{3.15}$$

At the L4Z line it is intended to combine the Three-Monitor-Method with the Quadrupole-Scan-Method [47], at which the variation of a quadrupole field gradient is used to determine the transverse emittance and Twiss parameters.
Due to intense space charge effects at the exit of Linac4 the transformation matrix elements R_{ij} are significantly altered by the space charge defocusing. In order to consider the space charge defocusing at the measurement procedure and to mitigate its impact on the measurement results the planned emittance measurements were simulated with varying beam parameters. For the determination of the transverse emittance and Twiss parameters the measurement results will be benchmarked with the simulation results [49][48].

3.4.2 Energy Measurements

In the context of this thesis a new LBS line layout has been developed. The LBS line is a spectrometer line used to measure the energy spread of particle beams. For the measurement of the energy spread as well as for the measurement of energy variations the generation of dispersion is essential. Due to the dispersion particles and particle ensembles characterised by a momentum deviation are

transversely displaced:

$$\delta y \quad = \quad \frac{\Delta p}{p} \cdot D_y \ . \tag{3.16}$$

The transverse displacement is directly proportional to the variation of the momentum Δp. In the case of particle ensembles characterised by a momentum spread $\frac{\Delta p}{p}$ the dispersion leads to an increase of the transverse beam size:

$$\sigma_y \quad = \quad \sqrt{\beta_y \varepsilon_y + \left(\frac{\Delta p}{p} \cdot D_y\right)^2} \ . \tag{3.17}$$

Design - Layout

In the existing LBS line a combination of slit, dipole magnet and SEM-Grid is used, Fig. 3.33.

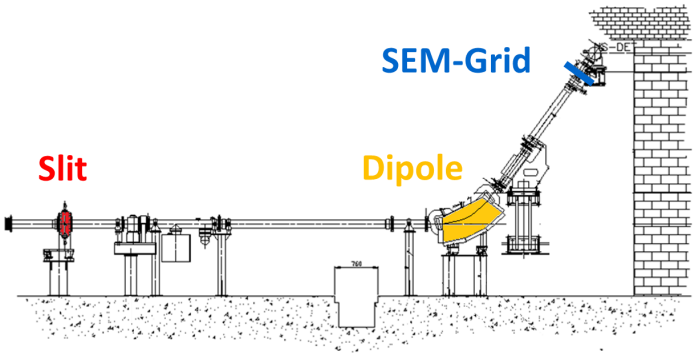

Figure 3.33: Current LBS-Line Layout

The LBS line is composed of an ensemble of slit, dipole magnet and SEM-Grid. The slit is used to collimate the transverse phase space of the particle ensembles. A dipole magnet installed downstream of the slit is used to generate a vertical dispersion of $D_y = 3\,m$ at the SEM-Grid.

The slit is used to reduce of the vertical emittance to enhance the resolution of the spectrometer line, Eq. 3.17. Due to the higher kinetic energy of the Linac4 particles the use of a slit needs to be avoided.
At a similar layout of the LBS line without the use of a slit the dispersion has to be varied from $D_y = 1\,m$ to $D_y = 10\,m$ to provide the required resolution for the investigation of the Linac4 energy regimes. To control the vertical dispersion the installation of a quadrupole magnet downstream of the spectrometer dipole is foreseen. In order to maintain the position of SEM-Grid and beam dump the position of the spectrometer dipole is shifted upstream. The layout of the new LBS line proposal is shown in Fig. 3.34.

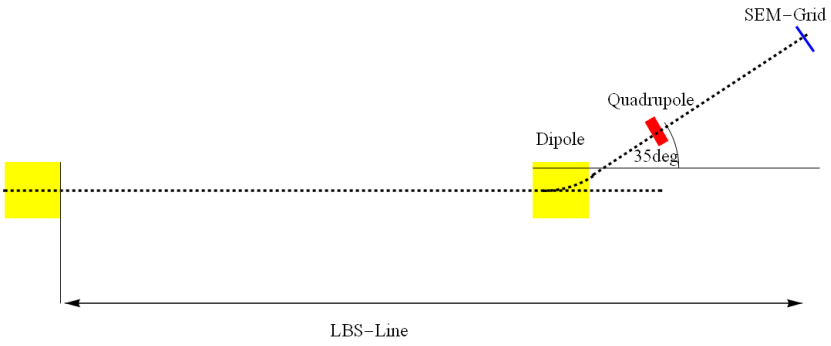

Figure 3.34: New LBS Line Layout
A Sbend dipole magnet is used to generate the vertical dispersion at the SEM-Grid. By means of the quadrupole setting the vertical dispersion will be controlled to optimised the measurement resolution.

The operation of Linac4 contains three different energy regimes, which have to be controlled using the LBS-Line. In the advanced PS-Booster injection scheme longitudinal phase-space-painting is foreseen, which requires an energy modulation of e.g. $\Delta E = \pm 1.2\,MeV$ along the bunch trains.
In first phase of Linac4 operation an PS-Booster injection without longitudinal phase space painting is planned. Here, an upper limit of the energy spread of the Linac4 bunches of $\sigma_{energy} = 450\,keV$ at the PS-Booster injection point is defined leading to an energy spread limit of $\sigma_{energy} = 350\,keV$ at the entrance of the LBS-line. This corresponds to the relative momentum spread of Linac2 of $\frac{\Delta p}{p} \approx 0.1\%$. In the case of optimised performance of the debuncher cavity the energy spread can be significantly reduced and an energy spread of $\sigma_{energy} = 90\,keV$ at the entrance of the LBS-line is expected. To optimise the measurement resolution for each energy regime several optical solutions of the LBS-line beam dynamics were calculated.

Energy Swing

The energy modulation of $\Delta E = \pm 1.2\,MeV$ corresponds to a relative momentum modulation of $\frac{\Delta p}{p} = \pm 0.4\,\%$. For the measurement of this momentum modulation at the LBS line the vertical bunch movement needs to be restricted to a range of approximately $\delta_y = \pm 5\,mm$ to optimise the measurement resolution. This determines a vertical dispersion of $D_y = 1.25\,m$ at the SEM Grid. A special beam optics to minimise the vertical beam size at the SEM-Grid position was computed.
In Fig. 3.35 the beam optics for investigation of the energy modulation from the exit of the bending magnet BHZ30 to the LBS-line SEM-Grid is shown.

In vertical plane the beam is focused using the weak focusing of the dipole magnet (Sbend) and the strong focusing of the quadrupole. Therefore, the beam

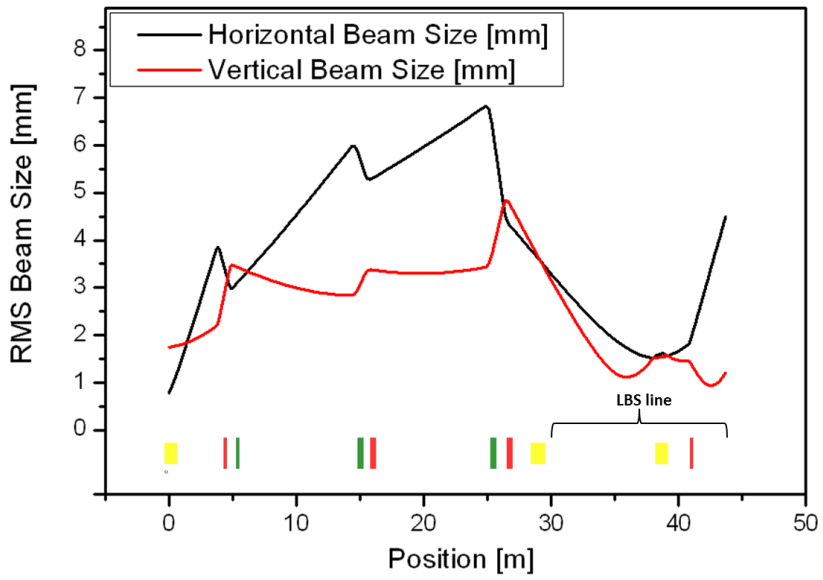

Figure 3.35: LBS Line Optics for Energy Modulation $\Delta E = \pm 1.2\,MeV$
In this plot the development of the transverse beam sizes from the dipole magnet BHZ30 to the SEM-Grid of the LBS line is shown. The six quadrupoles upstream of the LBS line are used to obtain a vertical beam size of below $\sigma_y = 1.5\,mm$ at the SEM-Grid within a loss-less beam transport. The quadrupole downstream of the spectrometer dipole is used to set a vertical dispersion of approximately $D_y = 1.5\,m$ at the SEM-Grid.

needs to be overfocused by the final quadrupole doublet upstream of spectrometer dipole magnet.
The presented horizontal beam optics is not optimised, but already adjusted to the aperture limitations of the LBS-line allowing a loss-less beam transport. At the SEM-Grid position of the LBS-line a vertical dispersion of $D_y = 1.5\,m$ is designed. In Fig. 3.36 the simulated phase space distributions of three bunches with average kinetic energies of $E_{kin.} = 160\,MeV$ and $E_{kin.} = 160\,MeV \pm 1.2\,MeV$ are plotted.

It can be concluded that the dispersion can be sufficiently reduced for the measurement of the energy modulation allowing the use of a minor SEM-Grid measurement range.
The beam optics is optimised for a clear bunch separation within a few hundreds keV energy difference. Due to the small vertical dispersion the impact of the nominal energy spread on the beam size becomes negligible.

Energy Spread - $\sigma_{energy} = 350\,keV$

Without the use of the transfer line debuncher cavity a rms energy spread of approximately $\sigma_{energy} = 350\,keV$ is expected at the entrance of the LBS-line,

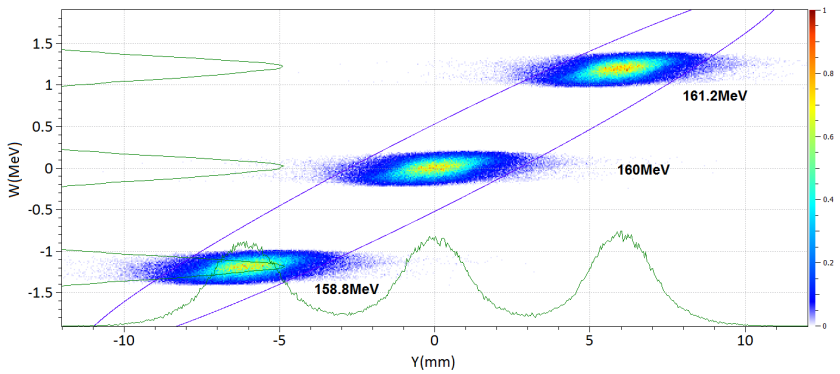

Figure 3.36: Energy Modulation - simulated Phase Space Distribution
In this plot the phase space distributions at the SEM-Grid position for three particle ensembles are shown. The average kinetic energy of the particle ensembles are $E = 160\,MeV$ *and* $E = 160\,MeV \pm 1.2\,MeV$*. By means of a vertical dispersion of* $D_y = 1.5\,m$ *a clear separation of the three bunches at the SEM-Grid is expected.*

Fig. 3.12. This energy spread corresponds to a relative momentum spread of:

$$\frac{\Delta p}{p} = \beta_E^{-2}\frac{\Delta E}{E} = 1.178 \cdot 10^{-3}, \tag{3.18}$$

with β_E the relativistic velocity of the particle bunch. Based on studies of the LBS-line beam optics vertical beam sizes at the SEM-Grid position below $\sigma_y(rms) = 1mm$ for monochromatic beams are possible.

$$\sigma_{monochromatic} = \sqrt{\beta\varepsilon} \tag{3.19}$$

$$\sigma_{nominal} = \sqrt{\beta\varepsilon + \left(D \cdot \frac{\Delta p}{p}\right)^2} \tag{3.20}$$

For the operation a difference between the beam sizes of a monochromatic beam and of a beam characterised by the nominal energy spread of $\sigma_{mono} : \sigma_{nominal} \leq 1:3$ is required[6]. Using Eq. 3.18, 3.19 and 3.20 a minimum dispersion of

$$D = \sqrt{8\frac{\beta\varepsilon}{\left(\frac{\Delta p}{p}\right)^2}} = 2.42m \tag{3.21}$$

is defined. To reduce the vertical dispersion at the SEM-Grid position to $D_y = 2.5\,m$ the spectrometer quadrupole is set to a field gradient of $g = 1\,\frac{T}{m}$, focusing in vertical plane. In Fig. 3.37 the development of the transverse beam sizes along the LBS line is plotted.

Due to the increasing dispersion downstream of the spectrometer quadrupole the vertical beam sizes of the two beams significantly differ. In Fig. 3.38 the

[6]A minimum ratio of the beam sizes of 1 : 2 is specified in [23].

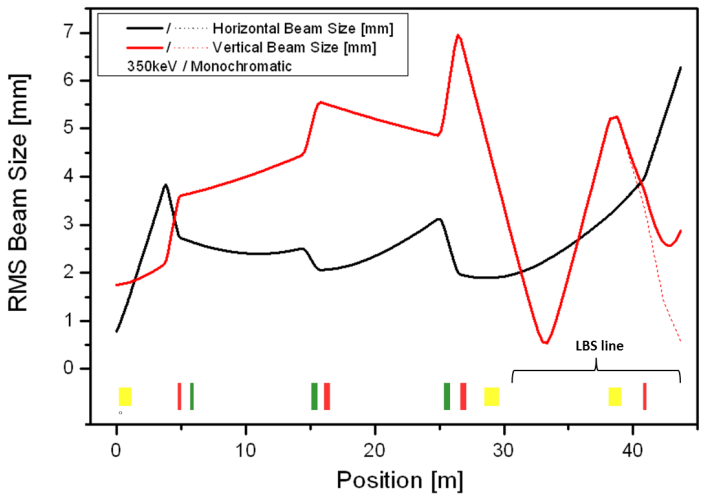

Figure 3.37: LBS Line Optics - 350 keV Energy Spread

This plot shows the vertical beam sizes of the nominal beam and of the corresponding monochromatic beam from the exit of dipole BHZ30 to the LBS-line SEM-Grid. Downstream of the spectrometer magnet significantly differences between the vertical beam sizes are obtained caused by the vertical dispersion. At the SEM-Grid a ratio of the vertical beam sizes amounts to $\sigma_{mono} : \sigma_{nominal} \approx 0.5 : 3$.

simulated phase space distribution of the 350 keV energy spread beam at the SEM-Grid is shown.

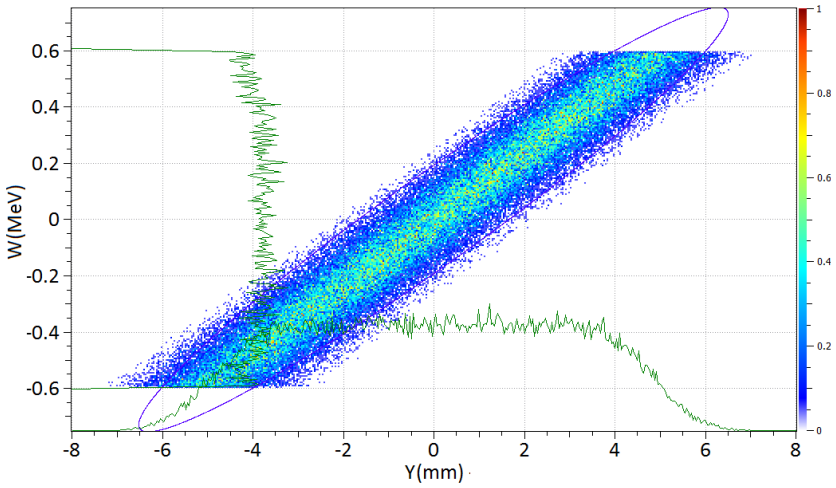

Figure 3.38: Phase Space Plot - 350 keV Energy Spread

In this plot the simulated phase space distribution, particle energy vs. vertical position, at the SEM-Grid is shown. Due to the vertical dispersion a projection of the energy distribution on the vertical spatial distribution is accomplished.

Energy Spread Calculation - $\sigma_{energy} = 350\,keV$
As the monochromatic beam size is not directly measurable, its impact on the energy spread calculation is frequently neglected. To mitigate the discrepancy between calculated energy spread and real energy spread a significant difference between the beam sizes of the monochromatic beam and the nominal energy-spread beam has to be accomplished.
In the following example a beam characterised by an energy spread of $\sigma_{energy}(rms) = 350\,keV$ is assumed. At the SEM-Grid a vertical rms beam size of $\sigma_y^{real}(rms) = 3.09\,mm$ was simulated. A monochromatic beam size of $\sigma_y^{mono}(rms) = 1.0\,mm$ is assumed. By means of the spectrometer quadrupole a vertical dispersion of $D_y = 2.5\,m$ at the SEM-Grid is obtained.
Using Eq. 3.17 a rms energy spread of $350\,keV$ is calculated. In order to estimate the error on the energy spread calculation a Taylor expansion of Eq. 3.17 with $\beta\varepsilon \to 0$ is developed:

$$\begin{aligned} \sigma_y &= \sqrt{\beta_y\varepsilon_y + \left(D_y\frac{\Delta p}{p}\right)^2}\ ; \\ \sigma_y|_{\beta\varepsilon\to 0} &= D_y\frac{\Delta p}{p} + \frac{1}{2}\frac{\beta_y\varepsilon_y}{D_y\frac{\Delta p}{p}} - \frac{1}{8}\frac{(\beta_y\varepsilon_y)^2}{(D_y\frac{\Delta p}{p})^3} + [\ldots]\ . \end{aligned} \tag{3.22}$$

This leads the following expansion

$$\sigma_y = 2.925\,mm + 0.1709\,mm - 5\,\mu m. \tag{3.23}$$

In the example the impact of the monochromatic beam size of the second order Taylor expansion amounts to 6%. Using the first order Taylor expansion to calculate the energy spread one obtains:

$$\begin{aligned} \frac{\Delta p}{p} &= \frac{\sigma_y}{D_y} = \frac{3.09\,mm}{2.5\,m}\ ; \\ \frac{\Delta p}{p} &= 1.236\cdot 10^{-3}\ . \end{aligned}$$

This corresponds to an energy spread of $367\,keV$, which is only 5 % higher than the assumed energy spread of $350\,keV$.

Nominal Energy Spread - $\sigma_{energy} = 90\,keV$

The measurement of the nominal Linac4 energy spread of $\sigma_{energy}(rms) = 90\,keV$ is the main challenge of the new LBS-line design. Assuming a minimum vertical beam size of a monochromatic beam of $\sigma_y^{mono}(rms) \approx 1\,mm$ a vertical dispersion of approximately $D_y = 11m$ is required to provide a sufficient resolution.
In order to investigate the $\sigma_{energy} = 90\,keV$ energy spread the spectrometer quadrupole is set to a field gradient of $g = 12\,\frac{T}{m}$, defocusing in vertical plane. This causes an increase of the vertical dispersion to $D_y(g = 12\,\frac{T}{m}) \approx 9.5\,m$. The

LBS-line optics is shown in Fig. 3.39.

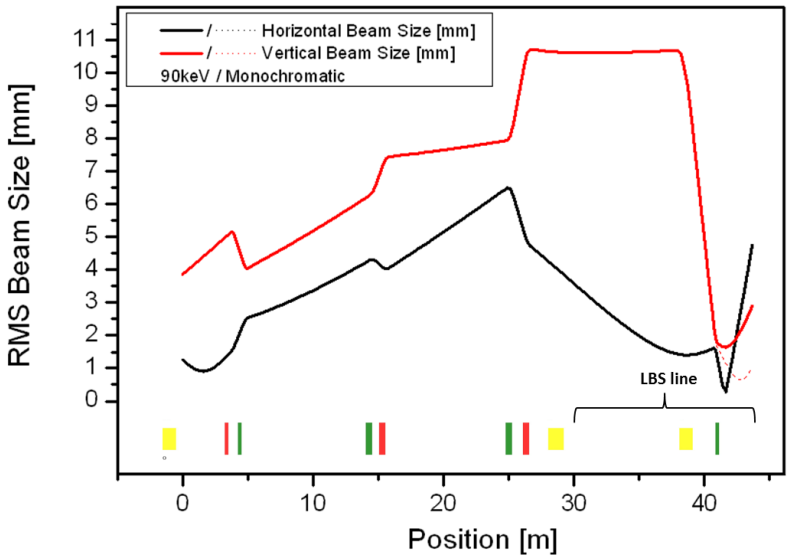

Figure 3.39: LBS Line Optics - 90 keV Energy Spread
In this diagram the development of the transverse beam sizes from the dipole magnet BHZ30 to the SEM-Grid of the LBS line is shown. In order to maximise the resolution of the LBS line a field gradient of $g = 12\,\frac{T}{m}$ *is set at the spectrometer quadrupole. By means of the weak focusing of the dipole magnet in combination with the quadrupole defocusing vertical beam sizes of* $\sigma_y^{mono} \approx 1\,mm$ *and* $\sigma_y^{nominal} \approx 2.5\,mm$ *are accomplished.*

Due to the high gradient of the spectrometer quadrupole a special matching of the vertical Twiss parameters at the entrance of the spectrometer dipole has to be accomplished. The six quadrupoles upstream the LBS line are used to maximise the vertical beam size at the entrance of the spectrometer dipole. Its weak focusing in combination with the high β-function causes a significant reduction of the beam size within a short distance. The spectrometer quadrupole is located upstream of the vertical beam waist. Its strong defocusing effect shifts the vertical beam waist further downstream, closer to the SEM-Grid. In particular this allows the extension of the lever arm to enhance the vertical dispersion. In Fig. 3.40 the simulated phase space distribution at the SEM-Grid position is plotted.
In the example an energy spread of $\sigma_{energy} = 88.4\,keV$ is assumed. Using the first order expansion of Eq. 3.22 an energy spread of $\sigma_{energy}(calulated) = 90.7\,keV$ is calculated. The discrepancy between the calculated energy spread and assumed energy spread is in the order of 2.5 %.

Based on the results of the LBS line studies it can be concluded that it is possible to examine the Linac4 energy modulation as well as the bunch energy spread down to $\sigma_{energy}(rms) \approx 90\,keV$. Moreover, in the new layout also the use of a slit is not required.

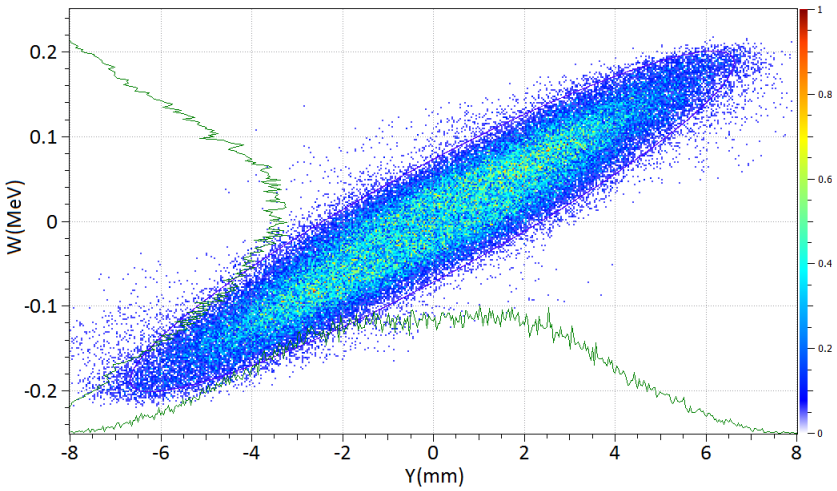

Figure 3.40: Phase Space Plot - 90 keV Energy Spread
In this plot the simulated phase space distribution of the nominal Linac4 beam at the SEM-Grid position is plotted. Due to the significantly increased dispersion of $D_y = 9.5\,m$ *an energy resolution of approximately* $30\,keV/mm$ *is obtained.*

LBS-line in Lead Ion-Operation

In addition to the investigation of the energy spread and energy modulation of H^- ion beams coming from Linac4 the control of the energy spread of heavy ion beams such as lead ion beams is foreseen. These beams are generated at the CERN Linac3 [50]. The characteristics of these beams significantly differ from the parameters of the Linac4 beams. Due to the low beam intensity and the high transverse emittance of $\varepsilon(rms) = 3\,\pi\,mm\,mrad$ space charge effects are negligible. A reduction of the energy spread using a transfer line debuncher cavity in the Linac3 transfer line leads to an estimated momentum spread of $\frac{\Delta p}{p} \leq 1.2 \cdot 10^{-4}$ at the entrance of the LBS line [50]. In the case of lead ions the momentum spread corresponds to an energy spread of approximately $\sigma_{energy} = 215\,keV$ at a kinetic energy of $E_{kin.} = 870\,MeV$. The proposed LBS-line optics for lead ion beams is adapted from the LBS-line optics for the measurement of the 90 keV energy spread beam of Linac4. Due to the high transverse emittance the vertical β-function at the spectrometer dipole has to be reduced to minimise particle losses. The lower β-function leads to a less intensive beam focusing by the dipole field.
For the lead ion operation the spectrometer quadrupole is set to a gradient $g = 8\frac{T}{m}$ to obtain a vertical dispersion of $D_y = 10\,m$ at the SEM-Grid[7]. The LBS-line optics for lead ion beams is presented in Fig. 3.41.

In Fig. 3.41 the development of the transverse beam sizes of lead ion beams with different energy spreads (215 keV, 500 keV, 870 keV) are plotted. A summary of

[7]The lead ions are 53^+ ionised.

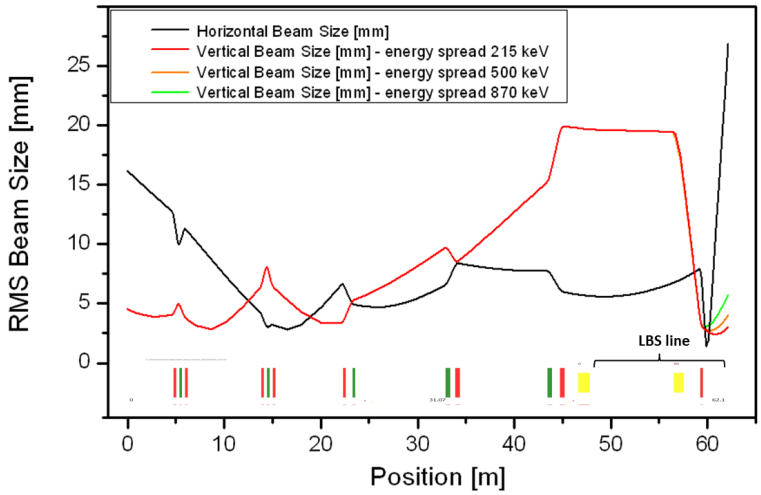

Figure 3.41: LBS Line Optics for Lead Ion Beams
In this plot the beam optics of the Lead ion beams from Linac3 to the LBS line is shown. By means of the spectrometer quadrupole a vertical dispersion of $D_y = 10\,m$ at the SEM-Grid is designed. The beam optics is optimised to provide a loss-less beam transport until the LBS-line SEM-Grid.

the calculation results is presented in Tab. 3.7. For the energy spread calculation the first order Taylor expansion of Eq. 3.17 is used. Due to the high transverse

Energy Spread	**vertical beam size at SEM [mm]**	**calculated Momentum Spread $\frac{\Delta p}{p}$)**	**calculated Energy Spread**
215keV	3.0	$3.0 \cdot 10^{-4}$	$520\,keV$
500keV	4.0	$4.0 \cdot 10^{-4}$	$700\,keV$
870keV	5.75	$5.75 \cdot 10^{-4}$	$1000\,keV$

Table 3.7: Linac3 - Ion Energy Spread Calculations - Summary
In this table the simulation results of the three assumed energy spread scenarios are summarised. As for the calculation of the energy spread the monochromatic beam size is neglected, a higher difference between assumed energy spread and calculated energy spread is obtained at lower energy spread values.

emittance of the lead ion beams the energy spread is overestimated. At present the LBS-line is used to adjust the RF-phase of the debuncher cavity rather than to measure the energy spread of the ion beams.
The new LBS-line design provides a significantly higher measurement resolution also in the case of Linac3 beam as well as for the Linac4 operations.

4

Start-to-End Simulation

In a Start-to-End simulation the beam transfer from the source to the injection point of the PS-Booster is successionally computed. These simulations are required to detect performance bottlenecks and suboptimal beam transfers between different accelerator components.
By means of the recent measurements at the source exit and at different locations along the LEBT a first characterisation of the Linac4 beam is completed. In the framework of this thesis the previous Start-to-End simulation [51] of Linac4 and transfer line was updated using the recent measurement results of the Test Stand Commissioning. For the Start-to-End simulation the measurement results were extrapolated to the RFQ exit and used to generate two H^- ion test beams, as the source commissioning showed that the measured phase space distributions of H^- ion beams and proton beams are characterised by very similar phase space characteristics, Fig. 4.1.

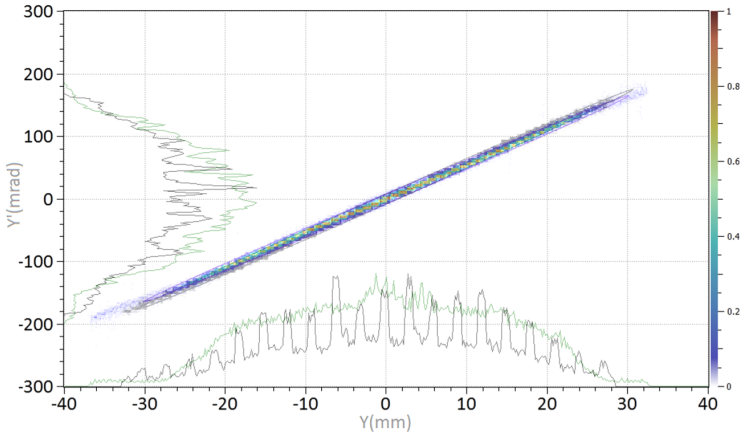

Figure 4.1: Transverse Phase Space Distributions of H^- ions & Protons
In this plot the measured transverse phase space distributions of a H^- ion beam (monochrome) and of a proton beam (colour) are plotted. Almost identical phase space distributions of H^- ion beams and proton beams were observed.

Also it is expected that their LEBT beam dynamcis is almost identical.
The measured phase space distributions differ in emittance and orientation of the phase space area from the reference beam, section 2.1.2. As a consequence a significant increase of particle losses along the LEBT was predicted and measured. The combination of LEBT measurements and RFQ simulations indicates that the maximum performance will be obtained by minimisation of the particle

losses along the LEBT, which limits the RFQ transmission to approximately 80%, Tab. A.3. For the updated Start-to-End simulation two measured phase space distributions were chosen to determine the simulation input distributions, the emittance measurements "580-330-1000" and "580-340-1000" presented in Tab. A.2. The particle distributions were tracked through the RFQ. At the exit of the RFQ these particle distributions are characterised by similar transverse emittances of $\varepsilon_x = \varepsilon_y = 0.27\pi\ mm\ mrad$. This value is in the order of the reference beam emittance of $\varepsilon_x = \varepsilon_y = 0.241\pi\ mm\ mrad$. In Fig. 4.2 the three phase space distributions at the RFQ exit are shown.

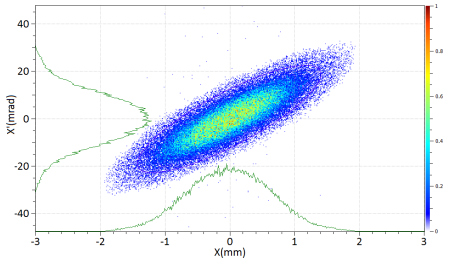

(1) Beam1 (Solenoid1 = 580 A Solenoid2 = 330 A)

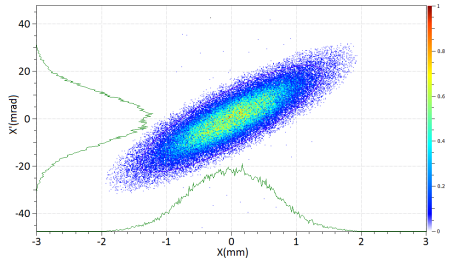

(2) Beam2 (Solenoid1 = 580 A Solenoid2 = 340 A)

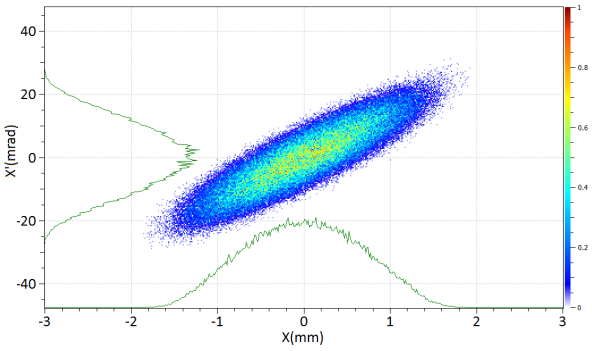

(3) Reference Beam

Figure 4.2: Horizontal Phase Space Distributions at RFQ Exit

These three plots show the transverse phase space distributions of the reference beam and of two measured beams at the exit of the RFQ. The three beams are characterised by similar transverse phase space distributions. The emittance of reference beam is approximately 10 % *smaller than the emittances of the two measured beam distributions.*

It is expected that due to the source upgrade a similar H^- ion distribution with a nominal beam current of 65 m will be obtained. For the Start-to-End simulation the nominal beam current is assumed[1].

[1]The focusing structure of the DTL is based on permanent quadrupole magnets. In the design phase the focusing configuration was optimised to enable a beam transport of space charge influenced beams with beam currents between 20 mA and 70 mA, [14][52].

A potential bottleneck of the Linac4 is the 4 m long MEBT developed to reduce the radioactive load of the PS-Booster. Its layout is shown in Fig. 4.3.

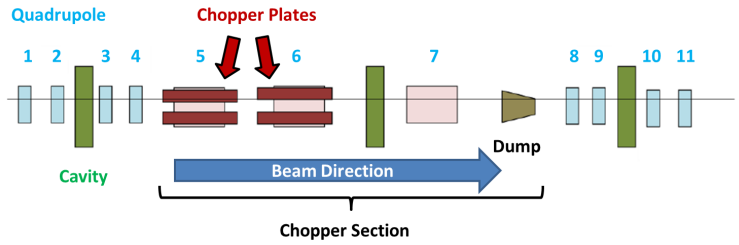

Figure 4.3: Schematic of the Linac4 MEBT
The centre part of the MEBT is the chopper section used to optimise the longitudinal bunch train structure for PS-Booster injection. It consists of two pairs of chopper plates integrated in two quadrupole magnets, a third quadrupole and a beam dump. Upstream and downstream of the chopper section each four quadrupole magnets are installed to match the beam from the RFQ to the chopper section and from the chopper section to the DTL. In order to adjust the bunch length three cavities will be used.

The centre part is designed to optimise the time structure of the bunch train, [14]. Inside the quadrupoles 5 and 6 two pairs of chopper plates are installed to cause a vertical deflection of the bunch train parts, which are supposed to be removed from the bunch train. The generated beam offset will be amplified by the defocusing impact of quadrupole 7 directing the beam into the chopper beam dump. To match the beam from the RFQ to the chopper section and from the chopper section to the DTL two families of quadrupoles are installed upstream and downstream of the chopper section.
Due to the higher transverse emittance of the measured distributions an increase of the particle losses at the MEBT beam dump is expected. In Fig. 4.4 the simulated beam optics along Linac4 are shown.

Without any re-adjustment of the optics a Linac and transfer line transmission of 85 % is obtained. The location of the particle losses are focused at the MEBT, where also in the case of the reference beam particle losses in the order of 5% are expected, Fig. 4.5.

In terms of emittance preservation the MEBT and the first two tanks of the DTL are especially crucial. At these parts the particles are low energetic and no space charge compensation is present. This leads to a high sensitivity of the beam to space-charge-driven emittance-growth.
In order to minimise the particle losses at the MEBT and to minimise the mismatch of the β-functions along the Linac the MEBT beam optics was adapted to the higher transverse emittance. To maintain the chopper efficiency only minor changes of the field settings of the quadrupoles 5, 6 and 7 were conducted. At the new MEBT optics the particle losses are reduced below 10 % within an enhanced beam matching, at which the transverse emittance growth could be

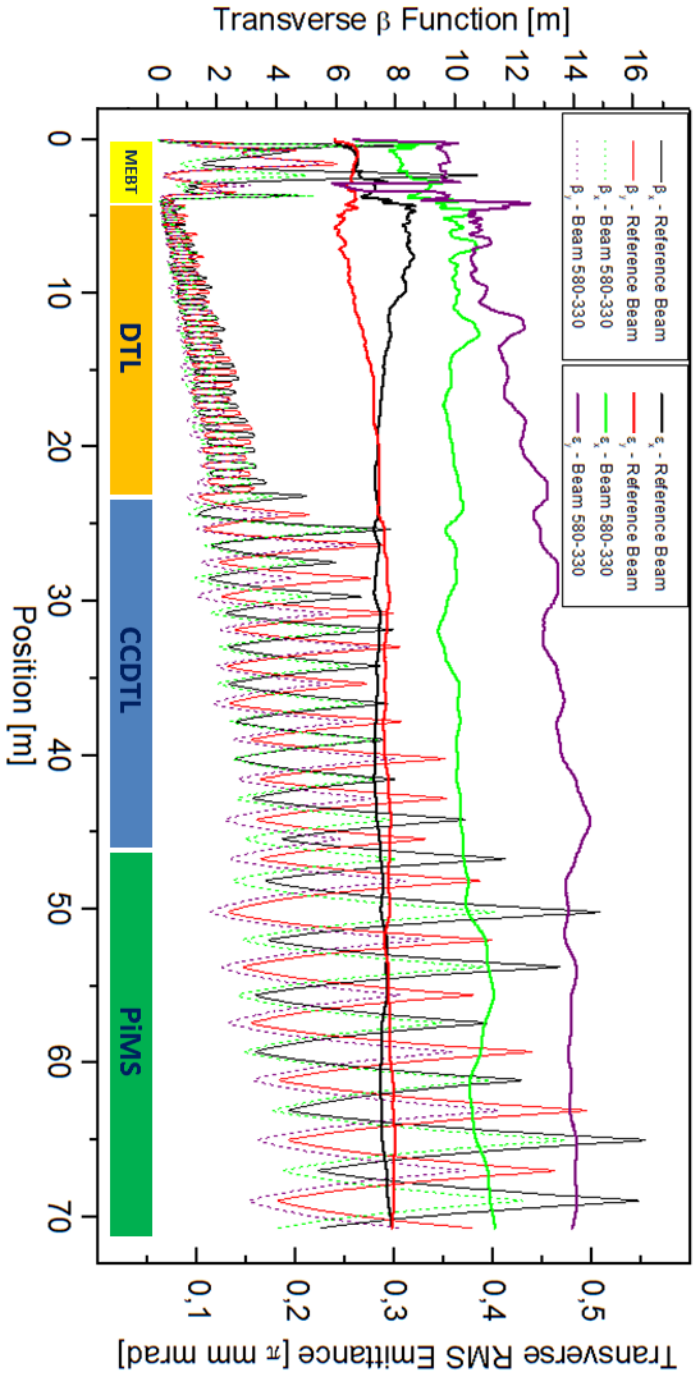

Figure 4.4: Beam Optics along Linac4 - Reference Beam Optics
In this plot the development of the transverse β-functions and transverse emittances along Linac4 is shown. Due to the higher transverse emittances of the measured beams with respect to the reference beam a significant increase of the transverse emittances and a mismatch of the β-functions along the Linac are obtained.

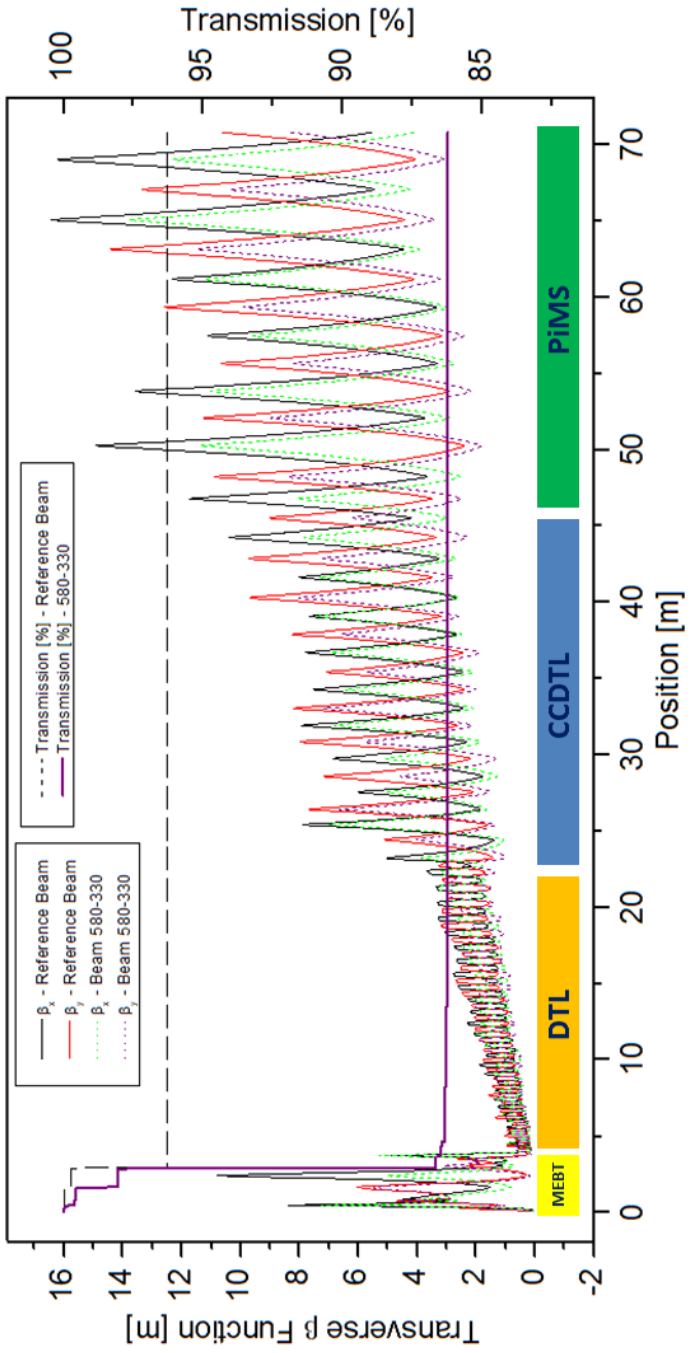

Figure 4.5: Particle Losses along Linac4 - Reference Beam Optics

In this plot the locations of the particle losses along Linac4 are shown. The particle losses are concentrated at the MEBT section, in particular the second chopper quadrupole and the chopper beam dump. Due to the increased emittance of the measured beam higher particle losses of 14 % *have been obtained.*

limited to $\varepsilon_x \approx \varepsilon_y \approx 0.45\,\pi\,mm\,mrad$, Fig. 4.6.

The location of the major transverse emittance increase is at the second half of the MEBT, where the transverse beam size needs to be strongly reduced twice to minimise particle losses at the chopper beam dump and to match the beam to the DTL. Further increases of the transverse emittance are detected along the CCDTL. In this section the development of the transverse β-functions of the two measured beams differ from the reference optics. It is expected that the further emittance increase along the CCDTL can be mitigated by adaption of the CCDTL beam optics to the higher transverse emittance. Due to the re-adjustment of the MEBT optics the beam mismatch was reduced. At the exit of the Linac the two measured beams are characterised by a higher transverse emittance of $0.45\,\pi\,mm\,mrad$.

As the transfer line optics was optimised to a specified space charge impact mainly defined by the beam parameters beam current and beam emittance, the higher transverse emittance leads to a reduction of the space charge effects, which causes an additional mismatch between beam and beam optics. However, only minor variations of the development of the transverse β-functions along the transfer line are observed, Fig. 4.7.
The major critical section of the transfer line in terms of emittance preservation is the first transfer line section upstream of the vertical chicane and in particular in between the first two bending magnets. In this section intense space charge effects are expected. In between the first bending magnets it is required to control the horizontal dispersion in presence of the intense space charge effects within minimisation of emittance growth. The higher transverse emittance leads to a reduction of the space charge defocusing. As a consequence the 'space charge' dispersion bump between the first two bending magnets is not perfectly closed leading to significant increase of the horizontal emittance. At the PS-Booster the transverse emittance increased to $\varepsilon_x \approx \varepsilon_y \approx 0.5\,\pi\,mm\,mrad$. In spite of the increased emittance and the minor beam mismatch a low-loss beam transport within acceptable PS-Booster matching is accomplished. A further reduction of the transverse emittance growth by the adaption of the transfer line optics to the higher initial transverse emittance is possible. The transverse emittance growth is limited to approximately 10 %. This shows that the transfer line optics is highly sophisticated, as the optical solution is stable within major variations of the beam parameters.

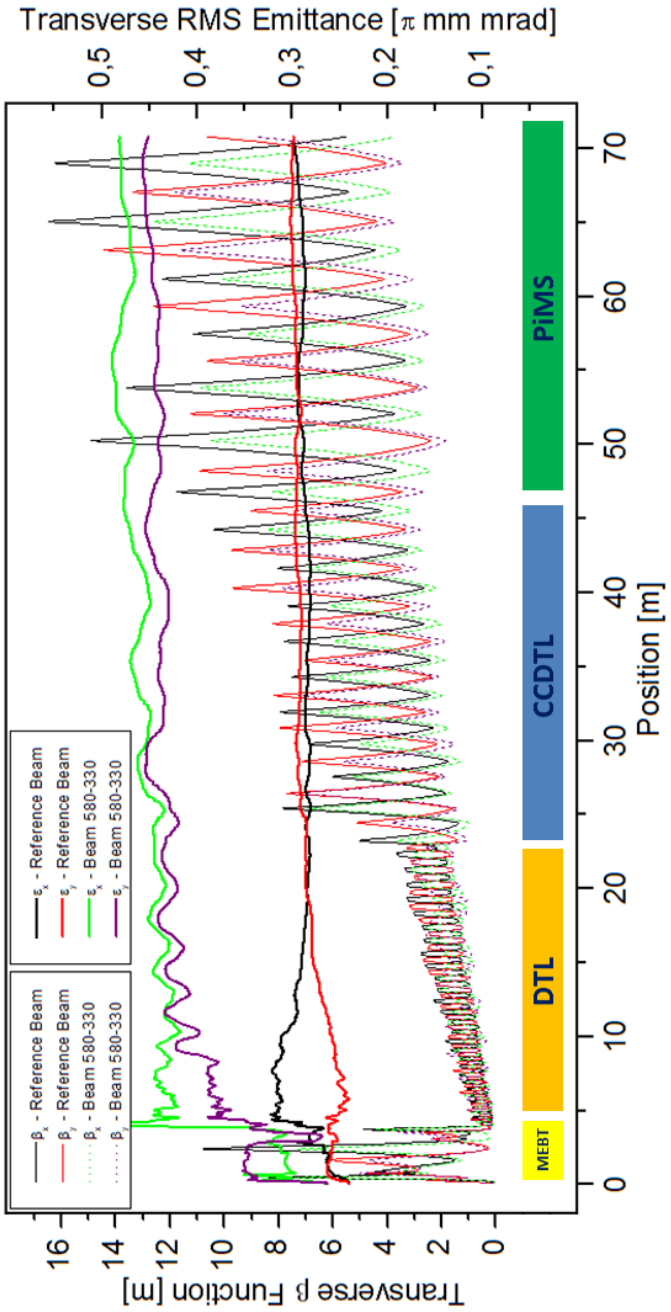

Figure 4.6: Rematched Beam Optics Linac4

In this diagram the development of the transverse β-functions and the transverse emittance along the Linac of one test beam and of the reference beam is shown. The main increase of the transverse emittance is located at the second half of the MEBT, where the beam needed to be focused twice to minimise losses at the chopper dump and to match the beam to the DTL. A second location of major transverse emittance growth is the CCDTL.

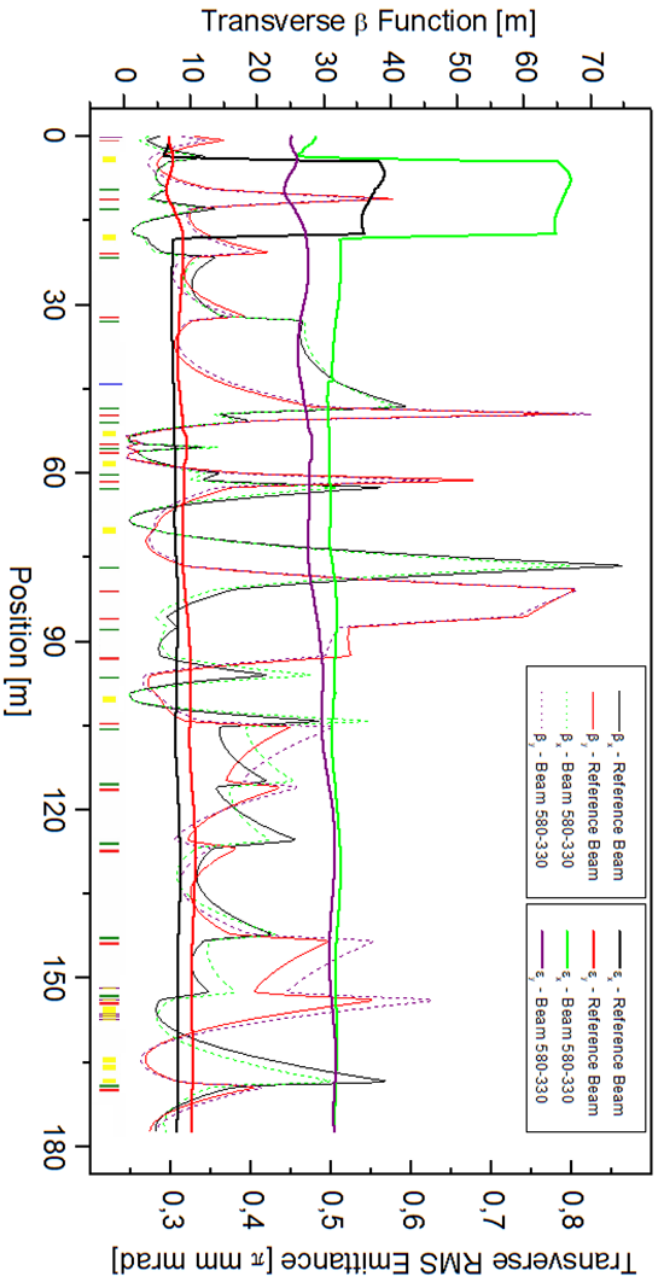

Figure 4.7: Transfer Line Optics

In this plot the development of the transverse β-functions and transverse emittance along the transfer line is shown. As the transfer line optics is optimised for the expected space charge impact of the reference beam, the reduced space charge impact caused by the increased emittance of the measured beams leads to a further emittance increase. The emittance increase is limited to approximately 10 % without an re-adjustment of the optics. A low-loss beam transport within good PS-Booster matching is accomplished.

Based on the results of the Start-to-End simulations it can be concluded that in terms of transverse emittance preservation the MEBT beam optics is most critical. The adjustment of the MEBT beam optics to varying beam properties is required to minimise particle losses and transverse emittance growth along the MEBT and the DTL.
The transfer line optics is designed to ensure optimised transverse emittance preservation for the reference beam. Due to the lower charge density of the measured beams a lower space charge impact is caused. This leads to non-closed space-charge dispersion-bumps. In combination with the minor variation of the transverse Twiss parameters the mismatch of the measured beams to the transfer line optics leads an increase of the transverse emittance. This emittance growth is in the order of 10 % indicating that the transfer line optics permits a stable beam transport within significant variations of the beam parameters. It is expected that a minor variation of the transfer line quadrupoles settings will be sufficient to restore the optimised transverse emittance preservation.

5
Conclusion

The latest upgrade of the CERN accelerator complex by the construction of the Large Hadron Collider (LHC) offers the possibility to explore physics beyond the standard model. In order to detect processes characterised by infinitesimal cross sections a high luminosity for the experiments is needed. At present the major limitation towards higher luminosity achieved by enhanced proton intensity is given by the accelerator injector chain, in particular by the performance of the PS-Booster at beam injection.
For a maximised beam brilliance bunch trains coming from Linac2 are accumulated in each of the four buckets of the PS-Booster.[1] The high bunch charge and low kinetic energy of the particle ensembles lead to intense space charge effects, which limit the PS-Booster performance. Due to the non-linear space charge effects the tune of the PS-Booster converts into a tune spread. In order to improve the PS-Booster performance it is foreseen to increase the PS-Booster injection energy to mitigate the intensity of the space charge effects. For this purpose the construction of a new, normal-conducting H^- ion Linac, Linac4, is planned. Critical parts of this Linac in terms of beam quality preservation are the beam transport sections between the different accelerator elements, whose beam dynamics are in the focus of this thesis.
Implemented in the design of Linac4 are three beam transport sections, a Low Energy Beam Transport LEBT, a Medium Energy Beam Transport MEBT and a High Energy Beam Transport HEBT section, which is the transfer line from Linac4 to the PS-Booster.
The LEBT, located between the source exit and the first accelerator element, the RFQ, is used to match the source beam into the RFQ. The degrading impact of space charge is mitigated by the residual-gas-induced space-charge-compensation and the compact design of the LEBT. However, this section is characterised by high particle losses. These particle losses limit the degree of freedom for the beam matching to the RFQ, which determines the beam transmission through the RFQ and the beam emittance at the exit of the RFQ.
Downstream of the RFQ the MEBT is used to model the bunch train structure for the PS-Booster injection and to match the beam to the Drift Tube Linac, DTL. In order to manipulate the bunch train structure a chopper section has been integrated in the MEBT. Hence, the MEBT beam optics is characterised by a significantly lower phase advance than the optics of RFQ and DTL. Due to the fast changes of the beam optics combined with intense space charge effects a high potential of transverse emittance growth is present at the MEBT section and along the first sections of the DTL.
Downstream of the MEBT the aperture limitations and the dense focusing

[1] Each of the PS-Booster bunches will be split up to 24 LHC bunches depending on the PS-Booster operation along the remaining accelerator chain .

structure of the Linac4 components DTL, CCDTL and PiMS permit a low-loss beam transport. Along this focusing structure the H^- ion beam is constantly focused leading to compact bunch dimensions and also to intense space charge fields. To limit the transverse and longitudinal emittance growth the dense focusing structure is used to maintain the beam dimensions as constant as possible. Due to the different focusing structure of the transfer line the first section of the transfer line shows a high potential of space-charge-driven emittance-growth.
The first components of the Linac, namely source, the Test-Stand-LEBT, the RFQ and the MEBT, are commissioned at a special Test Stand. The first part of this thesis is focused on the beam dynamics commissioning of the first low-energy front-end components of Linac4 at the $3\,MeV$ Test Stand, i.e. the commissioning of the H^- ion source and the commissioning of the Test-Stand-LEBT.
During the commissioning of the Linac4 source detailed investigations of the beam characteristics were conducted. These investigations focused on the variation of beam parameters depending on the source settings. It was shown that the measured phase space distributions significantly differ in terms of emittance and Twiss parameters from the assumed beam parameters. Based on the measured beam parameters theoretical studies of the LEBT performance were conducted to optimise its performance.
The commissioning of the LEBT was divided into two phases. In the first phase the transverse phase space distribution and particle momentum downstream of the first solenoid were measured. The measurement results were used to estimate the space charge compensation along the LEBT and to benchmark the simulation code PATH.
The second phase of the LEBT commissioning was focused on the optimisation of the LEBT performance and the preparation of the RFQ commissioning. In this commissioning phase the Test Stand LEBT was completely assembled and equipped with an emittance meter and a Faraday cup at its exit. In order to optimise the LEBT performance and to identify performance bottlenecks the LEBT beam dynamics was re-constructed. The major limitation of the Test Stand LEBT is the aperture limitation of the first solenoid in combination with the significantly higher transverse emittance, which led to particle losses of approximately 40 % depending of the LEBT settings. Based on LEBT simulations and measurements at the source exit and at the exit of the LEBT the acceptance of the Test-Stand-LEBT was determined.

The High Energy Beam Transport (HEBT) is in the focus of the second part of this thesis. The layout and the beam dynamics of the transfer line from the exit of Linac4 to the PS-Booster injection point were analysed and major variations of the transfer line layout and transfer line optics were conducted. In order to enhance the efficiency of the debuncher cavity in terms of energy spread reduction and the reduction of the RF-power consumption its position in the transfer line layout was shifted downstream by approximately $8\,m$. The transverse focusing scheme of the first transfer line section was re-designed to improve the preservation of the transverse emittance, whereby the transverse

emittance growth could be limited to less than 10 %. As a consequence of these modifications a reduction of potential particle losses in presence of field jitters and misalignments and an excellent PS-Booster matching are obtained.
For the Start-To-End simulation the latest measurement results of the low-energy front-end commissioning were used to define initial beam characteristics. Downstream of the RFQ the MEBT optics was adapted to the higher beam emittance to minimise particle losses and emittance growth. The final transverse emittance at the exit of the Linac could be preserved along the transfer line within acceptable PS-Booster matching.
A potential performance bottleneck of Linac4 is the MEBT beam dynamics. Along the RFQ the beam pulse will be converted into a train of bunches, whereby no space charge compensation by the residual gas molecules is expected. Moreover, the focusing structure of RFQ and DTL are high phase advance structures, but for the MEBT optics a lower phase advance is required. Hence, a high sensitivity of the MEBT optics to transverse emittance increase is expected, which is considered in the commissioning agenda of the MEBT.

Outlook

The Test Stand commissioning showed that the characteristics of the source beam significantly differ from the assumption and do lead to intense particle losses.
During the source commissioning phase II in 2011 a different focusing scheme for the source beam was tested for which the source extraction cathode was exchanged[2]. Based on simulations of source dynamics it was shown that the focusing impact of the cathode strongly depends on the beam parameters emittance and beam intensity. The restricted space of the extraction part allowed only minor variations. In a measurement campaign conducted with the new cathode the source parameters transverse emittance and beam current were investigated at varying source settings. The comparison with the measurement results of the original cathode showed that the beam focusing, transverse emittance and beam current were preserved.
Due to technical reasons the Test Stand commissioning was conducted using proton beams instead of H^- ion beams. In the re-designing process of the source the extraction system has been completely altered. In order to tune the beam parameters the new extraction system is equipped with electrostatic lenses. Its performance is currently under experimental examination and a stable H^- ion operation has been already achieved.
Based on the re-constructed LEBT beam dynamics the first solenoid of the LEBT was identified as a main performance limitation of the Test Stand accelerator. As a consequence it was decided to proceed the Test Stand commissioning with the final Linac4 LEBT, which is equipped with different types of

[2]The shape and position of the cathode was altered to shift the beam waist further towards the first solenoid.

solenoid magnets providing a higher LEBT acceptance. A fast commissioning of the new LEBT has been completed, the first H^- ions were injected into the RFQ and accelerated to $3\,MeV$. At present the commissioning of the RFQ and the optimisation of the H^- ion source are ongoing.

Appendix A
Measurement Results - Test Stand

A.1 RFQ Injection Parameters

The impact of space charge effects along the RFQ is considered by the adjustment of the injection Twiss parameters. In dependence of the transverse emittance and beam current different injection parameter sets were defined [34].

Emittance	α_{70mA}	β_{70mA} $[cm]$	α_{40mA}	β_{40mA} $[cm]$
0.25	1.21	3.12	1.03	2.726
0.26	1.195	3.08	1.023	2.707
0.27	1.18	3.05	1.015	2.69
0.28	1.166	3.02	1.007	2.674
0.29	1.153	2.99	1	2.659
0.30	1.14	2.964	0.994	2.645
0.31	1.13	2.939	0.988	2.631
0.32	1.119	2.915	0.982	2.62
0.33	1.11	2.895	0.977	2.609
0.34	1.1	2.875	0.972	2.598
0.35	1.092	2.855	0.967	2.588
0.36	1.083	2.838	0.963	2.578
0.37	1.075	2.82	0.959	2.569

Table A.1: RFQ Injection Parameters
Due to the high periodical, high phase advance lattice of the RFQ the beam Twiss parameter matching is crucial in terms of emittance preservation and minimisation of particle losses. The impact of space charge depending on the beam parameters beam current and transverse emittance is considered by the adjustment of the injection Twiss parameters. The data of this table was provided by [34].

A.2 LEBT Settings for RFQ Injection

Based on the phase space measurements at the LEBT exit sets of LEBT settings for the RFQ commissioning have been identified. In Tab. A.2 these LEBT settings and the measured beam parameters are summarised.

Setting	$I[mA]$	$\varepsilon_x(norm)$ $[mm\,mrad]$	α_x	β_x $[m]$	$\varepsilon_y(norm)$ $[mm\,mrad]$	α_y	β_y $[m]$
560-330-1000	29.1	0.38	-0.18	0.02	0.39	-0.54	0.04
580-330-1000	31.1	0.32	0.75	0.04	0.35	0.58	0.06
580-340-1000	31.1	0.34	0.0	0.002	0.36	0.2	0.04
580-350-1000	31.1	0.37	-0.62	0.03	0.34	-0.16	0.03
600-330-1000	29.5	0.32	1.49	0.1	0.28	1.63	0.16
600-340-1000	29.6	0.37	0.9	0.05	0.35	1.22	0.09
600-350-1000	29.6	0.38	0.36	0.03	0.31	0.86	0.06
620-340-1000	25.1	0.33	1.76	0.09	0.3	2.0	0.11
620-350-1000	25.1	0.38	0.88	0.04	0.3	1.42	0.06
620-360-1000	24.5	0.37	0.26	0.02	0.3	0.77	0.03
665-355-1-0.2500	12.8	0.34	0.55	0.02	0.22	0.76	0.02
665-365-1-0.2500	11.7	0.37	-0.37	0.02	0.21	-0.34	0.01
665-375-1-0.2500	10.7	0.36	-1.5	0.04	0.28	-1.6	0.04
680-355-1-0.2500	10	0.34	0.34	0.02	0.21	0.52	0.02

Table A.2: List of feasible LEBT Settings for RFQ Injection
This table summarises the LEBT settings identified for the RFQ commissioning. To indicate the LEBT settings a special nomenclature is used, e.g. 600-340-1000 determines solenoid1 current $I_{sol1} = 600\,A$, solenoid2 current $I_{sol2} = 340\,A$, first horizontal steerer magnet current $1\,A$ and the remaining steerer magnets turned off. In addition to the LEBT settings the detected horizontal and vertical emittances and Twiss parameters as well as the beam current are recorded. For the LEBT measurements a minimum source beam emittance of $\varepsilon = 0.5\,\pi\,mm\,mrad$ can be assumed. The detected emittance values are well below the source beam emittance.

A.3 RFQ Ejection Parameters (simulated)

Based on the LEBT beam measurements test beam were generated and tracked through the RFQ. A summary of the simulated beam parameters at the RFQ exit is presented in Tab. A.3.

Setting Sol1[A]-Sol2[A]	I_{LEBT} $[mA]$	RFQ Transmission [%]	RFQ Output Current $[mA]$	$\varepsilon_x(norm)$ $[mm\,mrad]$	$\varepsilon_y(norm)$ $[mm\,mrad]$
560-330	29.1	67.5	19.6	0.34	0.34
580-330	31	79	24.5	0.265	0.26
580-340	31	79	24.5	0.26	0.265
580-350	31	65	20.2	0.283	0.28
600-330	29.5	46.5	13.7	0.33	0.31
600-340	29.6	64	19	0.30	0.28
600-350	29.6	78.7	23.3	0.28	0.28
620-340	25.1	55.4	14	0.34	0.33
620-350	25.1	79	20	0.30	0.29
620-360	24.5	87.4	21.4	0.27	0.27
665-355	12.8	94.3	12	0.27	0.25
665-365	11.7	80	9	0.27	0.26
665-375	10.7	55	6	0.30	0.32
680-355	10	92.4	9	0.27	0.25

Table A.3: RFQ Ejection Parameters - Simulated
In this table the results of the RFQ simulations are summarised. Based on the measurement results listed in Tab. A.2 RFQ simulations were conducted. For each solenoid1 setting a solenoid2 setting was identified with a RFQ transmission of at least approximately 80 %.

A.4 Pencil Beam Parameters

A.4.1 RFQ Injection Parameters

Settings	$I[mA]$	$\varepsilon_x(norm)$ $[mm\,mrad]$	α_x	β_x $[m]$	$\varepsilon_y(norm)$ $[mm\,mrad]$	α_y	β_y $[m]$
560-330-1000	1.2	0.14	3.96	0.63	0.38	1.6	0.3
580-330-1000	1.4	0.14	1.45	0.1	0.11	1.4	0.09
580-340-1000	1.4	0.14	1.17	0.07	0.11	1.1	0.05
580-350-1000	-	0.18	0.5	0.04	0.12	0.5	0.03
600-330-1000	1.9	0.08	3.1	0.2	0.15	1.1	0.11
600-340-1000	1.9	0.09	2.1	0.1	0.09	1.5	0.08
600-350-1000	1.9	0.09	1.3	0.05	0.16	0.5	0.05
620-340-1000	2.6	0.09	2.8	0.41	0.14	1.3	0.01
620-350-1000	2.7	0.09	2.0	0.07	0.15	0.9	0.06
620-360-1000	2.7	0.12	0.71	0.03	0.16	0.5	0.04
665-355-1-0.2500	5.8	0.26	0.2	0.02	0.2	0.56	0.02
665-365-1-0.2500	5.5	0.28	-0.4	0.02	0.21	-0.5	0.02
665-375-1-0.2500	5.2	0.25	-1.1	0.04	0.22	-1.4	0.04
680-355-1-0.2500	7.8	0.29	0.21	0.02	0.21	0.4	0.02

Table A.4: Pencil Beam Parameters 11 mm Iris - RFQ Input

*In this table the pencil beam parameters (*11 mm *iris) for the RFQ commissioning are summarised. Depending on the LEBT settings the pencil beam current and the transverse emittance is tunable in a wide range from* $I = 7.8\,mA$ *to* $I = 1.2\,mA$ *and* $\varepsilon = 0.3\,\pi\,mm\,mrad$ *to* $\varepsilon = 0.08\,\pi\,mm\,mrad$.

A.4.2 RFQ Ejection Parameters (simulated)

Settings	$I[mA]$	$\varepsilon_x(norm)$ $[mm\,mrad]$	α_x	β_x $[m]$	$\varepsilon_y(norm)$ $[mm\,mrad]$	α_y	β_y $[m]$
560-330-1000	0.2	0.03	1.96	0.15	0.06	1.1	0.09
580-330-1000	0.2	0.03	2.14	0.17	0.04	1.5	0.11
580-340-1000	0.3	0.03	1.56	0.09	0.06	0.8	0.07
580-350-1000	-	0.04	1	0.05	0.04	0.7	0.04
600-330-1000	0.3	0.03	2.3	0.2	0.05	1.1	0.11
600-340-1000	0.3	0.03	1.6	0.1	0.07	0.7	0.08
600-350-1000	0.3	0.06	0.3	0.04	0.06	0.5	0.05
620-340-1000	0.4	0.04	1.9	0.12	0.05	1.4	0.1
620-350-1000	0.5	0.04	1.37	0.07	0.06	0.7	0.06
620-360-1000	0.4	0.04	0.7	0.03	0.05	0.6	0.04
665-355-1-0.2500	1.2	0.07	0.82	0.01	0.13	0.6	0.02
665-365-1-0.2500	1.2	0.07	0.2	0.02	0.14	-0.3	0.02
665-375-1-0.2500	1.2	0.08	-0.42	0.03	0.16	-1.1	0.04
680-355-1-0.2500	2.1	0.13	0.6	0.03	0.17	0.3	0.02

Table A.5: Pencil Beam Parameters $5\,mm$ Iris - RFQ Input

This table summarises the pencil beam parameters ($5\,mm$) at the RFQ injection plane. The beam current and the transverse emittance are tunable in the range from $I = 2.1\,mA$ to $0.2\,mA$ and from $\varepsilon = 0.13\,\pi\,mm\,mrad$ to $\varepsilon = 0.03\,\pi\,mm\,mrad$.

Settings	$I[mA]$	$\varepsilon_x(norm)$ $[mm\,mrad]$	α_x	β_x $[m]$	$\varepsilon_y(norm)$ $[mm\,mrad]$	α_y	β_y $[m]$
560-330-1000	0.29	0.45	-1.85	0.13	0.56	1.61	0.13
580-330-1000	1.3	0.25	-1.56	0.11	0.22	1.36	0.11
580-340-1000	1.4	0.16	-1.45	0.11	0.13	1.41	0.11
580-350-1000	1.4	0.09	-1.48	0.11	0.09	1.57	0.12
600-330-1000	1.7	0.3	-1.56	0.11	0.27	1.33	0.11
600-340-1000	1.9	0.21	-1.46	0.11	0.18	1.38	0.11
600-350-1000	1.9	0.11	-1.5	0.11	0.1	1.52	0.12
620-340-1000	2.4	0.27	-1.47	0.11	0.25	1.33	0.11
620-350-1000	2.7	0.17	-1.44	0.11	0.17	1.50	0.12
620-360-1000	2.7	0.12	-1.53	0.11	0.12	1.47	0.12
665-355-1-0.2500	5.5	0.23	-1.51	0.11	0.22	1.46	0.12
665-365-1-0.2500	4.6	0.25	-1.49	0.11	0.26	1.51	0.12
665-375-1-0.2500	3.6	0.3	-1.33	0.10	0.33	1.38	0.10
680-355-1-0.2500	7.2	0.25	-1.52	0.11	0.23	0.152	0.12

Table A.6: Pencil Beam Parameters $11\,mm$ Iris - RFQ Output

In this table the simulated pencil beam parameters ($11\,mm$ iris) at the RFQ exit are summarised. Depending on the settings of the solenoid2 the transverse emittance preservation can be controlled. The final transverse emittances vary between $\varepsilon = 0.33\,\pi\,mm\,mrad$ to $\varepsilon = 0.09\,\pi\,mm\,mrad$.

Settings	$I[mA]$	$\varepsilon_x(norm)$ $[mm\,mrad]$	α_x	β_x $[m]$	$\varepsilon_y(norm)$ $[mm\,mrad]$	α_y	β_y $[m]$
560-330-1000	0.2	0.13	-1.59	0.12	0.11	1.41	0.11
580-330-1000	0.2	0.15	-1.61	0.12	0.12	1.39	0.11
580-340-1000	0.3	0.08	-1.45	0.11	0.07	1.35	0.11
580-350-1000	0.2	0.04	-1.37	0.10	0.04	1.32	0.11
600-330-1000	0.3	0.15	-1.61	0.12	0.13	1.36	0.11
600-340-1000	0.3	0.08	-1.44	0.11	0.09	1.38	0.11
600-350-1000	0.3	0.05	-1.37	0.10	0.05	1.38	0.11
620-340-1000	0.4	0.12	-1.54	0.11	0.14	1.41	0.11
620-350-1000	0.5	0.07	-1.40	0.11	0.07	1.46	0.11
620-360-1000	0.4	0.05	-1.35	0.10	0.05	1.41	0.11
665-355-1-0.2500	1.2	0.09	-1.43	0.11	0.12	1.50	0.12
665-365-1-0.2500	1.16	0.10	-1.43	0.11	0.14	1.45	0.11
665-375-1-0.2500	1.1	0.16	-1.46	0.11	0.22	1.35	0.11
680-355-1-0.2500	2.1	0.14	-1.47	0.11	0.17	1.46	0.11

Table A.7: Pencil Beam Parameters $5\,mm$ Iris - RFQ Output

In this table the simulated pencil beam parameters (5 mm iris) at the RFQ exit are listed. Due to the smaller bore radius of the 5 mm iris a further reduction of the transverse emittance and beam current of the pencil beams at the RFQ entrance can be accomplished. The preservation of the transverse emittance along the RFQ is mainly determined by the settings of solenoid2.

A.5 SteererMap

For compensation of alignment errors of LEBT and RFQ the use of steerer magnets is foreseen. In preparation of the RFQ commissioning two steerer maps were recorded. At these steerer maps beam parameters have been measured in dependence of the settings of the steerer magnets. For the identification of alignment mismatch the position of the beam centre is crucial, at which the beam parameters horizontal beam position $x\,[mm]$, horizontal beam slope $x'\,[mrad]$, vertical beam position $y\,[mm]$ and vertical beam slope $y'\,[mrad]$ have been determined at the exit of the LEBT in dependence of the steerer settings. Moreover, the parameters of the transverse phase space distribution, emittance $\varepsilon_{x,y}[\pi\,mm\,mrad]$ and Twiss parameters $\alpha_{x,y}[-]$, $\beta_{x,y}[m]$, have been measured. In Tab. A.8 to Tab. A.12 the steerer map of the solenoid setting Solenoid1 current $580\,A$ and Solenoid2 current $340\,A$ is presented.
The reference scans are related to the nominal steerer setting of "*1 0 0 0* ", at which a current of $I = 1\,A$ at the first horizontal steerer is used and the remaining steerer magnets have been turned off.

Datum	x	x'	y	y'	ε_x	α_x	β_x	ε_y	α_y	β_y
29.09.	0.32	9.05	3.08	-11.54	0.284	-5.06	0.44	0.354	-2.18	0.21
30.09.	0.4	9.93	3.16	-10.85	0.284	-4.62	0.39	0.346	-1.85	1.79
04.10.	0.47	9.78	3.12	-10.4	0.31	-3.77	0.3	0.274	-2.12	0.17
05.10.	0.39	9.35	3	-12.45	0.28	-4.4	0.35	0.35	-2.28	0.19
06.10.	0.4	9.35	3.09	-11.67	0.29	-4.28	0.35	0.35	-2.39	0.2

Table A.8: Reference Scans

I	x	x'	y	y'	ε_x	α_x	β_x	ε_y	α_y	β_y
-1	-0.31	-14.2	5	19.2	0.35	-2.64	0.28	0.377	-1.44	0.17
-0.5	-0.28	-9.77	4.4	11.3	0.32	-3.23	0.32	0.328	-1.86	0.19
0	0.12	-1.25	3.9	1.78	0.32	-3.79	0.35	0.38	-1.9	0.2
0.5	0.15	3.7	3.54	-3.47	0.29	-4.64	0.41	0.33	-2.36	0.22
1.5	0.5	14	2.7	-18.8	0.29	-4.99	0.44	0.33	-2.37	0.24
2	0.66	18.2	2.3	-25.15	0.33	-4.37	0.41	0.38	-1.9	0.21

Table A.9: Steerer1 Horizontal

I	x	x'	y	y'	ε_x	α_x	β_x	ε_y	α_y	β_y
-1.5	2.1	34.3	5.07	13.4	0.28	-4.55	0.39	0.42	-1.9	0.195
-1	1.5	25.6	4.4	5.8	0.27	-4.96	0.42	0.36	-2.4	0.22
-0.5	0.98	17.7	3.85	-2.9	0.28	-4.96	0.42	0.36	-2.37	0.22
0.5	-0.12	1.33	2.44	-20.9	0.28	-4.8	0.43	0.32	-2.16	0.21
1	-0.72	-6.6	1.7	-29.8	0.297	-4.5	0.44	0.27	-2.4	0.25
1.5	-1.28	-14.7	1.2	-36.9	0.32	-3.92	0.43	0.29	-2.2	0.25

Table A.10: Steerer1 Vertical

I	x	x'	y	y'	ε_x	α_x	β_x	ε_y	α_y	β_y
-8	8.1	22.3	-4.4	-20.2	0.33	-3.42	0.31	0.23	-3.14	0.26
-6	6.1	18.1	-2.6	-18.4	0.32	-3.93	0.3	0.22	-2.76	0.23
-4	4.1	12.6	0.49	-15.3	0.29	-4.34	0.37	0.32	-1.95	0.17
-2	2.2	10.1	1.34	-13.5	0.33	-3.86	0.33	0.29	-1.87	0.17
-1	1.27	8.15	2.24	-13.1	0.276	-4.43	0.38	0.33	-1.8	0.17
-0.5	0.89	10.1	2.74	-12.7	0.26	-4.88	0.4	0.34	-1.7	0.16
0.5	0.26	9.37	3.87	-11.32	0.31	-4.2	0.36	0.35	-1.8	0.17
1	-0.27	8.54	4.2	-11.37	0.28	-4.9	0.41	0.3	-1.98	0.18
2	-1.06	8.8	4.8	-13.4	0.31	-4.4	0.4	0.26	-2.5	0.24
4	-3	5.36	7.02	-7.4	0.32	-4.2	0.38	0.33	-1.8	0.19
6	-5.1	2.45	8.83	-2.13	0.29	-4.3	0.39	0.32	-1.67	0.18
8	-6.96	-1.35	10.9	-3.4	0.27	-4.6	0.42	0.182	-2.04	0.19

Table A.11: Steerer2 Horizontal

I	x	x'	y	y'	ε_x	α_x	β_x	ε_y	α_y	β_y
-8	-6.99	2.3	-3.6	-19	0.25	-4.77	0.44	0.43	-2.37	0.24
-6	-5.1	4.4	-1.9	-16.9	0.27	-4.78	0.44	0.4	-2.59	0.26
-4	-2.8	9.2	-0.1	-15.2	0.25	-4.6	0.39	0.37	-2	0.19
-2	-1.3	8.2	1.5	-14.8	0.26	-4.76	0.4	0.39	-1.7	0.17
-1	-0.5	8.2	2.3	-13.9	0.29	-4.6	0.39	0.38	-1.65	0.16
-0.5	0	8	2.7	-13.4	0.28	-4.2	0.35	0.34	-1.7	0.16
0.5	1.2	8.4	3.6	-10.4	0.25	-4.8	0.4	0.29	-1.9	0.17
1	0.94	10.3	4	-10.6	0.29	-4.2	0.35	0.34	-1.7	0.17
2	2.2	10.2	4.8	-10	0.24	-5.1	0.43	0.33	-1.8	0.18
4	4.1	11.9	6.5	-6.4	0.29	-4.3	0.38	0.33	-1.66	0.18
6	5.9	14.6	8.3	-3.2	0.28	-4.8	0.44	0.29	-2	0.22
8	7.6	15.3	10.2	2	0.3	-4.3	0.4	0.3	-1.66	0.19

Table A.12: Steerer2 Vertical

Bibliography

[1] J.Beringer et al. (Particle Data Group), "Review of Particle Physics", Phys. Rev. D 86, 010001, (2012)

[2] P.W.Higgs, "Broken symmetries and the masses of gauge bosons", Phys. Rev. Lett. 13 (1964) 508509, doi:10.1103/PhysRevLett.13.508

[3] G.Arnison et al., "Experimental observation of isolated large transverse energy elelctrons with associated missing energy at $\sqrt{s} = 540\,GeV$", Phys. Lett. 122b (103), (1983)

[4] O.Brüning et al., "LHC Design Report", CERN-2004-003, (2004)

[5] ATLAS Collaboration, "ATLAS: Letter of Intent for General-Purpose pp Experiment at the Large Hadron Collider at CERN", CERN-LHCC-92-004, (1992)

[6] CMS COLLABORATION, "TECHNICAL PROPOSAL",CERN/LHCC 94-38, LHCC/P1, 15 December 1994, (1994)

[7] ALICE Collaboration, "ALICE : Technical proposal for a Large Ion collider Experiment at the CERN LHC", CERN-LHCC-95-71 ; LHCC-P-3, (1995)

[8] LHCB Collaboration, "LHCb: Technical Proposal, A Large Hadron Collider Beauty Experiment for Precision Measurements of CP Violation and Rare Decays", CERN-LHCC-98-004 ; LHCC-P-4, (1998)

[9] TOTEM Collaboration, "TOTEM, Total Cross Section, Elastic Scattering and Diffraction Dissociation at the LHC : Technical Proposal", CERN-LHCC-99-007 ; LHCC-P-5, (1999)

[10] K.Elsener et al., "The CERN neutrino beam to Gran Sasso (NGS) : conceptual technical design", CERN-98-02 ; INFN-AE-98-05, (1998)

[11] Isolde - Project, *http://isolde.web.cern.ch/ISOLDE/default2.php?index=index/facilityindex.htm&main=facility/portrait.php*

[12] L.W.Alvarez, "Minutes of the Meeting of September 19-21, 1946" in Procedings of the American Physical Society, Phys. Rev. 70 (1946) p.799

[13] R.Garoby, "Multiple bunch-splitting in the PS: results and plans", 11th Chamonix Workshop - January 15-19, Chamonix, France, (2001)

[14] M.Vretena et al., "Linac4 Technical Design Report", CERN-AB-2006-084 ; CARE-Note-2006-022-HIPPI, (2006)

[15] M.Martini, C.R. Prior, "High-intensity and high-density charge-exchange injection studies into the CERN PS Booster at intermediate energies", EPAC 2004, CERN-AB-2004-069, (2004)

[16] J.D.Jackson, "Klassische Elektrodynamik", Walter de Gruyter Berlin New York (2. Auflage), (1983)

[17] J.Rossbach and P.Schmüser, "Basic Course on Accelerator Optics", CERN Accelerator School 94-01, Cern, (1993)

[18] F.Hinterberger, "Physik der Teilchenbeschleuniger und Ionenoptik", Springer Verlag, (2008)

[19] B.J.Holzer - Private Communication

[20] K.R.Crandall and D.P.Rusthoi, "TRACE 3-D Documentation", Los Alamos National Laboratory, LA-UR-97-886, (1997)

[21] O.D. Kellogg, "Foundations of Potential Theory", Springer Verlag Berlin, (1976)

[22] A.Perrin and J.F.Amand, Travel v4.06, user manual, CERN (2003)

[23] H.Wiedemann, "Particle Accelerator Physics I", Springer Verlag, (1999)

[24] L.M.Hein, "Space Charge Effects in Cascaded HGHG-FELs", Diploma Thesis 2009,Humboldt-Universiät zu Berlin, Helmholtz-Zentrum Berlin, (2009)

[25] M.Scholz, Private Communication and "Simulationen zur H^- Charge Exchange Injection in den CERN Proton Synchrotron Booster mit Linac4", Diploma Thesis, 2010

[26] K.Schindl, "Space charge", CERN Accelerator School 2006-002, Cern, (2003)

[27] E.Wilson, "Transverse Beam Dynamics", CERN Accelerator School 94-01, Cern, (1993)

[28] O.Midttun, R.Scrivens, "A new extraction system for the Linac4 H^- ion source" - to be publ.

[29] M.Kronberger et al., "Commissioning of the new H^- source for Linac4", Review of Scientific Instruments 81, 02A708, (2010)

[30] J.B.Lallement, A.Lombardi, "A Pencil Beam for the Linac4 commissioning", sLHC-Project-Note-0017 ; CERN-sLHC-Project-Note-0017, (2010)

[31] C.Rossi - Private Communications

[32] P.Forck, "Beam Diagnostics and Instrumentation" (Lecture Notes), JUAS, Archamps, (2010)

[33] O.Midttun - Private Communication

[34] J.B.Lallement - Private Communication

[35] J.Billen, L.Young, "SUPERFISH/POISSON - Manual", LA-UR-96-1834

[36] D.A.Edwards & M.J.Syphers, "An Introduction to the Physics of High Energy Accelerators", A Wiley-Interscience Publication

[37] A.B.Ismail et al., "Space Charge Neutralization and its dynamic effects", 39th ICFA Advanced Beam Dynamics Workshop on High Intensity High Brightness Hadron Beams (ICFA-HB - 2006), Tsukuba, Japan, (2006)

[38] P.A.Posocco - Private Communication

[39] G.Bellodi, A.Lombardi, "Transfer Line Studies from LINAC4 to the PS Booster: Green Field Option", CERN AB-Note-2007-037 ABP, (2007)

[40] G.Bellodi, M.Eshraqi, J.B.Lallement, A.Lombardi - "Updated layout of the LINAC4 transfer line to the PS Booster (Green Field Option)", CERN AB-Note-2008-036 ABP, (2008)

[41] C.Carli - Private Communication

[42] R.Wegner, Minutes of Meeting: 'Meeting on Debuncher Cavity, 5. May 2010 ', *https://twiki.cern.ch/twiki/bin/view/SPL/DeBuncherCavity0510*, (2010)

[43] C.Carli, "Simulation of the CERN PS Booster Performance with 160 MeV H^- Injection from Linac4", PAC07, TUPAN093, (2007)

[44] R.Wegner, "Power needs for the debuncher cavity ", presentation at Meeting: "Meeting on Debuncher Cavity 24. March 2011 ", *https://twiki.cern.ch/twiki/bin/view/SPL/DeBuncherCavity0311*, CERN, (2011)

[45] L.M.Hein, A.Lombardi, "Update of the Linac4-PSB Transfer Line", CERN sLHC-Project-Note-0028, (2010)

[46] Y.Cai, "Lattice Performance of the PEP-II High Energy Ring", Slac-Pub-7733, (1998)

[47] M.G.Minty, F.Zimmermann, "Measurement and Control of Charged Particle Beams", Springer Verlag, (2003)

[48] J.B.Lallement, A.Lombardi, P.A.Posocco,"Emittance reconstruction technique for the Linac4 high energy commissioning" , CERN ATS-Note-2012-079 MD, (2012)

[49] M.G.Tudela - Private Communication

[50] N.Angert et. al., "CERN heavy-ion facility design report", CERN-93-01, (1993)

[51] M.Garcia Tudela et. al., "Update end-to-end simulations of Linac4", CERN, sLHC Project Note 0025, (2010)

[52] A.Lombardi et. al., "End-to-End Beam Dynamics for CERN LINAC4", CERN-AB-2007-001, (2006)

Acknowledgment

First of all I would like to emphasise my gratitude for the support and guidance of my supervisors Prof. Dr. Eberhard Jaeschke, Dr. Bernhard Holzer and Dr. Alessandra Lombardi.
Although Prof. Jaeschke went into retirement shortly before I decided to start a PhD. graduation, he immediately agreed to supervise and evaluate the work allowing me to apply for the PhD. position at CERN. His professional and private guidance has been the major support to complete this thesis.
My local supervisor Dr. Bernhard Holzer ensured a fast progress of my thesis and in particular in my professional education by means of frequent meetings, which are focused on current subjects of my work and on actual studies of CERN projects. Amongst the professional supervision Dr. Bernhard Holzer has been always a contact person and a strong support in private matters.
The work has been also directly supervised by Dr. Alessandra Lombardi, leader of the CERN Linac4 beam dynamics group. She immediately integrated me in her group and gave me the chance to deepen my knowledge about space charge influenced beam dynamics by entrusting me with the optimisation of the transfer line optics. In order to gain experiences in technical work Alessandra Lombardi offered me the opportunity to participate at the $3\,MeV$ Test Stand commissioning. Her professional and personal commitment is gratefully acknowledged.
Furthermore, I would like to thank Prof. Dr. Andreas Jankowiak, Prof. Dr. Thomas Lohse, Prof. Dr. Volker Ziemann and PD. Dr. Atoosa Meseck, who agreed to evaluate this thesis and to attend the public defence of it.

In the framework of my work on the transfer line optics I was strongly supported by Dr. Christian Carli, specialist on the CERN PS-Booster optics, and Rolf Wegner, expert on the Linac4 cavities. For the Test Stand commissioning a close collaboration with the Linac4 source team was established. In this cooperation I would like to highlight Dr. Richard Scrivens, Oystein Midttun and Michael O'Neil, who acquaint me with the Linac4 prototype source and assisted in its operation.
Moreover, I would like to mention Dr. Piero Antonio Posocco, Dr. Detlef Kuchler and Giulia Bellodi. During my work I collaborated with many more colleagues, who all support my work by their expertise and fruitful discussions. Amongst the support of my colleagues of CERN I was also strongly supported by my friends from the Helmholtz-Zentrum Berlin (HZB).
Finally, I would like to thanks my friends and my family for their encouragement. A very special thanks goes to my parents, whose commitment and continuous support encouraged and allowed me to make my interest in science to my profession.
For all your support and the good time I had at CERN and in Berlin I want to thank you.

List of Publications

[1] L.M. Hein, "Space Charge Effects in Cascaded HGHG-FELs", Diploma Thesis 2009, Humboldt-Universiät zu Berlin, Helmholtz-Zentrum Berlin, (2009)

[2] M. Garcia Tudela et. al., "Update end-to-end simulations of Linac4", CERN, sLHC Project Note 0025, (2010)

[3] L.M. Hein, A.Lombardi, "Update of the Linac4-PSB Transfer Line", CERN sLHC-Project-Note-0028, (2010)

[4] G. Bellodi et. al., "Beams dynamics optimisation of LINAC4 structures for increased operational flexibility", Linac2010, CERN-ATS-2010-202, (2010)

[5] G. Bellodi et. al., "Alignment and Field Error Tolerance in Linac4", Internal Note, CERN-ATS-Note-2011-021 PERF, (2011)

[6] L.M. Hein et. al., "LINAC4 low energy beam measurements", IPAC2012, CERN-ATS-2012-206, (2012)

[7] G. Bellodi et. al., "Pre-commissioning results of the Linac4 Front-End", Linac2012, to be published, (2012)

Selbständigkeitserklärung

Ich erkläre, dass ich die vorliegende Arbeit selbständig und nur unter Verwendung der angegebenen Literatur und Hilfsmittel angefertigt habe.

Berlin, den 19.03.2013 Lutz Matthias Hein